Theoretical Analysis of Torsionally Vibrating Microcantilevers for Chemical Sensor Applications in Viscous Liquids

Tao Cai
Marquette University

Recommended Citation

Cai, Tao, "Theoretical Analysis of Torsionally Vibrating Microcantilevers for Chemical Sensor Applications in Viscous Liquids" (2013). *Dissertations (2009 -)*. Paper 301.
http://epublications.marquette.edu/dissertations_mu/301

THEORETICAL ANALYSIS OF TORSIONALLY VIBRATING MICROCANTILEVERS FOR CHEMICAL SENSOR APPLICATIONS IN VISCOUS LIQUIDS

By

Tao Cai, B.E., M.E.

A Dissertation submitted to the Faculty of the Graduate School,
Marquette University,
in Partial Fulfillment of the Requirements for
the Degree of Doctor of Philosophy

Milwaukee, Wisconsin

December 2013

ABSTRACT
THEORETICAL ANALYSIS OF TORSIONALLY VIBRATING MICROCANTILEVERS FOR CHEMICAL SENSOR APPLICATIONS IN VISCOUS LIQUIDS

Tao Cai, B.E., M.E.

Marquette University, 2013

Dynamically driven microcantilevers excited in the transverse (or out-of-plane) direction are widely used as highly sensitive chemical sensing platforms in various applications. While these devices work very well in air, their performance in liquids is not efficient because of the combination of increased viscous damping and effective fluid mass. In order to improve the characteristics of microcantilevers in liquid environments, some other vibration modes such as the torsional mode and lateral (or in-plane) flexural mode have been proposed.

In this work, the characteristics of torsionally vibrating rectangular microcantilevers with length L, width b and thickness h in viscous liquids are investigated taking into account the thickness effects. Finite element models are used to obtain the hydrodynamic loading (torque per unit length) and thus calculate values of the hydrodynamic function. An analytical expression of the hydrodynamic function in terms of the Reynolds number and aspect ratio, h/b, is then obtained by fitting the numerical results. This allows for the characteristics to be investigated as a function of both beam geometry and fluid properties, considering thickness effects on the torsional constant, the hydrodynamic function and the polar moment of area. For high aspect ratios, ($h/b>0.16$) microcantilevers vibrating in the 1st torsional mode, ignoring thickness effects could result in a minimum error of 9%, 5%, 20%, 7% for the resonance frequency, quality factor, mass sensitivity, and normalized mass limit of detection, respectively. Clearly, for many sensing applications based on analyzing the resonance frequency and mass sensitivity, thickness effects should be taken into account. The resonance frequency is found to be dependent on $h/(bL)$ and the quality factor is found to be dependent on $h/L^{1/2}$ for microcantilevers vibrating in the 1st torsional mode in viscous liquids. In comparison, for microcantilevers vibrating in the 1st lateral mode, the resonance frequency is dependent on b/L^2 and the quality factor is dependent on $hb^{1/2}/L$. Such different trends can be used to optimize device geometry and liquid property, thus maximizing quality factor and sensitivity in chemical sensing applications. Compared with microcantilevers in the 1st transverse mode, microcantilevers that vibrate in their first torsional mode have higher resonance frequency and quality factor. The increase in resonance frequency and quality factor results in higher sensitivity and reduced frequency noise, respectively. This will yield much lower limits of detection in liquid-phase chemical sensing applications.

ACKNOWLEDGMENTS

Tao Cai, B.E., M.E.

I would like to thank my academic advisor, Dr. Fabien Josse, for his advice, understanding, and patience over the whole course of my Ph.D. study and research. He has been motivating, encouraging, and enlightening. His guidance is essential in the preparation of this work. Thank you, Dr. Josse.

I would like to thank Dr. Stephen Heinrich and Dr. Nicholas Nigro for the many hours of discussions on the physical and numerical modeling of the system. My gratitude is also extended to Dr. Oliver Brand at Georgia Institute of Technology for providing experimental data used to confirm results in this dissertation and helping me a lot during IFCS conference. I would like to thank Dr. Edwin Yaz, Dr. Isabelle Dufour, Dr. Susan Schneider, and Dr. Chung Hoon Lee for their useful input on my research and helps to improve my presentation skills.

I would like to thank my entire research committee (Dr. Josse, Dr. Heinrich, Dr. Lee, Dr. Schneider, and Dr. Yaz) for their corrections and suggestions on how to improve this dissertation. Thanks are also given to the current and former members of the Microsensor Research Group, especially Dr. Florian Bender, Dr. Russell Cox, and Dr. Jinjin Zhang.

Finally I would like to thank my wife (Dr. Xiaojun Liu), my daughter (Cari Qinyun Cai), my parents (Chongwan Cai and Qun Song), my sister (Lei Cai), my brother-in-law (Yun Shen), my family and friends for their supports and concerns throughout the whole journey of my graduate study abroad.

TABLE OF CONTENTS

LIST OF TABLES

LIST OF FIGURES

1. INTRODUCTION

1.1 MEMS-based Sensors

Microelectromechanical systems (MEMS) are miniaturized devices using mechanical and electro-mechanical elements by the microfabrication technology [1]. MEMS are also referred to as micromachines in Japan, or micro systems technology (MST) in Europe. The critical physical dimensions of MEMS devices can vary from below one micron to several millimeters. In any MEMS devices, there are at least some elements having some sort of mechanical functionality whether these elements can move or not. While the functional elements of MEMS are miniaturized structures, sensors, actuators, and microelectronics, one of the most notable elements is the microsensor. MEMS-based sensors are micro devices that convert the measured mechanical signals into electrical signals [1]. When the mechanical structure in a MEMS-based sensor is designed to vibrate at a resonance frequency, these sensors are called MEMS resonant sensors. One such mechanical structure in a MEMS-based sensor is the microcantilever. In this dissertation, microcantilever-based MEMS resonant sensors will be investigated.

MEMS-based sensors have applications in industry, environment and other various areas. Based on the different sensing mechanisms [1], MEMS-based sensors can function as flow sensors [2-6], magnetic sensors, thermal sensors, thermal actuators, humidity sensors [7-8], and energy harvesters [9-18]. For example, MEMS-based micro hot-plate devices [19-21] are widely used as thermal sensors. This type of device consists of micro hot-plates as integrated heater elements. The advantages of the micro hot-plate approach are the low power consumption, fast transient operation, direct integration with additional electronic components, miniaturization, and reduction of fabrication costs.

Generally speaking, MEMS-based sensors have various applications in electronics, photonics, mechanics, chemistry and biology, etc. In this dissertation, chemical sensor applications will be investigated. Chemical sensors are characterized in many different ways by their sensitivity, resolution and selectivity [1]. The sensitivity is the ratio of the magnitude of the output signal to the magnitude of the input quantity to be measured. The resolution is a measure of the minimum change of the input quantity to which the chemical sensor can respond, which is also called the limit of detection (LOD). The selectivity is the degree to which the chemical sensor can distinguish one input quantity from another. Basically, a chemical sensor with high sensitivity, low limit of detection, and high selectivity is desired.

For microcantilever-based MEMS resonant sensors, the two important characteristics are the resonance frequency and quality factor. The resonance frequency is the frequency of a vibrating system at which the response amplitude is a relative maximum. When operating at a resonant frequency, even a small periodic driving force can produce a large-amplitude vibration because the system can store and easily transfer energy between kinetic energy and potential energy. When the system reaches its steady state, the energy loss of the system is equal to the excitation energy from the driving forces in each cycle. Without driving forces, the amplitude of the system will reduce exponentially due to the energy loss. The quality factor is dependent on the damping mechanisms that are the sources of energy loss. It is a dimensionless parameter that describes how damped an oscillator or resonator is. Equivalently, the quality factor characterizes a resonator’s bandwidth relative to its resonance frequency. Higher quality factor indicates a lower energy loss per cycle compared to the maximum stored energy of the system.

In a liquid environment, liquid damping is one of the main physical damping mechanisms inherent to microcantilever-based MEMS resonant sensors [22]. The liquid damping relates to the energy loss due to the interaction between the microcantilever and the surrounding liquid at its vibrational state. The liquid damping has three contributions: viscous damping [23], acoustic radiation [24] and squeezed-film damping [25]. The viscous damping is due to the interaction i.e. friction between the liquid and the structure as well as the direction of the friction being parallel to the device motion. The acoustic damping is due to the acoustic radiation when the resonator excites a wave in the liquid in the direction perpendicular to the device motion. The squeezed-film damping is due to liquid motion perpendicular to the surfaces when the liquid is pushed into or out of the gap formed by adjacent surfaces. For example, the squeezed-film damping is significant for MEMS devices with a plate that moves against a trapped film. In this dissertation, only the liquid damping due to the viscous drag will be considered and all the other damping mechanisms will be ignored.

The support damping, surface-effect damping, thermoelastic damping, and viscoelastic damping are four other main physical damping mechanisms inherent to microcantilever-based MEMS resonant sensors in a liquid [22]. The support damping, which is also called anchor losses, is the energy loss from the resonator to the substrate when the resonator anchors are stressed at the clamping points as a consequence of resonator displacement during vibration. Surface-effect damping is the energy loss due to the roughness, contaminants, and etching residues on the surfaces. Thermoelastic damping is an intrinsic-material damping source due to the thermoelasticity present in almost all materials. It is caused by irreversible heat flow across the thickness of the resonator, which describes the energy coupling between the elastic field and the temperature field. The viscoelastic damping is another intrinsic-material damping source, which is due to the viscoelasticity present in viscoelastic materials such as polymers. The Young's modulus of a viscoelastic material is represented by a complex number. The real part of this complex number is known as the storage modulus, which is associated with the elastic behavior of the material; the imaginary part is called the loss modulus, which is associated with the viscous behavior of the material and determine the energy dissipative ability of the material.

Most MEMS-based sensors are fabricated from silicon wafers or silicon-on-insulator (SOI) wafers by micromachining techniques [27]. The details of each step of the micromachining techniques are well-described in the literature [28-31]. The micromachining techniques make it possible to integrate the MEMS device with additional electronic components. For example, a mechanical sensing component can be integrated with the complementary metal-oxide-semiconductor (CMOS) [2] circuit on a silicon chip.

The sensing elements of MEMS-based sensors are microstructures such as beams, bridges, membranes, and plates, which are fully or partially anchored, usually onto a silicon substrate. The three classical schemes of the mechanical structure in a MEMS resonant sensor are the cantilever, the fixed-fixed beam, and the folded beam.

The cantilever beam has the simplest structure, where one end of the beam extents from the substrate and the other end of the beam is free. A typical cantilever resonator is shown in Figure 1-1 [31]. Since one end of the cantilever is free, there are negligible residual stresses introduced from the fabrication. Compared to the fixed-fixed or folded beam, the cantilever beam is easier to fabricate, excite and analyze due to its simple structure [34]. Cantilever resonant sensors are mostly used to measure mass [31,35].

The fixed-fixed beam resonator has a vibrating mass fixed at two points. There are many variations of this basic structure. One of the popular implementations of this scheme is the double-ended tuning fork (DETF) [36-38], which consists of two parallel beams with identical length. A DETF type fixed-fixed resonator is shown in Figure 1-2 [28]. Oscillation is usually performed laterally and in an anti-symmetric mode. One significant drawback of this design is the susceptibility of DETFs to post-fabrication stresses in the two beams which are clamped on both ends. DETFs have been used in many applications, including force sensors [36], gyroscopes [37], accelerometers [39], and strain sensors [40].

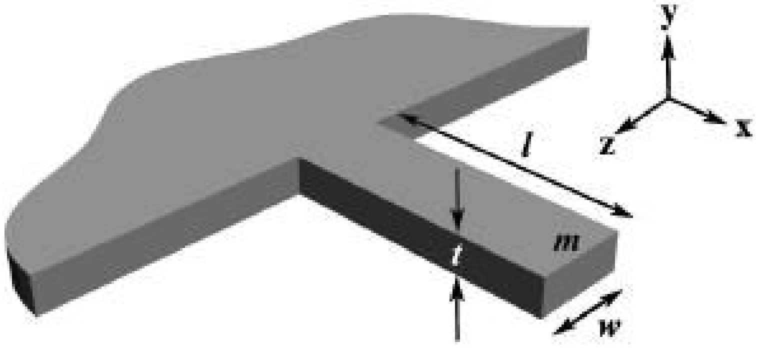

Figure 1-1: Typical cantilever resonator, adapted from Ref. 31.

The folded beam resonator is the most complex, but most flexible design. In this design, the beams are extended out from a substrate anchor and then "folded" back onto themselves to extend in the opposite direction. A folded beam resonator is shown in Figure 1-3 [40]. Similarly to the cantilever resonator, there are negligible residual stresses

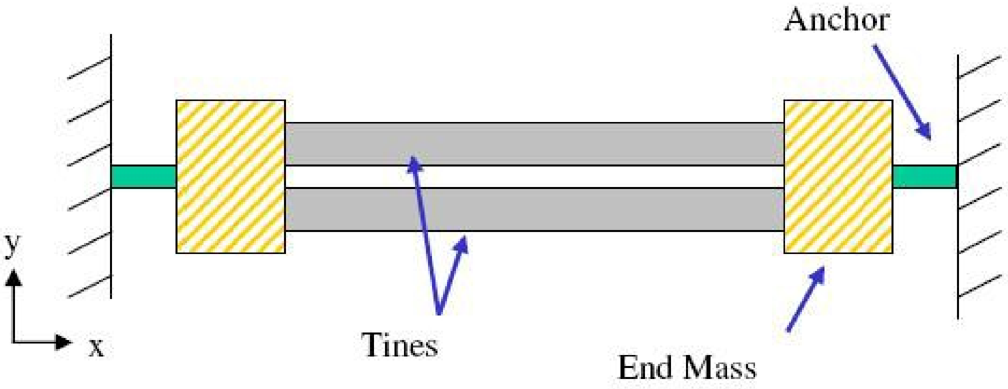

Figure 1-2: Double-ended tuning fork (DETF) type fixed-fixed resonator, adapted from Ref. 28.

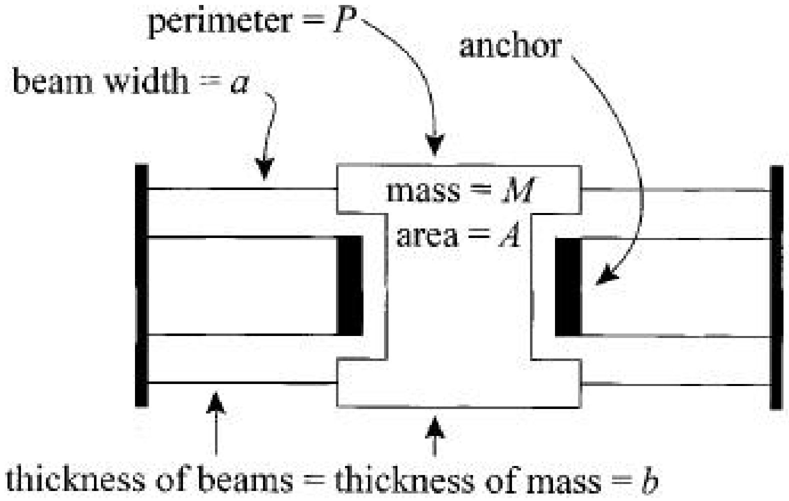

Figure 1-3: Folded beam resonator, adapted from Ref. 40.

due to the fabrication in a folded beam resonator because the expansion of the beams is no longer bounded by the anchors. A rough analytical expression for the fundamental frequency of the folded beam resonator was proposed in Ref. 40. The folded beam resonators are used in many of the same applications as the fixed-fixed beam resonators, but they are more robust against spurious influences from post-fabrication dimensional variations [40] and temperature variations [41].

Of all the three classical schemes, the cantilever is the most widely used as a MEMS resonant sensor. For chemical sensing applications, the microcantilever, as the sensing element, is often coated with a chemically sensitive layer in order to interact with the target analyte [50]. The chemical sensing layer is the most important part of the chemical sensor since it contributes greatly to the overall sensitivity and determines the sensor's selectivity to a certain analyte or class of analytes. The material of the coating could be a metal, a polymer, or a bio-functionalized coating. There are two different interactions between the analyte and the sensing layer: surface interaction and bulk interaction [50]. In the surface interaction, the analyte is adsorbed onto the surface of the sensing layer, whereas it is absorbed into the sensing layer in the bulk interaction. For a specific sensor, it could be either surface interaction when sensing some large size particle, or bulk interaction when sensing some small size particles.

In order to achieve resonance in the mechanical structure of a MEMS resonant sensor, the device must be excited by an actuator and set to resonate by varying the excitation frequency. The most popular and widely used excitation methods are capacitive actuation and piezoelectric actuation [26].

The capacitive actuation is based on the principle of electrostatics. There are two main schemes: the parallel plate and the comb drive design. The parallel plate actuator is perhaps the only actuation method that can be used to drive any of the three resonator types [26]. The major drawback of this scheme is that the response is nonlinear [28]. The parallel plate scheme was demonstrated and used in a resonant mass sensor application [32,43]. The comb drive actuators consist of two interdigitated finger structures with one fixed and the other connected to a compliant suspension. It is widely used since the response of the comb is linear. A comprehensive analytical treatment of the comb structure was performed by taking into account many electrical field nonlinearities and discontinuities [46]. Since one of the combs must be physically coupled to the resonator, this excitation scheme is employed only for fixed-fixed and folded beam structures [33,36,43,47].

The piezoelectric actuation is based on the piezoelectric effect. The main drawback of piezoelectric actuation is the necessity of the additional piezoelectric material and the integration of the piezoelectric material with the SOI resonator [32,35,48].

Both the capacitive and the piezoelectric methods used in actuators can be also used in transducers. Besides the capacitive and piezoelectric methods, magnetic actuation [44-45], electrothermal actuation [77], photothermal actuation [42], piezoresistive detection [77], and optical detection [42-43] are also used in MEMS resonant sensor applications. For example, the electrothermal excitation and piezoresistive detection were chosen as driving and detector mechanisms in Ref. 77 because they can be easily integrated with the use of diffused resistors. In this implementation, two diffused p-type silicon resistors, as electrothermal excitation elements, were integrated at the clamped edge of the microcantilever. One of the heating resistors was driven by an AC voltage superimposed on a DC voltage in order to excite the microcantilever and avoided frequency doubling. A full Wheatstone bridge configuration was chosen for the sensing piezoresistors on the microcantilever in order to reject common-mode signals such as deflection due to the common temperature change.

The mechanical structure in a MEMS-based sensor can operate in different modes. Among the different chemical sensor platforms, microcantilever-based sensors are of high interest since they are easily fabricated and in many cases have high sensitivity and quality factor. Microcantilevers can operate in the static mode [50] or dynamic mode. When working in a dynamic mode, the microcantilever can operate in transverse (out-of-plane flexural) mode [51-74], lateral (in-plane flexural) mode [71-86], torsional mode [51-60,85-94], longitudinal mode [95-96], or coupled modes [97].

The cross-section of a microcantilever could be uniform or non-uniform. In this dissertation, the term "rectangular microcantilever" stands for a microcantilever with a uniform rectangular cross-section. The term "circular microcantilever" stands for a microcantilever with a uniform circular cross-section. A rectangular microcantilever with length *L*, width *b*, and thickness *h* under transverse, lateral, torsional, or longitudinal mode is depicted in Figure 1-4. Microcantilevers with some other shapes such as T-shape beams [54,83,90-91,98-100], U-shaped beams [54], and V-shaped beams [53-54] have also been investigated and described in the literature. In addition to vibrating microcantilevers, trampoline-shape micro-structures [101-104] and rotational mode micro-disks [105-107] were also actively investigated and presented in the literature.

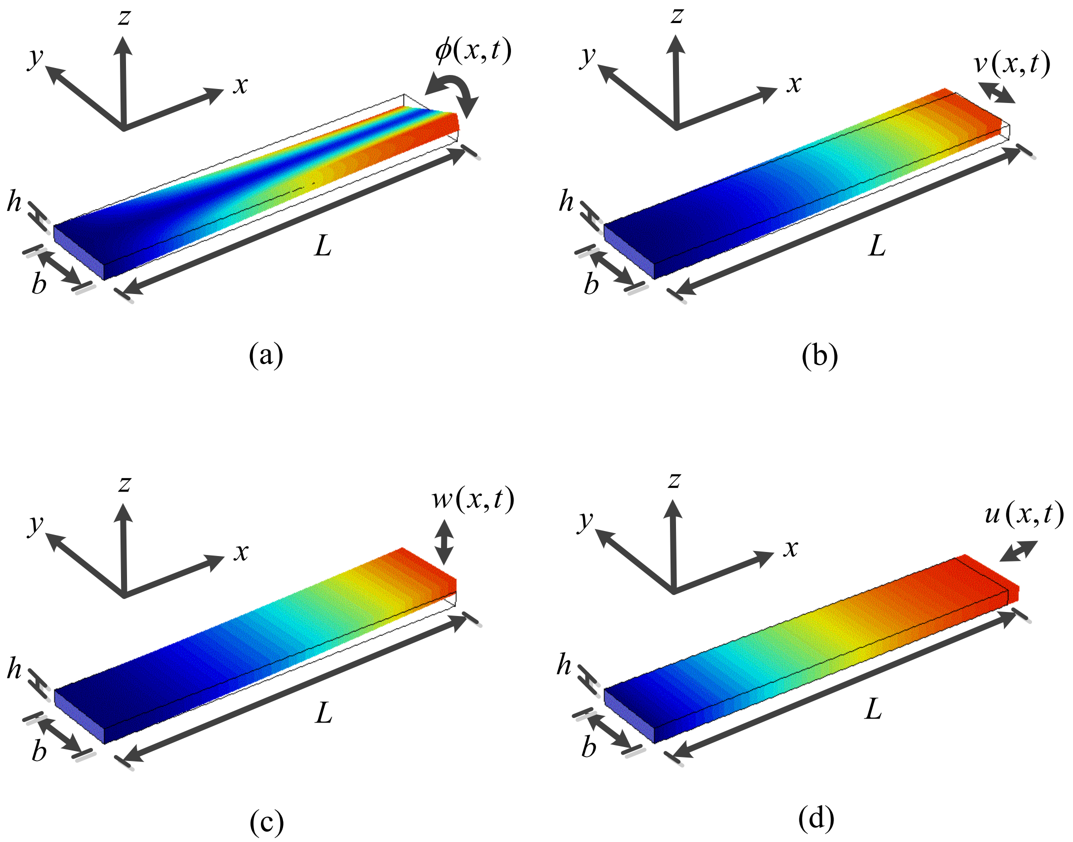

(a) (b) (c) (d)

Figure 1-4: Geometry of a rectangular microcantilever with length *L*, width *b*, and thickness *h*, vibrating (a) torsionally, (b) laterally, (c) transversely, (d) longitudinally, where ϕ, *v*, *w*, *u* are the rotational deflection (angle) in y-z plane, deflection in y direction, deflection in z direction, and deflection in x direction, respectively. The color coding represents the deflection in the relevant direction.

1.2 Modeling Vibrating Microcantilevers

Microcantilevers torsionally, laterally, or transversely vibrating in vacuum have been investigated and presented in the literature [110,116]. The resonance frequencies associated with the different order of torsional, lateral, or transverse mode were obtained in closed-form analytical expressions in terms of the geometry and material properties of the microcantilever by solving the relevant equation of motion of the vibrating beam.

Although the resonance frequencies of cantilevers vibrating torsionally, laterally, or transversely in air are very close to those in vacuum, they decrease considerably when operating in liquids. For the cantilevers with low aspect ratio (*h*/*b*) vibrating torsionally, laterally, or transversely in an inviscid liquid, Chu [51-52] obtained closed-form analytical expressions for the resonance frequencies, in terms of the geometry and material properties of the microcantilever and the density of the liquid, by considering the liquid's pressure effect and solving the Navier-Stokes equations of inviscid liquids [114]. The hydrodynamic loads due to the liquid's pressure effect (effective added mass) were obtained using the chordwise hydrodynamic strip theory [51-52].

However, Chu's analysis [51-52] is not applicable for a microcantilever in a viscous liquid where the viscosity of the liquid increasingly affects the motion of the liquid around the vibrating microcantilever. For a microcantilever vibrating in viscous liquids, both the pressure effect and viscous shear effect of the liquid must be taken into account. By calculating the hydrodynamic load (resisting force for transverse mode and resisting torque for torsional mode) per unit length, closed-form analytical expressions of the hydrodynamic functions of a transversely or torsionally vibrating circular microcantilever in viscous liquids were obtained by Stokes [115,87]. The hydrodynamic functions are in terms of the Reynolds number, which is a dimensionless parameter that gives a measure of the ratio of inertial forces to viscous forces. But these analytical expressions are only for circular cross-section microcantilevers and cannot be used for rectangular cross-section microcantilevers, which are widely used in MEMS resonant sensor applications. For a rectangular microcantilever vibrating laterally in a viscous liquid, Stokes [75] also obtained a closed-form analytical expression of the hydrodynamic function in terms of the Reynolds number by assuming the microcantilever as an infinite flat plate and by calculating the resisting force per unit length from the liquid.

For a rectangular microcantilever torsionally or transversely vibrating in viscous liquids, Sader [88,62] proposed an analytical expression of the hydrodynamic function and set up the procedure to calculate the resonance frequency and quality factor, assuming the microcantilever has negligible thickness (ribbon case). In these approaches, the microcantilever was assumed as an infinite flat plate with negligible thickness; as a result, the edge effect and thickness effect were not taken into account. The hydrodynamic function in term of the Reynolds number was obtained by solving the linearized Navier-Stokes equations for viscous liquids [114], using the numerical integral method introduced by Tuck [61]. Although the analytical expressions of the hydrodynamic function are accurate for the ribbon case, the expressions are very complex. Some simplified expressions were proposed by fitting the numerically obtained values of the hydrodynamic function in a range of Reynolds numbers [67,70].

Recently, Aureli [70,93] improved the analytical expression of the hydrodynamic function of a microcantilever vibrating torsionally or transversely in a viscous liquid by considering the nonlinear liquid effects due to moderately large amplitude rotations. In those approaches, the hydrodynamic functions were obtained by solving the nonlinear Navier-Stokes equations for viscous liquids [114] using a set of two-dimensional computational fluid dynamics (CFD) simulations of a rigid thin plate, representative of a cross section of the vibrating microcantilever. A correction term associated with the effect of the finite vibration amplitude was added to the hydrodynamic function proposed by Sader for the transverse mode [62] and torsional mode [88].

Among the many modes mentioned above, microcantilevers vibrating in the transverse (out-of-plane) mode [51-74] are widely investigated and used as highly sensitive chemical sensor platforms in various applications. The shift in the resonance frequency of the microcantilevers is used to measure the presence and concentration of a chemical analyte in the operating environment. Especially in air, mass changes in the range of picograms [64], femtograms [66], even attograms [68] have been detected and the results have been presented in the literature.

While transversely vibrating microcantilevers operate well in air, they have limited applications in viscous liquid media. The resonance frequency and quality factor of the device decrease greatly because of the additional fluid resistance (combination of increased viscous damping and effective fluid mass due to the liquid medium). Therefore, the mass sensitivity of the system decreases dramatically and the system's susceptibility to frequency noise increases. In order to improve these characteristics, it has been proposed to reduce the length of the microcantilever, to operate in higher-order transverse flexural modes [57,72,85], or to investigate other vibration modes of microcantilevers, such as the torsional mode [51-60,85-94] or lateral (in-plane) flexural mode [71-86].

Reducing the length of the transversely vibrating microcantilever can increase the resonance frequency of the microcantilever since the resonance frequency of the microcantilever is roughly inversely proportional to its length squared. Also reducing the length of the microcantilever can increase the quality factor of the system since the fluid damping decreases due to the smaller surface area of the interface between the microcantilever and the surrounding medium. However, the shorter microcantilever with smaller sensing area leads to smaller amounts of analytes that can be sorbed into the sensing layer, which result in a smaller shift of the resonance frequency due to the sorbed analyte. As the length of the microcantilever decreases, the support loss increases and may not be negligible compared to the viscous liquid loss.

Operating in higher-order transverse flexural modes [57,72,85] can increase the resonance frequency and quality factor. However, the support loss and the difficulty to excite the microcantilever also increase. Furthermore, experimental work by Maali [67] indicates that the theoretical errors of the resonance frequency and quality factor increase as the mode number increases if the hydrodynamic function is calculated using the semi-analytical model by Sader [62]. In order to resolve this issue, exact analytical solutions for the 3D flow field and hydrodynamic function were derived by Van Eysden and Sader for the microcantilever in incompressible viscous fluids [55-57] and compressible viscous fluids [58-59]. In these models, the hydrodynamic functions were obtained by solving a linear system of algebraic equations. Coefficients of the linear system were complex and expressed in terms of the Meijer G function [112].

For a rectangular microcantilever operating in the first lateral mode in viscous liquids, simple closed-form expressions were proposed in Ref. 78 to calculate the beam response, the resonance frequency and the quality factor by using a single degree of freedom (SDOF) model and a harmonic tip force. The SDOF model was based on beam theory and the assumption that the fluid resistance resulted from the shear stresses, which were given by the classical solution by Stokes for an oscillating infinite plate. A new analytical model was also derived in Ref. 79 for an electrothermally driven microcantilever experiencing lateral vibration in a liquid and successfully confirmed the validity of the previously proposed closed-form expressions based on the SDOF model [78].

For a rectangular rigid plate laterally vibrating in viscous liquids, Brumley and Sader [73-74] obtained a table of values of the hydrodynamic function at some specific Reynolds number and aspect ratio (*h*/*b,* with thickness, *h*, and width, *b*). In this approach, the edge effects and thickness effects of liquids were considered and the boundary integral technique of Tuck [61] was extended. However, an analytical expression for the hydrodynamic function was not provided.

Recently, the hydrodynamic function was obtained in Ref. 84 for a rigid bar with a rectangular cross-section laterally vibrating in a viscous liquid by ANSYS numerical simulations. The hydrodynamic function was then used to calculate the characteristics, such as resonance frequency and quality factor, of laterally vibrating microcantilevers in viscous liquids. In this approach, the edge effects and thickness effects of liquids were considered and an analytical expression of the hydrodynamic function in terms of Reynolds number and aspect ratio (*h*/*b*) was provided by fitting the numerical results. Based on the analytical expression of the hydrodynamic function, the characteristics such as resonance frequency, quality factor, and mass sensitivity of the laterally vibrating microcantilevers were investigated and compared to those of the transversely vibrating microcantilevers. The comparison indicates that operating dynamically driven microcantilevers in the lateral mode is better than transverse mode for liquid-phase (bio)chemical sensing applications.

For a rectangular microcantilever torsionally vibrating in viscous liquids, the approaches to calculate the hydrodynamic function and the characteristics such as resonance frequency and quality factor from both Sader [88] and Aureli [93] assume that the thickness of the microcantilever is negligible compared to its width and length. However, the results based on these approaches show that for torsional mode, both the resonance frequency and the quality factor increase as the thickness of the microcantilever increases. Thus, in order to improve the performance of a torsion-based cantilever liquid-phase chemical sensing platform, the thickness of the torsionally vibrating microcantilever should be considered. This necessitates the inclusion of the thickness effects when evaluating the hydrodynamic function, in addition to the polar moment of area and the torsional constant. Such improvements will be considered in this dissertation.

1.3 Problem Statement and Objectives

Microcantilevers operating in the out-of-plane flexural mode (also known as transverse mode) have applications in both gas and liquid phases. However, in liquid phase, this mode of operation does not yield efficient microcantilevers because the resonance frequency, sensitivity and frequency stability of the vibrating microcantilevers drastically decrease. This is due to the larger fluidic resistance forces in the liquid: the inertial force and damping force. In order to improve the characteristics of transversely vibrating microcantilevers, several methods have been investigated, which include reducing the length of the microcantilever, operating in higher-order modes, or changing the shape of the microcantilever from uniform rectangular cross-section to other shapes such as a hammerhead. Another promising method to implement highly efficient liquid-phase sensors is to operate the microcantilever in the torsional mode [51-60,85-94] or in-plane flexural mode (or lateral mode) [71-86], in order to achieve higher resonance frequency and quality factor, hence higher sensitivity.

For the laterally vibrating microcantilevers in viscous liquids, several attempts of modeling the hydrodynamic function have been made. Some investigations assume the thickness of the microcantilever to be negligible, thus treating the microcantilever as a ribbon [75]. Other investigations consider both the edge effects and the thickness effects of a rectangular microcantilever in viscous liquids [73-74, 84] and provide an analytical or semi-analytical expression of the hydrodynamic function in terms of Reynolds number and aspect ratio (h/b) [84]. On the other hand, for the hydrodynamic function of torsionally vibrating microcantilevers in viscous liquids, all the investigations [88, 93] presented in the literature ignore the edge effects and thickness effects and regard the microcantilever as a ribbon.

The research objective of this dissertation is to theoretically investigate torsionally vibrating resonant rectangular microcantilevers for chemical sensor applications in liquid environments to determine whether improved characteristics can be achieved by optimizing the microcantilever geometry.

In order to achieve this research objective, the governing equation for rectangular microcantilevers excited sinusoidally in time by a torque per unit length distributed arbitrarily along the axial direction in a viscous liquid will be derived and analyzed by considering the liquid effect as an external torque per unit length which, when normalized, will yield the hydrodynamic function. The hydrodynamic function of rectangular microcantilevers under torsional mode in liquids will be determined in terms of both Reynolds number and aspect ratio (h/b) by using numerical simulations, in which the microcantilever is assumed to be a rigidly rotating body excited sinusoidally in time. An analytical expression for the hydrodynamic function will then be obtained by fitting the numerical results. Based on the hydrodynamic function, analytical expressions for the device characteristics such as the resonant frequency, quality factor, mass sensitivity, and normalized mass limit of detection (LOD) will be derived and applied to evaluate various cantilever geometries and liquid properties. The trends of the characteristics of microcantilevers under torsional mode will be shown as functions of changes in the structure dimensions and liquid properties. The resonance frequencies and quality factors of torsionally vibrating microcantilevers in water will be calculated and the results will be compared to those under transverse and lateral vibration modes, and the limited experimental data that is available [125]. Finally, design procedures and design guidelines will be provided and discussed.

1.4 Dissertation Organization

This dissertation is organized into six chapters. In Chapter 1, an introduction to the chemical sensors is given. Emphasis is placed on the dynamic mode microcantilever-based chemical sensors. The methods in the literature used to model the microcantilevers under transverse, lateral, or torsional mode are investigated. The main objectives of this dissertation are introduced, that is, to characterize the microcantilever-based chemical sensors operating under torsional mode in viscous liquids.

In chapter 2, the equation of motion will be established and solved for the rotational deflection of a microcantilever vibrating torsionally in a viscous liquid. By using the undamped mode shapes and the method of mode superposition [110], the result will be expressed in terms of an arbitrary excitation frequency. This can be used to find the response characteristics, such as the frequency spectrum, resonance frequency, and quality factor, and the sensing metrics of sensitivity and limit of detection if the device is used as a sensor. All of these quantities depend on the hydrodynamic function, i.e., the normalized hydrodynamic torque per unit length, which must be known.

In chapter 3, the hydrodynamic functions will be obtained by solving Navier-Stokes equations for incompressible Newtonian liquids. After a review of Stokes' solution to the hydrodynamic function for circular microcantilevers, the numerical evaluation of the hydrodynamic function for rectangular microcantilevers for 19 Reynolds numbers and 11 aspect ratios (thickness to width) will be obtained using numerical simulations in COMSOL. Three methods are used to extract the magnitude, phase, real part and imaginary part of the hydrodynamic function. Thus, by fitting the numerical results, an analytical expression for the hydrodynamic function, including the thickness effects, is obtained for the first time for rectangular microcantilevers vibrating torsionally in viscous liquids.

In chapter 4, the frequency spectra, resonance frequencies and quality factors of rectangular microcantilevers operating in the first torsional mode in viscous liquids are obtained. The dependencies of the resonance frequency and quality factor on the geometry of the microcantilever operating in the first torsional mode and the material properties of the liquid are investigated. The resonance frequencies and quality factors of rectangular microcantilevers operating in the first torsional mode in water are calculated and compared to those for first transverse and first lateral mode, and the limited experimental results that are available [125].

In chapter 5, the mass sensitivity and normalized mass limit of detection of torsionally vibrating rectangular microcantilevers in viscous liquids are defined and obtained. The mass sensitivity and normalized mass limit of detection of rectangular microcantilevers operating in the first torsional mode in viscous liquids are obtained. The dependencies of the mass sensitivity and normalized mass limit of detection on the geometry of the rectangular microcantilever operating in the first torsional mode and the material properties of the liquid are investigated. In addition, the design procedure for the rectangular microcantilever dimension is provided for a given working resonance frequency.

Finally in chapter 6, a summary of the results, conclusions and suggestion on future research topics are given.

2. TORSIONALLY VIBRATING MICROCANTILEVERS IN VISCOUS LIQUIDS

2.1 Problem Statement and Assumptions

A typical rectangular microcantilever under torsional mode of operation is shown in Figure 2-1, where L, b, h are the length, width, thickness of the microcantilever, respectively. In analyzing the vibrating cantilever, the following assumptions are used:

(1) The microcantilever is assumed to be an elastic Euler-Bernoulli beam.

(2) For the purpose of calculating the hydrodynamic load, the microcantilever is assumed to be a rigidly rotating body.

(3) The length (L) of the microcantilever is much greater than its width (b) or thickness (h) so that the support effect and edge effect can be ignored.

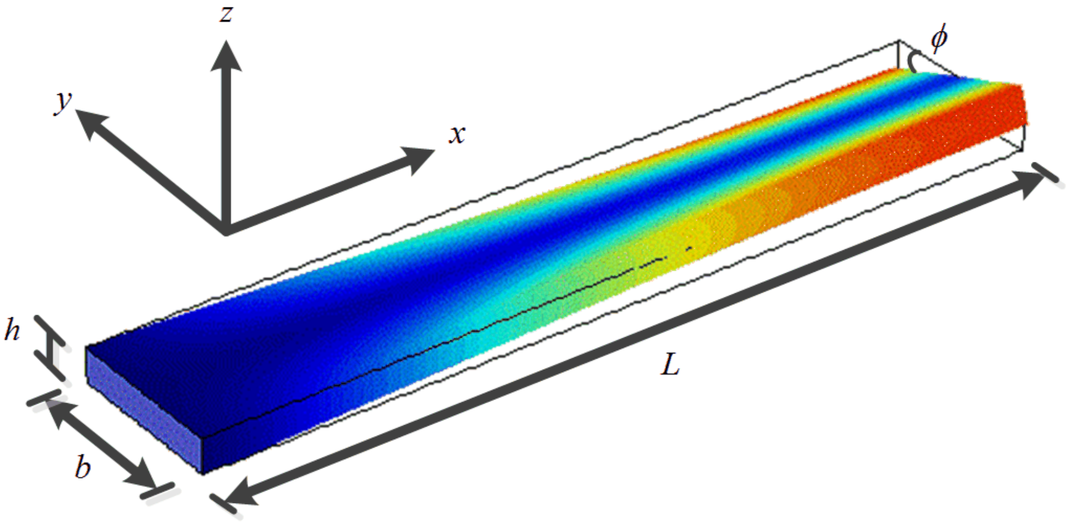

Figure 2-1: Geometry of a torsionally vibrating rectangular microcantilever with length L, width b, and thickness h, where ϕ is the rotational deflection (angle). The color coding represents the z-axis deflection.

(4) The amplitude of the rotational deflections (rotation angles of the cross sections) is assumed to be very small such that the nonlinear convection term in Navier-Stokes equations can be ignored.

(5) Mode coupling between different orders and types of vibrating modes is not considered.

(6) The longitudinal inertia and longitudinal stress due to warping of the cross section are neglected in developing the classical torsional model.

(7) The interface between the microcantilever and the liquid is a non-slip interface.

(8) The liquid domain is continuous and much larger than the size of the microcantilever.

(9) The liquid is Newtonian with constant viscosity. The flow is incompressible.

(10) There is no source or sink of mass or heat in the fluid domain, and heat transfer effects are ignored.

(11) Body forces (gravitational forces) are ignored.

(12) Applied torsional load is assumed to be purely sinusoidal in time.

(13) Among damping mechanisms, only the viscous damping between the micro-cantilever and the liquid is considered and other energy loss mechanisms such as support damping, surface-effect damping, and thermoelastic damping are ignored.

2.2 Equation of Motion

Based on the assumptions above, the equation of motion of a torsionally vibrating microcantilever in a viscous liquid is derived. The free-body diagram is shown in Figure 2-2, where ρ is the mass density of the microcantilever material, J_p is the polar moment of the cross-section area of the microcantilever, ϕ is the rotational deflection (angle) of the microcantilever in y-z plane, T_x is the internal torque in the microcantilever at the location x, $T_{\text{drive}}(x)e^{j\omega t}$ is the position-dependent sinusoidal excitation torque per unit length applied at an angular frequency of ω, and $T_{\text{hydro}}\left(x, \text{Re}, h/b\right)$ is the resistance torque per unit length from the liquid. The parameter Re is the Reynolds number, a dimensionless number proportional to the ratio of inertial forces to viscous (friction) forces [113-115]. The Reynolds number is defined as

$$\text{Re} = \frac{\rho_l \omega b^2}{4\eta}, \tag{2.1}$$

where ρ_l and η are the mass density and the viscosity of the liquid, respectively. Low Reynolds numbers indicate that the viscous (friction) forces are more important than the inertial forces; the inertial forces could be neglected and the liquid is viscous. On the other hand, high Reynolds numbers indicate that the inertial forces are dominant to the viscous (friction) forces; the viscous forces could be ignored and the liquid is considered

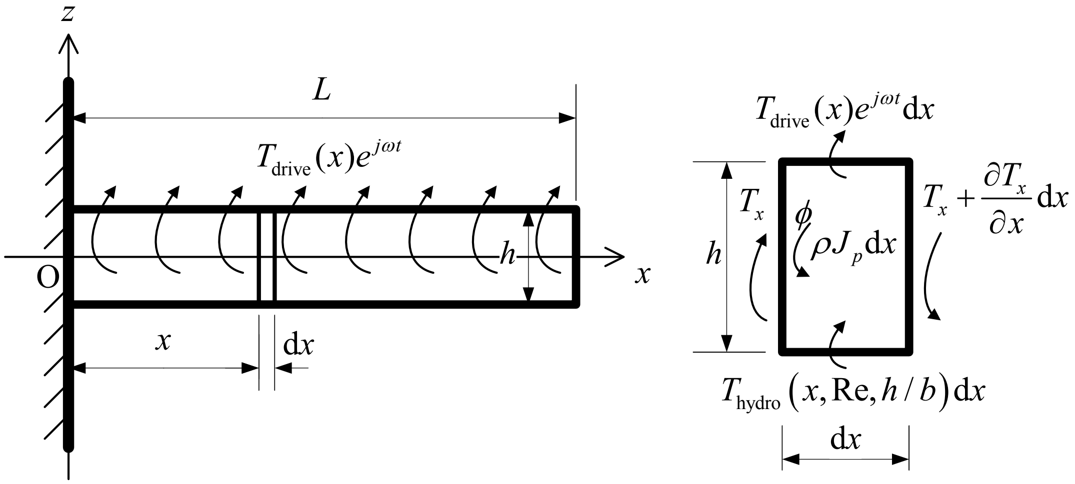

Figure 2-2: Free-body diagram of a torsionally vibrating microcantilever in a viscous liquid.

inviscid. The equation of motion and characteristics for the system in an inviscid liquid can be easily obtained from similar systems in a viscous liquid by setting the viscosity of the liquid to zero, or setting the Reynolds number to infinity.

From the free-body diagram, Figure 2-2, the torque equilibrium in a viscous liquid is expressed by the following equation,

$$\left(T_x + \frac{\partial T_x}{\partial x}\mathrm{d}x\right) - T_x - T_{\text{drive}}(x)e^{j\omega t}\mathrm{d}x + T_{\text{hydro}}\left(x, \mathrm{Re}, \frac{h}{b}\right)\mathrm{d}x = \rho J_p \mathrm{d}x \frac{\partial^2 \phi(x,t)}{\partial t^2}. \tag{2.2}$$

The internal torque in Eq. (2.2) can be obtained using the theory of elasticity and is expressed as follows [110],

$$T_x = GK\frac{\partial \phi(x,t)}{\partial x}. \tag{2.3}$$

In Eq. (2.3), *G* and *K* are the shear modulus and the torsional constant of the microcantilever, respectively. Substituting Eq. (2.3) into Eq. (2.2) and assuming *G* and *K* are constants, the equation of motion is obtained as

$$GK\frac{\partial^2 \phi(x,t)}{\partial x^2} - \rho J_p \frac{\partial^2 \phi(x,t)}{\partial t^2} = T_{\text{drive}}(x)e^{j\omega t} + T_{\text{hydro}}\left(x, \mathrm{Re}, \frac{h}{b}\right). \tag{2.4}$$

The equation of motion is derived from the equilibrium of the torque per unit length. The four terms in Eq. (2.4), from left to right, represent the torques per unit length due to elastic deformation of the microcantilever, the rotational inertia of the microcantilever, the sinusoidal excitation, and the resistance of the liquid, respectively. The last term, the torque per unit length of the liquid resistance, is expressed as

$$T_{\text{hydro}}\left(x, \mathrm{Re}, \frac{h}{b}\right) = g_{1,\text{tors}}\frac{\partial \phi(x,t)}{\partial t} + g_{2,\text{tors}}\frac{\partial^2 \phi(x,t)}{\partial t^2}, \tag{2.5}$$

with

$$g_{1,\text{tors}} = \frac{\pi \rho_l b^4 \omega}{8} \Gamma_{\text{rect,tors,imag}}\left(\text{Re}, \frac{h}{b}\right), \tag{2.6}$$

$$g_{2,\text{tors}} = \frac{\pi \rho_l b^4}{8} \Gamma_{\text{rect,tors,real}}\left(\text{Re}, \frac{h}{b}\right). \tag{2.7}$$

In the above equations, $g_{1,\text{tors}}$ is the frequency-dependent coefficient associated with the liquid damping torque per unit length and is written in terms of the imaginary part of the hydrodynamic function, and $g_{2,\text{tors}}$ is the frequency-dependent coefficient associated with the liquid inertial torque per unit length and is written in terms of the real part of the hydrodynamic function. The hydrodynamic function,

$$\Gamma_{\text{rect,tors}}\left(\text{Re}, \frac{h}{b}\right) = \Gamma_{\text{rect,tors,real}}\left(\text{Re}, \frac{h}{b}\right) + j\Gamma_{\text{rect,tors,imag}}\left(\text{Re}, \frac{h}{b}\right), \tag{2.8}$$

is a dimensionless complex-valued function depending on the Reynolds number and the aspect ratio. The hydrodynamic function is obtained by solving the linearized Navier-Stokes equations for the incompressible viscous liquid [88,113-115]

$$\nabla \cdot \mathbf{v} = 0, \tag{2.9a}$$

$$\rho_l \frac{\partial \mathbf{v}}{\partial t} = -\nabla p + \eta \nabla^2 \mathbf{v}, \tag{2.9b}$$

where p and $\mathbf{v}$ are the hydrodynamic pressure and velocity at a particular point in the liquid, respectively; $\rho_l \partial \mathbf{v} / \partial t$ is the term related to the liquid's inertial forces, while $\eta \nabla^2 \mathbf{v}$ is the term related to the liquid's viscous forces. The values and expressions for the hydrodynamic function will be covered in details in the next chapter.

Solutions to the equation of motion of the torsionally vibrating microcantilever in vacuum will first be obtained. This is done by setting the torque per unit length of the liquid resistance to zero in Eq. (2.4), which is then reduced to [110],

$$GK\frac{\partial^2\phi(x,t)}{\partial x^2}-\rho J_p\frac{\partial^2\phi(x,t)}{\partial t^2}=T_{\text{drive}}(x)e^{j\omega t}. \tag{2.10}$$

It is noted that the boundary conditions for the torsionally vibrating microcantilever in a viscous liquid or in vacuum are the same and given as follows:

$$\phi(0,t)=0, \tag{2.11a}$$

$$\left.\frac{\partial\phi(x,t)}{\partial x}\right|_{x=L}=0. \tag{2.11b}$$

The first boundary condition, Eq. (2.11a), indicates that the microcantilever is perfectly clamped on the left side, that is, there is no rotation at x=0. The second boundary condition, Eq. (2.11b), indicates that the microcantilever is free on the right side, that is, there is no torque at x=L since the torque is proportional to the derivative of the rotational deflection, ϕ, with respect to x from Eq. (2.3).

2.3 Natural Frequency and Mode Shape in Vacuum

Before solving the equation of motion, Eq. (2.4), together with the boundary conditions in Eq. (2.11), to obtain the steady state solution of the rotational deflection response for the system in a viscous liquid, the natural frequency and mode shape for the system in vacuum is first obtained. The i-th undamped natural frequency and mode shape function for the system in vacuum can be obtained by solving the following equation of motion [110], which is based on Eq. (2.10),

$$GK\frac{\partial^2\phi(x,t)}{\partial x^2}-\rho J_p\frac{\partial^2\phi(x,t)}{\partial t^2}=0, \tag{2.12}$$

together with the boundary conditions in Eq. (2.11). By using the method of separation of variables,

$$\phi(x,t) = \bar{\phi}(x)e^{j\omega t}, \tag{2.13}$$

and substituting Eq. (2.13) into Eq. (2.12) and Eq. (2.11), the equation of motion and the relevant boundary conditions are rewritten as

$$GK\frac{\partial^2\bar{\phi}(x)}{\partial x^2} + \rho J_p\omega^2\bar{\phi}(x) = 0, \tag{2.14a}$$

$$\bar{\phi}(0) = 0, \tag{2.14b}$$

$$\left.\frac{\partial\bar{\phi}(x)}{\partial x}\right|_{x=L} = 0. \tag{2.14c}$$

The general solution to Eqs. (2.14a-c) is of the form,

$$\bar{\phi}(x) = A\sin(\lambda x) + B\cos(\lambda x), \tag{2.15}$$

where A and B are unknown amplitude parameters. Substituting Eq. (2.15) into Eqs. (2.14 a-c), the equation of motion and the relevant boundary conditions are rewritten as the following three algebraic equations

$$GK\lambda^2 = \rho J_p\omega^2, \tag{2.16a}$$

$$B = 0, \tag{2.16b}$$

$$A\lambda\cos(\lambda L) = 0. \tag{2.16c}$$

There are infinitely many solutions to Eqs. (2.16a-c). Each solution is associated with one vibration mode. Thus the rotational deflection response, i.e., the general solution to the equation of motion described by Eq. (2.12) is obtained as

$$\phi(x,t) = \sum_{i=1}^{\infty} A_i\sin(\lambda_i x)e^{j\omega_{\text{vac},i}t}, \tag{2.17}$$

where A_i is the unknown parameter determined by the initial conditions, and the i-th undamped natural frequency and mode shape function of the system in vacuum are given by [110],

$$\omega_{\text{vac},i} = \lambda_i \sqrt{\frac{GK}{\rho J_p}}, \tag{2.18a}$$

$$\bar{\phi}_i(x) = \sin\left(\lambda_i x\right). \tag{2.18b}$$

In the above equations, the constant associated with the i-th mode is as follows,

$$\lambda_i = \frac{(2i-1)}{2L}\pi. \tag{2.19}$$

The mode shape function has the following orthogonal properties [110],

$$\int_0^L \bar{\phi}_i(x)\bar{\phi}_k(x)\mathrm{d}x = \begin{cases} \int_0^L \sin^2\left(\lambda_i x\right)\mathrm{d}x = \int_0^L \left[\frac{1}{2} - \frac{1}{2}\cos\left(2\lambda_i x\right)\right]\mathrm{d}x = \frac{L}{2}, & i = k, \\ \int_0^L \frac{1}{2}\left[\cos\left(\frac{i+k-1}{L}\pi x\right) - \cos\left(\frac{i-k}{L}\pi x\right)\right]\mathrm{d}x = 0, & i \neq k, \end{cases} \tag{2.20}$$

and the following special values,

$$\int_0^L \bar{\phi}_i(x)\mathrm{d}x = \int_0^L \sin\left(\lambda_i x\right)\mathrm{d}x = 1/\lambda_i, \tag{2.21a}$$

$$\bar{\phi}_i(L) = (-1)^{i+1}. \tag{2.21b}$$

2.4 Frequency Spectrum

The expression, orthogonal properties and special values of the mode shape functions of the torsionally vibrating system in vacuum, which are obtained in the previous section, will be used to solve the equation of motion for the system in viscous liquids by using the mode superposition method. The steady state rotational deflection response of the torsionally vibrating microcantilever in viscous liquids is obtained here by solving the equation of motion, Eq. (2.4), together with the boundary conditions, Eq. (2.11). Based on the mode superposition method, the steady state rotational deflection response can be expressed as the sum of the each response to each excitation associated with the *i*-th mode shape, i.e.,

$$\phi(x,t)=\sum_{i=1}^{\infty}C_i\bar{\phi}_i(x)e^{j\omega t}, \tag{2.22}$$

where *Ci* is the unknown coefficient representing the weight of contribution from the *i*-th mode to the total response. Substituting Eq. (2.22) into Eq. (2.4), the equation of motion is rewritten as

$$\sum_{k=1}^{\infty}C_k\bar{\phi}_k(x)[GK\lambda_k^2-\omega^2(\rho J_p+g_{2,\text{tors}})+j\omega g_{1,\text{tors}}]=-T_{\text{drive}}(x). \tag{2.23}$$

Multiplying both sides of Eq. (2.23) by the mode shape function, $\bar{\phi}_i(x)$, and integrating through the length of the beam, Eq. (2.23) is rewritten as

$$\int_0^L\bar{\phi}_i(x)\sum_{k=1}^{\infty}C_k\bar{\phi}_k(x)[GK\lambda_k^2-\omega^2(\rho J_p+g_{2,\text{tors}})+j\omega g_{1,\text{tors}}]\mathrm{d}x=-\int_0^L T_{\text{drive}}(x)\bar{\phi}_i(x)\mathrm{d}x,$$

or

$$\sum_{k=1}^{\infty}[GK\lambda_k^2-\omega^2(\rho J_p+g_{2,\text{tors}})+j\omega g_{1,\text{tors}}]C_k\int_0^L\bar{\phi}_i(x)\bar{\phi}_k(x)\mathrm{d}x=-\int_0^L T_{\text{drive}}(x)\bar{\phi}_i(x)\mathrm{d}x. \tag{2.24}$$

Finally, by applying the orthogonal properties of the mode shape functions given by Eq. (2.20), Eq. (2.24) is rewritten as

$$[GK\lambda_i^2-\omega^2(\rho J_p+g_{2,\text{tors}})+j\omega g_{1,\text{tors}}]C_i\frac{L}{2}=-\int_0^L T_{\text{drive}}(x)\bar{\phi}_i(x)\mathrm{d}x. \tag{2.25}$$

Thus, the unknown coefficients are solved and given by

$$C_i=\frac{-2\int_0^L T_{\text{drive}}(x)\bar{\phi}_i(x)\mathrm{d}x}{L[GK\lambda_i^2-\omega^2(\rho J_p+g_{2,\text{tors}})+j\omega g_{1,\text{tors}}]}. \tag{2.26}$$

The steady state rotational deflection response is then given by

$$\phi(x,t)=\sum_{i=1}^{\infty}C_i\bar{\phi}_i(x)e^{j\omega t}=\sum_{i=1}^{\infty}\frac{-2\bar{\phi}_i(x)e^{j\omega t}\int_0^L T_{\text{drive}}(x)\bar{\phi}_i(x)\mathrm{d}x}{L[GK\lambda_i^2-\omega^2(\rho J_p+g_{2,\text{tors}})+j\omega g_{1,\text{tors}}]}. \tag{2.27}$$

Assuming the excitation torque per unit length is uniform along the x axis, i.e., $T_{\text{drive}}(x)=-\bar{T}_{\text{drive}}$, and applying Eq. (2.21), the rotational deflection response of the system in viscous liquids is obtained as follows,

$$\phi(x,t)=\sum_{i=1}^{\infty}\frac{2\bar{\phi}_i(x)\bar{T}_{\text{drive}}e^{j\omega t}}{\lambda_i L[GK\lambda_i^2-\omega^2(\rho J_p+g_{2,\text{tors}})+j\omega g_{1,\text{tors}}]}. \tag{2.28}$$

Evaluating Eq. (2.28) at $x=L$, the magnitude of the dynamic tip rotational deflection is given by,

$$|\phi(L,t)|=\left|\sum_{i=1}^{\infty}\frac{2(-1)^{i+1}\bar{T}_{\text{drive}}}{\lambda_i L\sqrt{[GK\lambda_i^2-\omega^2(\rho J_p+g_{2,\text{tors}})]^2+(\omega g_{1,\text{tors}})^2}}\right|. \tag{2.29}$$

Furthermore, evaluating Eq. (2.29) at $\omega=0$, the magnitude of the static tip rotational deflection is obtained as

$$|\phi_{\text{static}}(L)|=|\phi(L,t)|_{\omega=0}=\left|\sum_{i=1}^{\infty}\frac{2(-1)^{i+1}\bar{T}_{\text{drive}}}{\lambda_i^3 LGK}\right|=\left|\sum_{i=1}^{\infty}\frac{(2L)^3 2(-1)^{i+1}\bar{T}_{\text{drive}}}{(2i-1)^3\pi^3 LGK}\right|,$$

or

$$|\phi_{\text{static}}(L)|=\left|\frac{\bar{T}_{\text{drive}}L^2}{2GK}\frac{32}{\pi^3}\sum_{i=1}^{\infty}\frac{(-1)^{i+1}}{(2i-1)^3}\right|=\left|\frac{\bar{T}_{\text{drive}}L^2}{2GK}\right|. \tag{2.30}$$

The normalized tip rotational deflection is the ratio of the magnitude of the dynamic tip rotational deflection, $|\phi(L,t)|$, to the static tip rotational deflection, $|\phi_{\text{static}}(L)|$, by using unit of dB,

$$\bar{\phi}_{\text{norm, tip}} = 20\log_{10}\left|\sum_{i=1}^{\infty}\frac{4(-1)^{i+1}GK}{\lambda_i L^3\sqrt{[GK\lambda_i^2-\omega^2(\rho J_p+g_{2,\text{tors}})]^2+(\omega g_{1,\text{tors}})^2}}\right|. \tag{2.31}$$

By using Eq. (2.31), the frequency spectrum can be obtained by calculating the normalized tip rotational deflection in terms of the excitation frequency.

2.5 Resonance Frequency

By solving the equation of motion, Eq. (2.4), the resonance frequency of the system can be obtained. For the microcantilever in vacuum, the resonance frequency is the same as the natural frequency and is given by Eq. (2.18a). For the microcantilever in a liquid, the liquid could be treated as an inviscid liquid or a viscous liquid.

For the microcantilever with low aspect ratio (*h*/*b*) immersed in an inviscid liquid, the *i*-th resonance frequency was obtained by Chu [51],

$$\omega_{\text{InvL},i} = 2\pi f_{\text{InvL},i} = \omega_{\text{vac},i}\left(1+\frac{3\pi\rho_l b}{32\rho h}\right)^{-1/2}. \tag{2.32}$$

Eq. (2.32) indicates that for a rectangular microcantilever characterized by its density and geometry (length, width, and thickness) in an inviscid liquid characterized by its density, the resonance frequency is always less than that in vacuum and the ratio between them is dependent on the ratio of their density and the aspect ratio (*h*/*b*).

For the microcantilever immersed in a viscous liquid, assuming that only the *i*-th torsional mode is excited, i.e.,

$$T_{\text{drive}}(x) = T_{\text{drive},i}\sin\lambda_i x, \tag{2.33}$$

and the vibration shape is given by the *i*-th undamped mode shape

$$\phi(x,t) = \Phi(t)\sin\lambda_i x. \tag{2.34}$$

The system will behave as a simple harmonic oscillator and the equation of motion, Eq. (2.4), can be rewritten as

$$(\rho J_p + g_{2,\mathrm{tors}})\frac{\partial^2\Phi(t)}{\partial t^2} + g_{1,\mathrm{tors}}\frac{\partial\Phi(t)}{\partial t} + GK\lambda_i^2\Phi(t) = T_{\mathrm{drive},i}e^{j\omega t}. \tag{2.35}$$

For the single degree of freedom (SDOF) system,

$$m\frac{\partial^2\Phi(t)}{\partial t^2} + c\frac{\partial\Phi(t)}{\partial t} + k\Phi(t) = F_0\cos\omega t, \tag{2.36}$$

its undamped natural frequency, damping ratio, and resonance frequency are given, respectively, by

$$\omega_{\mathrm{n}} = 2\pi f_n = \sqrt{\frac{k}{m}}, \tag{2.37}$$

$$\xi = \frac{c}{2\sqrt{mk}} = \frac{c}{2m\omega_{\mathrm{n}}}, \tag{2.38}$$

$$\omega_r = 2\pi f_r = \omega_n\sqrt{1-2\xi^2} = \sqrt{(1-2\xi^2)k/m}. \tag{2.39}$$

It is noted that Eq. (2.38) indicates $\xi > 0$ and Eq. (2.39) requires $\xi < \sqrt{2}/2$. In order to apply the above formula, the damping ratio of the system has to meet the requirement $0 < \xi < \sqrt{2}/2$. Such system is called moderately underdamped vibration system. For sensor applications, the damping ratio of the system is less than 0.5 and the above requirement is always met.

Comparing Eq. (2.35) and Eq. (2.36), the following relations are found,

$$m = \rho J_p + g_{2,\mathrm{tors}}, \tag{2.40a}$$

$$c = g_{1,\mathrm{tors}}, \tag{2.40b}$$

$$k = GK\lambda_i^2. \tag{2.40c}$$

Substituting Eqs. (2.40a-c) into Eqs. (2.37-2.39), the damping ratio and the resonance frequency associated with the *i*-th mode are given by

$$\xi_i = \frac{g_{1,\mathrm{tors}}}{2\omega(\rho J_p + g_{2,\mathrm{tors}})}, \tag{2.41}$$

$$\omega_{\mathrm{VisL},i} = 2\pi f_{\mathrm{VisL},i} = \omega_{\mathrm{vac},i}\sqrt{1-2\xi_i^2}\left[1+\frac{g_{2,tors}}{\rho J_p}\right]^{-1/2}. \tag{2.42}$$

For the cases where the Reynolds number is high, the energy loss is low, $\xi_i << 1$, and the general expression of the resonance frequency in Eq. (2.42) is reduced to

$$\omega_{\mathrm{Approx,VisL},i} = 2\pi f_{\mathrm{Approx,VisL},i} = \omega_{\mathrm{vac},i}\left[1+\frac{g_{2,tors}}{\rho J_p}\right]^{-1/2}, \tag{2.43}$$

which is identical to the expression obtained for the resonance frequency of torsionally vibrating microcantilevers in viscous liquids when low loss is assumed [88]. Eq. (2.43) indicates that the resonance frequency in a viscous liquid is always less than the one in vacuum and the ratio of the two frequencies is dependent on the ratio of their inertias, i.e., the ratio of the liquid's added moment of inertia to the microcantilever's moment of inertia. For transversely or laterally vibrating microcantilevers in viscous liquids, these relationships are the same except that the inertias are given by the masses rather than the moments of inertia.

Furthermore, for a rectangular microcantilever with low aspect ratio (*h*/*b*) in an inviscid liquid, the general expression for the resonance in Eq. (2.42) can be further reduced to Eq. (2.32). The polar moment of area of a rectangular microcantilever with low aspect ratio (*h*/*b*) is approximated as [88,116]

$$J_p \approx \frac{b^3 h}{12}. \tag{2.44}$$

Substituting Eq. (2.7) and Eq. (2.44) into Eq. (2.43), the resonance frequency is rewritten as

$$\omega_{\mathrm{InvL},i} = 2\pi f_{\mathrm{InvL},i} = \omega_{\mathrm{vac},i}\left[1+\frac{3\pi\rho_l b}{2\rho h}\Gamma_{\mathrm{rect,tors,real}}\left(\mathrm{Re}=\infty, \frac{h}{b}=0\right)\right]^{-1/2}, \tag{2.45}$$

In comparing Eq. (2.32) and Eq. (2.45), it is shown that the real part of the hydrodynamic function in this case is 1/16, i.e.,

$$\Gamma_{\mathrm{rect,tors,real}}\left(\mathrm{Re}=\infty, \frac{h}{b}=0\right)=\frac{1}{16}=0.0625. \tag{2.46}$$

Finally, Eq. (2.45) can be reduced to the resonance frequency in vacuum by setting the density of the liquid to 0.

2.6 Quality Factor

As mentioned in the previous chapter, the quality factor is an important design parameter for resonant MEMS devices in various applications including sensor applications. The quality factor is defined as 2π times the ratio of the peak energy stored in a vibrating system to the energy lost per cycle, i.e.,

$$Q = 2\pi\frac{\text{Maximum Energy Stored in one cycle}}{\text{Energy Loss in the same cycle}}. \tag{2.47}$$

Before solving for the quality factor of the torsionally vibrating microcantilever in a viscous liquid, the quality factor of the moderately underdamped vibration system described by Eq. (2.36) is first obtained. For this system, the transfer function is given by

$$H(f)=\frac{H_0}{1-\left(\frac{f}{f_n}\right)^2+2\xi\frac{f}{f_n}j}=\left|H(f)\right|e^{-j\varphi(f)}. \tag{2.48}$$

From Eq. (2.48), the magnitude and phase of the transfer function are obtained as,

$$\left|H(f)\right| = \frac{H_0}{\sqrt{\left[1-\left(\frac{f}{f_0}\right)^2\right]^2 + 4\xi^2\left(\frac{f}{f_0}\right)^2}}, \tag{2.49}$$

$$\varphi(f) = \arctan\frac{2\xi\frac{f}{f_0}}{1-\left(\frac{f}{f_0}\right)^2}. \tag{2.50}$$

The steady state response of the system is given by

$$\Phi(t) = F_0\left|H(f)\right|\cos(\omega t-\varphi). \tag{2.51}$$

Here, H_0 is the transfer function of the static system, which is the ratio of the static response Φ_0 to the maximum excitation F_0 and is expressed as

$$H(f=0) = H_0 = \frac{\Phi_0}{F_0} = \frac{1}{k}. \tag{2.52}$$

Substituting Eq. (2.39) into (2.49-2.50), the magnitude and phase of the transfer function at the resonance frequency are given by,

$$\left|H(f_r)\right| = \frac{H_0}{2\xi\sqrt{1-\xi^2}} = H_{\max}, \tag{2.53}$$

$$\varphi(f_r) = \arctan\frac{\sqrt{1-2\xi^2}}{\xi}. \tag{2.54}$$

In order to evaluate Eq. (2.47) to obtain the quality factor, it is necessary to first calculate the kinetic energy, potential energy, total energy and energy loss per cycle of the steady state system, respectively. The kinetic energy is due to the motion of the system, which is defined and calculated as

$$U_k = \frac{1}{2} m \left(\frac{\partial \Phi}{\partial t} \right)^2 = \frac{1}{2} m\omega^2 F_0^2 \left| H\left(f\right) \right|^2 \sin^2\left(\omega t - \varphi\right). \tag{2.55}$$

The potential energy is due to the position and deformation, which is defined and calculated as

$$U_p = \frac{1}{2} k \Phi^2 = \frac{1}{2} k F_0^2 \left| H\left(f\right) \right|^2 \cos^2\left(\omega t - \varphi\right). \tag{2.56}$$

The total energy is the sum of both kinetic energy and potential energy, and is given by

$$U_t = U_p + U_k = \frac{1}{2} F_0^2 \left| H\left(f\right) \right|^2 \left[k\cos^2\left(\omega t - \varphi\right) + m\omega^2 \sin^2\left(\omega t - \varphi\right) \right]. \tag{2.57}$$

The energy loss per cycle is the work done by the damping (friction) forces during each vibration period and given by

$$\Delta W = \int_0^{2\pi/\omega} c \left(\frac{\partial \Phi}{\partial t} \right) \left(\frac{\partial \Phi}{\partial t} \right) dt = \pi F_0^2 \left| H\left(f\right) \right| c\omega \left| H\left(f\right) \right|. \tag{2.58}$$

By calculating the first and second derivatives of the total energy, the ranges of the total energies for different excitation frequency are obtained as

$$\begin{cases} U_{k,\max} \le U_{tot} \le U_{p,\max}, & f < f_0, \\ U_{p,\max} = U_{tot} = U_{k,\max}, & f = f_0, \\ U_{p,\max} \le U_{tot} \le U_{k,\max}, & f > f_0, \end{cases} \tag{2.59}$$

where $U_{k,\max}$ and $U_{p,\max}$ are the maximum kinetic energy and maximum potential energy during one cycle, respectively. So the maximum total energy for each case of the excitation frequency range is given, respectively, by

$$\begin{cases} U_{t,\max} = U_{p,\max}, & f < f_0, \\ U_{t,\max} = U_{p,\max} = U_{k,\max}, & f = f_0, \\ U_{t,\max} = U_{k,\max}, & f > f_0. \end{cases} \tag{2.60}$$

For this system, the quality factor defined by Eq. (2.47) is given by

$$Q(f) = 2\pi \frac{U_{t,\max}}{\Delta W}. \tag{2.61}$$

Substituting Eq. (2.60) into Eq. (2.61), the quality factor is rewritten as

$$Q(f) = \begin{cases} \dfrac{f_0}{2\xi f}, & f < f_0, \\ \dfrac{1}{2\xi}, & f = f_0, \\ \dfrac{f}{2\xi f_0}, & f > f_0. \end{cases} \tag{2.62}$$

Since $f_r = f_0\sqrt{1-2\xi^2} < f_0$, the quality factor of the SDOF system at its resonance frequency is given by

$$Q(f_r) = \frac{1}{2\xi\sqrt{1-2\xi^2}}. \tag{2.63}$$

From Eq. (2.35), based on Eq. (2.41) and Eq. (2.63), the quality factor of the torsionally vibrating microcantilevers in viscous liquids can be obtained as

$$Q_{\text{tors}} = \frac{1}{2\xi_i\sqrt{1-2\xi_i^2}} = \frac{\rho J_p + g_{2,\text{tors}}}{g_{1,\text{tors}}/\omega}\left[1 - \frac{1}{2}\left(\frac{g_{1,\text{tors}}/\omega}{\rho J_p + g_{2,\text{tors}}}\right)^2\right]^{-1/2}. \tag{2.64}$$

For the cases where the Reynolds number is high, the energy loss is low, $\xi_i << 1$, and the expression of the quality factor in Eq. (2.64) is reduced to

$$Q_{\text{approx,tors}} = \frac{1}{2\xi_i} = \frac{\rho J_p + g_{2,\text{tors}}}{g_{1,\text{tors}}/\omega}, \tag{2.65}$$

which is identical to the expression obtained for the quality factor of torsionally vibrating microcantilevers in viscous liquids when low loss is assumed [88]. Eq. (2.65) indicates that the quality factor equals the ratio of the total inertia of the microcantilever and liquid to the damping parameter divided by the excitation frequency. For transversely or laterally vibrating microcantilevers in viscous liquids, this relationship is the same except that the inertias are given by masses rather than moments of inertia and the damping parameter is associated with the transverse or lateral mode rather than the torsional mode.

In order to calculate the frequency spectrum, resonance frequency and quality factor of a torsionally vibrating rectangular microcantilever in a viscous liquid, the expressions for the hydrodynamic function, the torsional constant and the polar moment of area have to be determined.

2.7 Thickness Effects on Rectangular Microcantilevers

The equations to calculate the frequency spectrum, resonance frequency, and quality factor of the torsionally vibrating microcantilevers in viscous liquids are expressed in terms of the hydrodynamic function, Γ, the torsional constant, *K*, and the polar moment of area, J_p. When calculating the resonance frequency and the quality factor of the torsionally vibrating rectangular microcantilevers in viscous liquids for the ribbon case [88], the thickness effects have been ignored. In the ribbon case, the hydrodynamic function is in terms of only the Reynolds number and is given by [88]

$$\Gamma_{\text{ribbon,rect,tors,real}} = \Gamma_{\text{rect,tors,real}}(\text{Re}, h/b = 0), \tag{2.66a}$$

$$\Gamma_{\text{ribbon,rect,tors,imag}} = \Gamma_{\text{rect,tors,imag}}(\text{Re}, h/b = 0). \tag{2.66b}$$

The torsional constant is approximated by [88,116]

$$K_{\text{ribbon}} = \frac{bh^3}{3}, \tag{2.67}$$

and the polar moment of area is approximated by [88,116]

$$J_{p,\text{ribbon}} = \frac{b^3 h}{12}. \tag{2.68}$$

Although the infinitely thin approximation in the ribbon case yields accurate results for transverse motion for moderately thin rectangular microcantilevers over a large range of aspect ratios (*h*/*b*), torsional or lateral motion of microcantilevers with high aspect ratio (*h*/*b*) is found to be poorly described by this infinitely thin model. The thickness effects should be taken into account when evaluating the hydrodynamic function, the polar moment of area, and the torsional constant of microcantilevers with high aspect ratio (*h*/*b*).

In the present study, the thickness effects on the hydrodynamic function, the torsional constant, and the polar moment of area are considered as follows:

$$\Gamma_{\text{rect,tors,real}} = \Gamma_{\text{rect,tors,real}}(\text{Re}, h/b) > \Gamma_{\text{rect,tors,real}}(\text{Re}, h/b = 0), \tag{2.69a}$$

$$\Gamma_{\text{rect,tors,imag}} = \Gamma_{\text{rect,tors,imag}}(\text{Re}, h/b) > \Gamma_{\text{rect,tors,imag}}(\text{Re}, h/b = 0), \tag{2.69b}$$

$$K = \frac{2bh^3}{k_2} < \frac{bh^3}{3}, \tag{2.70}$$

$$J_p = \frac{b^3 h + bh^3}{12} > \frac{b^3 h}{12}. \tag{2.71}$$

Values of the parameter k_2 in terms of the aspect ratio (*h*/*b*) are given in Table 2-1 [109]. The ribbon theory underestimates the real and imaginary parts of the hydrodynamic

Table 2-1: Parameter k_2 for torsional constant [109]

h*/*b	11	22/3	11/2	22/5	11/3	11/4	11/5	11/10	0
k_2	14.2	10.2	8.73	8.03	7.60	7.12	6.87	6.41	6

function since it underestimates the added inertia and damping by ignoring the thickness of the microcantilever. From Table 2-1, the value of parameter k_2 for a microcantilever is greater than 6, so the ribbon theory overestimates the torsional constant. Eq. (2.71) indicates that the ribbon theory also underestimates the polar moment of area.

Thickness effects on the hydrodynamic function, the torsional constant, and the polar moment of area affect the calculated values of the characteristics of microcantilevers vibrating torsionally, such as the resonance frequency and the quality factor. Substituting Eq. (2.18a) and Eq. (2.19) into Eq. (2.42), the resonance frequency for torsional mode is rewritten by

$$f_{r,i} = \frac{2i-1}{4L}\sqrt{\frac{GK(1-2\xi_i^2)}{\rho J_p + g_{2,\text{tors}}}}. \tag{2.72}$$

The resonance frequency calculated by Eq. (2.72) and quality factor calculated by Eq. (2.64) indicate that, for torsional modes, increasing hydrodynamic function decreases the calculated values of both the resonance frequency and quality factor. Increasing torsional constant increases the calculated values of both the resonance frequency and quality factor. Increasing polar moment of area decreases the calculated values of the resonance frequency but increases the calculated values of the quality factor. Compared to the ribbon theory, the thickness effects on both hydrodynamic function and torsional constant decreases the calculated values of both the resonance frequency and quality factor; on the other hand, the thickness effect on polar moment of area decreases the calculated values of the resonance frequency, but increases the calculated values of the quality factor.

3. HYDRODYNAMIC FUNCTION OF A TORSIONALLY VIBRATING RECTANGULAR MICROCANTILEVER IN A VISCOUS LIQUID

3.1 Introduction

In the previous chapter, the equation of motion for a torsionally vibrating microcantilever in a viscous liquid, which is described by Eq. (2.4), is derived and appropriate solutions are found; the expressions to calculate the frequency spectrum, resonance frequency and quality factor are obtained. In order to evaluate the characteristics of the vibrating system, the expressions or values of the hydrodynamic function must be first obtained. The hydrodynamic function is obtained by comparing the excitation velocity and the normalized torque per unit length acted on the microcantilever from the surrounding liquid. The torque per unit length is obtained from the integral of the torque per unit area along the boundary of the cross-section of the microcantilever. The torque per unit area at a specific point on the boundary is induced by two hydrodynamic stresses: the normal stress, whose direction is perpendicular to the border, and the shear stress, whose direction is parallel to the border. The total stress is equal to the vector sum of the normal stress and the shear stress. The distributions of total, normal and shear stresses along the boundary of the cross-section of a rigid rectangular microcantilever in a viscous liquid are depicted in Figure 3-1. In this case, the hydrodynamic torque per unit length is given by

$$\begin{aligned} T_{\mathrm{hydro}}(t) \quad = \quad & 4\int_0^{h/2}\left[\sigma_{yz}(b/2,z,t)b/2-\sigma_{yy}(b/2,z,t)z\right]\mathrm{d}z \\ & +4\int_0^{b/2}\left[\sigma_{zz}(y,h/2,t)y-\sigma_{yz}(y,h/2,t)h/2\right]\mathrm{d}y, \end{aligned} \tag{3.1}$$

where σ_{yy} and σ_{zz} are the normal stresses, σ_{yz} is the shear stress, and t is the time. The normalized torque per unit length is defined by

$$\hat{T}_{\text{hydro}}(t) = \frac{T_{\text{hydro}}(t)}{\pi b \eta \operatorname{Re} v_m}, \tag{3.2}$$

where b is the width of the microcantilever, η is the viscosity of the liquid, Re is the Reynolds number, and v_m is the maximum magnitude of the excitation velocity and is given by

$$v_m = \frac{\omega \sqrt{b^2 + h^2}}{2} \phi_m, \tag{3.3}$$

where ω is the excitation frequency, h is the thickness of the microcantilever, and ϕ_m is the maximum magnitude of the rotational deflection. For the ribbon case, the thickness (h)

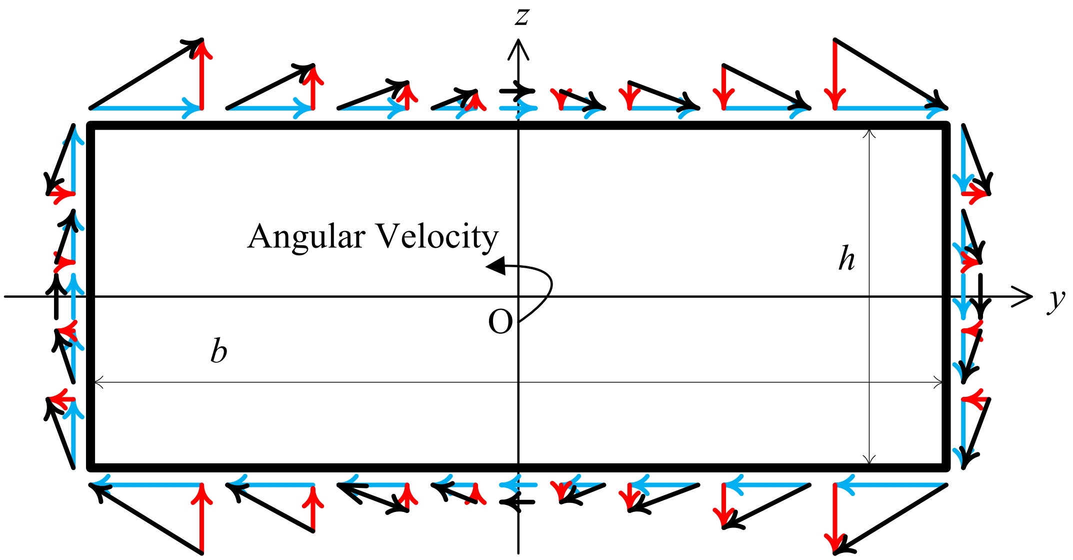

Figure 3-1: Hydrodynamic total stresses (in black), normal stresses (in red), and shear stresses (in blue) acting on the surfaces of a rigid rectangular cross-section of a torsionally vibrating microcantilever in a viscous liquid.

is much less than the width (b) and the maximum magnitude of the excitation velocity is approximated by

$$v_m \approx \frac{\omega b}{2}\phi_m. \tag{3.4}$$

Substituting Eq. (3.4) and the definition of the Reynolds number described by Eq. (2.1) into Eq. (3.2), the normalized torque per unit length for the ribbon case is rewritten as

$$\hat{T}_{\text{hydro}}(t) = \frac{T_{\text{hydro}}(t)}{\pi\omega^2\rho_l b^4\phi_m / 8}. \tag{3.5}$$

This definition in the time domain is equivalent to the definition in the frequency domain for the ribbon case [88].

If the cross-section of the rigid microcantilever is circular, an analytical expression of the hydrodynamic function is given by the well-known expression [87]

$$\Gamma_{\text{circ,tors}}(\omega) = \frac{2j}{\text{Re}} + \frac{jK_0(-j\sqrt{j\,\text{Re}})}{\sqrt{j\,\text{Re}}K_1(-j\sqrt{j\,\text{Re}})}. \tag{3.6}$$

In Eq. (3.6), j is the imaginary unit, Re is the Reynolds number, and the functions K_0 and K_1 are modified Bessel functions of the third kind.

If the cross-section of the rigid microcantilever is rectangular, the analytical expression of the hydrodynamic function obtained by the infinitely thin model for the ribbon case is given by [88]

$$\Gamma_{\text{rect,tors}}(\omega) = \left(\frac{5Re - 15\ln(Re) + 8}{80(Re+1)}\right)\frac{\Gamma_{r1}}{\Gamma_{r2}} + j\left(\frac{0.41}{\sqrt{Re}} + \frac{1}{Re}\right)\frac{\Gamma_{i1}}{\Gamma_{i2}}, \tag{3.7a}$$

with

$$\begin{aligned}\Gamma_{r1} = 4.17950 - 0.25269\,\tau + 2.88308\tau^2 - 0.08680\tau^3 \\ + 0.33837\tau^4 + 0.03318\tau^5 + 0.01884\tau^6,\end{aligned} \tag{3.7b}$$

$$\Gamma_{r2} = 1 - 2.27659\,\tau + 2.10179\tau^2 - 0.11365\tau^3 + 0.34989\tau^4 + 0.03779\tau^5 + 0.01884\tau^6, \tag{3.7c}$$

$$\Gamma_{i1} = 0.82494 - 0.67701\,\tau + 0.41150\tau^2 - 0.16748\tau^3 + 0.04897\tau^4 - 0.01107\tau^5 + 0.00148\tau^6, \tag{3.7d}$$

$$\Gamma_{i2} = 1 - 0.72962\,\tau + 0.40663\tau^2 - 0.16517\tau^3 + 0.04907\tau^4 - 0.01110\tau^5 + 0.00148\tau^6, \tag{3.7e}$$

$$\tau = \log(\mathrm{Re}). \tag{3.7f}$$

It is apparent that the above expression for the ribbon case is very complex with many terms. This analytical expression of the hydrodynamic function is well approximated by the simple dependence on the nondimensional thickness of the viscous layer surrounding the microcantilever, $\mathrm{Re}^{-0.5}$. The numerical coefficients were determined through least square fitting to the above analytical expression and is given by [93]

$$\Gamma_{\mathrm{rect,tors,approx}}(\omega) = (0.0634 + 0.388\,\mathrm{Re}^{-0.5}) + j(0.400\,\mathrm{Re}^{-0.5}). \tag{3.8}$$

In the range of Reynolds numbers from 100 to 50,000, the maximum relative deviations between the approximated simple fit of Eq. (3.8) and the complex analytical expression of Eqs. (3.7a-f) are less than 1.1% for the real part and 2.5% for the imaginary part.

The infinitely thin model used to solve for the above expression of the hydrodynamic function for the ribbon case is semi-analytical. For the case of a microcantilever with finite thickness, the problem to obtain an expression of the hydrodynamic function described by Eq. (2.8) is even more complex and cannot be solved by a pure analytical method. A numerical method will be used to solve for the values of the hydrodynamic function for a set of different Reynolds numbers and aspect ratios (*h*/*b*). An analytical expression for the hydrodynamic function will then be obtained by fitting the numerical results.

3.2 Numerical Evaluation of the Hydrodynamic Function for Rectangular Microcantilevers

3.2.1 Simulation Procedure and Model Validation

In order to calculate the values of the hydrodynamic function at specific Reynolds numbers and aspect ratios (*h*/*b*), 2D numerical simulations by COMSOL are used to extract the torque per unit length of the torsionally vibrating microcantilevers in viscous liquids as a function of time. In these models based on the finite element method (FEM), the rectangular cross-sections of the microcantilevers are assumed to be rigid with a constant width and variable thickness. The surrounding liquid domain, a square with the same center as the cross-section of the microcantilever, is modeled as an incompressible fluid governed by the linearized Navier-Stokes equations. A typical FEM mesh is shown in Figure 3-2.

The boundary conditions are applied on both the inner boundary and the outer boundary. On the inner boundary, a sinusoidal angular excitation velocity is imposed and

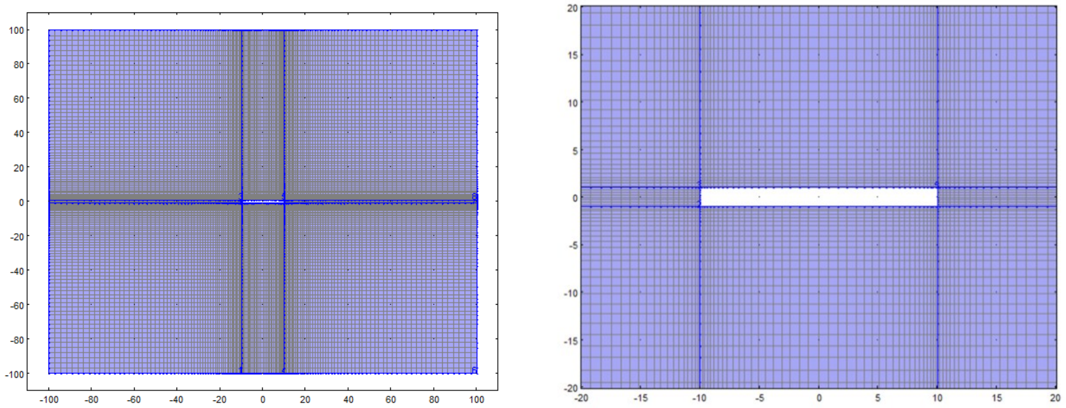

Figure 3-2: A typical mesh of the FEM model of a viscous liquid surrounding to a rigid rectangular cross-section of the torsionally vibrating microcantilever: the whole model (Left) & the center part (Right).

the equivalent velocity components in the y and z directions are as follows,

$$v_y = -\frac{2v_m z\cos(\omega t)}{\sqrt{h^2+b^2}}, \tag{3.9a}$$

$$v_z = -\frac{2v_m y\cos(\omega t)}{\sqrt{h^2+b^2}}. \tag{3.9b}$$

where v_m is the maximum magnitude of the excitation velocity, h and b are the thickness and width of the microcantilever, respectively, ω is the excitation frequency, and t is the time. On the outer boundary, the pressure of the liquid and the viscous stress are set to zero.

While the amplitude of the excitation velocity is held constant, the excitation frequency is varied in order to investigate the effect of different Reynolds numbers. The liquid's mass density and viscosity are set to those of water (ρ_l = 1000 kg/m^3 and η = 1 cP). A transient analysis is performed over three cycles, which is verified to be long enough to let the system reach steady state. The torque per unit length is then extracted as a function of time from the integral of the torque per unit area induced by the hydrodynamic normal stresses and shear stresses along the entire inner boundary. A typical numerical result of the torque per unit length from COMSOL is shown as the blue dots in Figure 3-3.

Furthermore, the thickness of the microcantilever is varied in different models in order to investigate the effect of different aspect ratios. Both the excitation frequency and the thickness of the microcantilever are varied in order to find the real and imaginary parts of hydrodynamic function in terms of both the Reynolds number, Re, and aspect ratio *h/b*.

In this study, microcantilevers with 11 different aspect ratios (0.001, 0.002, 0.005, 0.01, 0.02, 0.05, 0.1, 0.2, 0.3, 0.5, 1) vibrating with 19 different Reynolds numbers (1, 1.778, 3.162, 5.623, 10, 17.78, 31.62, 56.23, 100, 177.8, 316.2, 562.3, 1000, 1778, 3162, 5623, 10000, 17780, 31620) are investigated. This represents a total of 209 calculation cases. The investigated aspect ratios are chosen based on the fitting attempts which assume that the hydrodynamic function is approximately proportional to the aspect ratio. This "linear" dependence is confirmed when the analytical expression is obtained by fitting the numerical results. The investigated Reynolds numbers, whose logarithms to base 10 are from 0 to 4.5 with interval of 0.25, are chosen based on the assumption that

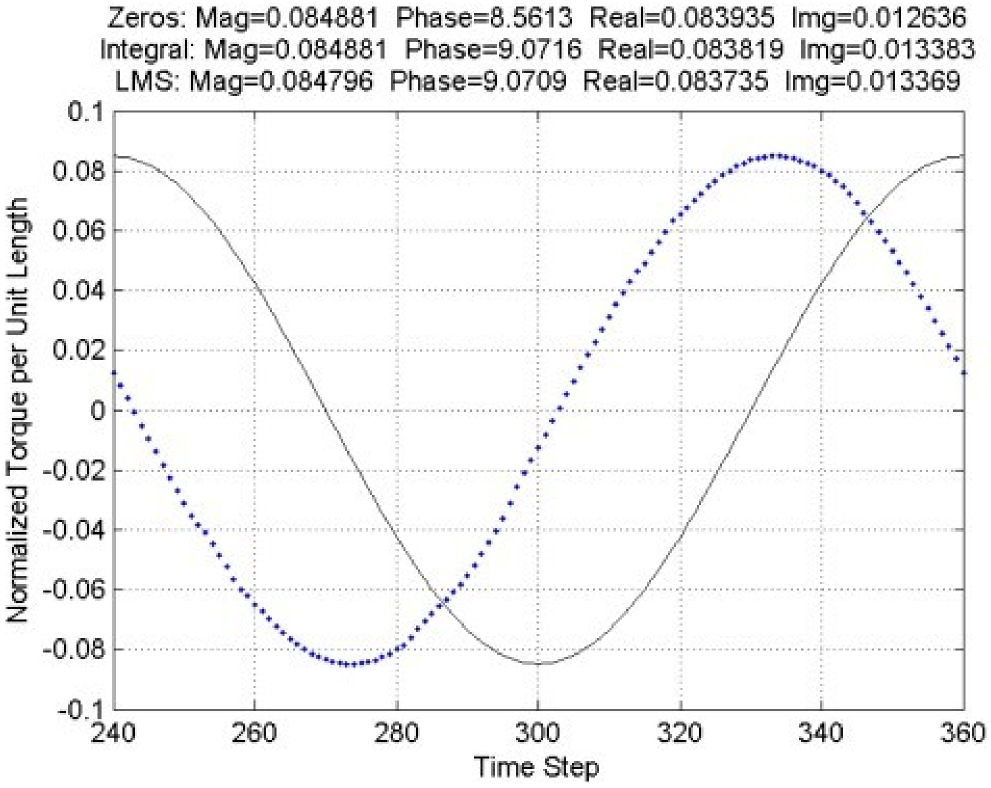

Figure 3-3: Normalized torque per unit length (blue dots), the excitation velocity (black solid), and the results on the magnitude, phase, real part and imaginary part of the hydrodynamic function for Re=1000 and *h/b*=0.1.

the hydrodynamic function is proportional to the power function of the Reynolds numbers, Re^{-a}, where the unknown index, a, is obtained by fitting. This power function dependence is extended from the simple dependence, $\mathrm{Re}^{-0.5}$, for the ribbon case.

In order to validate our numerical model, a convergence study is performed to identify an appropriate mesh distribution, mesh size, and time interval between data points. In our final model, the mesh size is much smaller around the microcantilever's cross-section since higher gradients occur near the microcantilever. For each calculation case, with specific Reynolds number and aspect ratio, several models with different mesh sizes and time intervals are created and the convergence is proved by the fact that the difference in the numerical results from these models are very small and negligible.

3.2.2 Methods to Extract the Magnitude, Phase, Real Part, and Imaginary Part of the Hydrodynamic Function

Based on the numerical results (from COMSOL) for the magnitude and phase offset from the angular excitation velocity; the real and imaginary parts of the hydrodynamic function are then calculated. The magnitude and phase of the hydrodynamic function are calculated by the following three methods: zero comparison, average by integral on the last cycle [82], and the least square method (LSM). All of these three methods need the assumption that the numerical results (normalized torque per unit length) are sinusoidal with time.

The first method is to compare the two zeros of both the normalized torque per unit length and the angular excitation velocity in the last cycle in order to obtain the phase offsets between them. The phase of the hydrodynamic function is the average of the two phase offsets subtracted from $\pi/2$,

$$\alpha_0 = \frac{\pi}{2} - \frac{1}{2}\left(\frac{nInterval/4{+}1\text{-}n0a}{nInterval} 2\pi + \frac{3nInterval/4{+}1\text{-}n0b}{nInterval} 2\pi \right), \tag{3.10}$$

where *nInterval* is the number of the time intervals between data points in one cycle, *n0a* and *n0b* is the interpolated time step number of the two values for the normalized torque per unit length, which are closest to 0 and with opposite signs. For instance, *n0a* is between 242 and 243 for the calculation case shown in Figure 3-3 since the first zero of the normalized torque per unit length during the last cycle occurs at the moment between the time step #242 and #243. In this case, *n0a* is given by linear interpolation,

$$n0a = 242 + \frac{\hat{T}_{242}}{\hat{T}_{242} - \hat{T}_{243}}, \tag{3.11}$$

where $\hat{T}_{242}$ and $\hat{T}_{243}$ are the normalized torques per unit length at the time step #242 and #243, respectively.

The second method is to obtain the average phase of the hydrodynamic function by calculating the integral/summation of the product of the numerical results and the angular excitation velocity [82],

$$\alpha_{\text{Int}} = \frac{\pi}{2} \text{-} \arccos\left[\frac{2}{sMax \cdot nInterval} \sum_{k=1}^{nInterval} \hat{T}_k \cos\frac{2\pi k}{nInterval} \right], \tag{3.12}$$

where *sMax* is the maximum value and $\hat{T}_k$ is the normalized torque per unit length at the time step *k* in the last cycle.

For the above two methods, the magnitude of the hydrodynamic function is the maximum value of the normalized torque per unit length in the last cycle.

The third method is to use the least square method to obtain the fitting expression (sinusoidal with time and the magnitude is $|\Gamma|$) for the numerical results and then compare to the angular excitation velocity to get the phase of the hydrodynamic function as follows,

$$\left|\Gamma\right| = \sqrt{s_1^2 + s_2^2}, \tag{3.13a}$$

$$\alpha_{\mathrm{LSM}} = \frac{\pi}{2} + \arctan\frac{s_2}{s_1}, \tag{3.13b}$$

with

$$s_1 = \frac{\sum_{k=1}^{nInterval} \hat{T}_k \cos\frac{2\pi k}{nInterval}}{\sum_{k=1}^{nInterval} \cos^2\frac{2\pi k}{nInterval}}, \tag{3.14a}$$

$$s_2 = \frac{\sum_{k=1}^{nInterval} \hat{T}_k \sin\frac{2\pi k}{nInterval}}{\sum_{k=1}^{nInterval} \sin^2\frac{2\pi k}{nInterval}}. \tag{3.14b}$$

The results of the magnitude, phase, real part and imaginary part of the hydrodynamic function at Re=1000 and h/b=0.1 are shown in Figure 3-3. From the results, one can see that all three methods gave almost the same results (relative differences are less than 0.5%), which confirms the assumption that the torque per unit length is sinusoidal with time is valid. The numerical results from COMSOL simulation for this case are valid. Both the mesh size and the time interval between data points are small enough and don't have to be further reduced. For each calculation case with specific combination of the Reynolds number and the aspect ratio, the mesh size and calculation parameters are adjusted in order to make sure the resultant values of the hydrodynamic function obtained by the three methods are very close, similarly to the case shown in Figure 3-3.

3.2.3 Results of the Numerical Simulations for Rectangular Microcantilevers

A Java program, whose source file is provided in APPENDIX A, is developed to generate COMSOL models and compute the normalized torque per unit length. A MATLAB program, whose source file is provided in APPENDIX B, is developed to extract the magnitude, phase, real part, and imaginary part of the hydrodynamic function. Numerical results for the magnitude, phase, real part, and imaginary part of the hydrodynamic function in terms of the Reynolds number and aspect ratio (*h*/*b*) are given in Table C-1, Table C-2, Table C-3, and Table C-4 in APPENDIX C, respectively. Numerical results for the real and imaginary parts of the hydrodynamic function in terms of the Reynolds number and aspect ratio (*h/b*) are shown in Figure 3-4. Results using the analytical hydrodynamic function for the ribbon case [88] are also shown on the same figure for comparison purpose. From Figure 3-4, it can be seen that, as the Reynolds number increases, both real and imaginary parts of the hydrodynamic function decrease rapidly. Furthermore, as the aspect ratio (*h/b*) decreases, both the real and imaginary parts

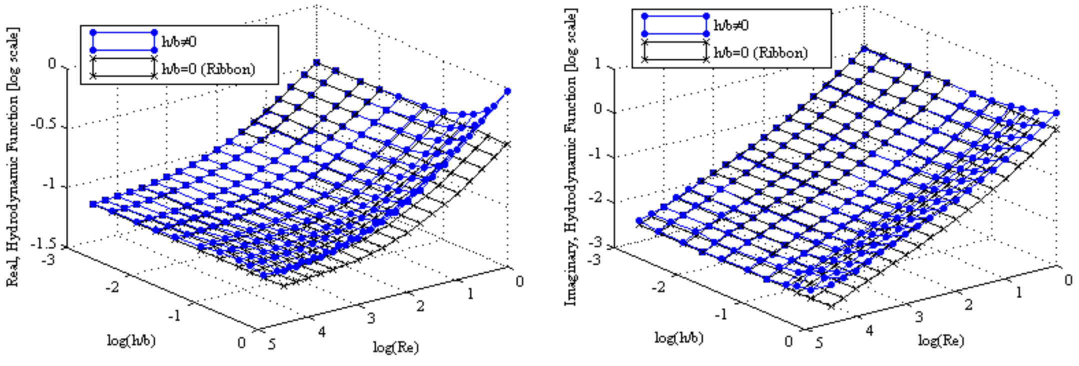

Figure 3-4: The hydrodynamic function in terms of the Reynolds number and aspect ratio: the real part (Left) & the imaginary part (Right).

of the hydrodynamic function decrease and the numerical results approach the empirical analytical expression for the ribbon case [88]. For the cases with very small aspect ratios, it is noted that the difference between the numerical results and the values calculated by Eqs. (3.7a-f) for the ribbon case is finite; the difference will not asymptotically approach zero with the reduction of the aspect ratio. This is due to the infinite flat plane assumption used for the ribbon case, which ignores the edge effect.

3.3 Analytical Expression of the Hydrodynamic Function for Rectangular Microcantilevers

When choosing the investigated Reynolds numbers and aspect ratios, it is assumed that the hydrodynamic function is proportional to the power function of the Reynolds number and approximately proportional to the aspect ratio. This assumption is extended from the approximation expressions proposed in the literature for the ribbon case [67,70, 93]. For example, the approximated expression proposed in Ref. 93, which is rewritten as Eq. (3.8), indicates that both the real part and imaginary part of the hydrodynamic function dependent on $\mathrm{Re}^{-0.5}$, which is a power function with the index of -0.5.

In general, the analytical expression of the hydrodynamic function can be written in the following form,

$$\Gamma_{\mathrm{rect,tors}}\left(\mathrm{Re},\frac{h}{b}\right)=\Gamma_{\mathrm{R1}}(\mathrm{Re})\Gamma_{\mathrm{R2}}\left(\frac{h}{b}\right)+j\,\Gamma_{\mathrm{I1}}(\mathrm{Re})\Gamma_{\mathrm{I2}}\left(\frac{h}{b}\right). \tag{3.15}$$

Assuming

$$\Gamma_{\mathrm{rect,tors,real}}=\Gamma_{\mathrm{R1}}(\mathrm{Re})\Gamma_{\mathrm{R2}}\left(\frac{h}{b}\right)=\left(a_{\mathrm{R1}}+a_{\mathrm{R2}}\,\mathrm{Re}^{m}\right)\left[a_{\mathrm{R3}}+(h/b)^{n}\right], \tag{3.16a}$$

$$\Gamma_{\text{rect,tors,imag}} = \Gamma_{\text{I1}}(\text{Re})\Gamma_{\text{I2}}\left(\frac{h}{b}\right) = \left(a_{\text{I1}}\,\text{Re}^{-1} + a_{\text{I2}}\,\text{Re}^{-0.5}\right)\left[a_{\text{I3}} + (h/b)^{p}\right], \tag{3.16b}$$

by fitting the numerical results on the values of real and imaginary parts of the hydrodynamic function, an analytical expression of the hydrodynamic function in terms of the Reynolds number, Re, and aspect ratio, *h/b*, is obtained using the MATLAB surface fitting tool, the function *sftool*, and is given by [92]

$$\Gamma_{\text{rect,tors,real}} = (0.05 + 0.24\text{Re}^{-0.43})[1.2 + (h/b)^{0.89}], \tag{3.17a}$$

$$\Gamma_{\text{rect,tors,imag}} = (\text{Re}^{-1} + 0.45\,\text{Re}^{-0.5})[0.75 + (h/b)]. \tag{3.17b}$$

Using this analytical expression, the values of hydrodynamic function for any arbitrary aspect ratio and Reynolds number within the parameter ranges investigated could be rapidly obtained. For the investigated aspect ratios (from 0.01 to 0.2) and Reynolds numbers (from 1 to 31,620), the real part of the hydrodynamic function is within 6.2% of the numerical results, and the imaginary part of the hydrodynamic function is within 22% of the numerical results. It is noted that the largest discrepancy for the imaginary part occurs when the Reynolds number is high and the aspect ratio is either very small or very large. When Re<10,000 and $0.02 \leqslant h/b \leqslant 0.1$, the largest discrepancy between the imaginary parts of the expression and the numerical results decreases to 8%. A more complicated model could be used for fitting the imaginary part of the hydrodynamic function over a wide range of Re and *h*/*b*. For high Reynolds numbers, although the relative discrepancy is high, the absolute difference is small since the values of the imaginary part of the hydrodynamic function are very small. For very high Reynolds number, the hydrodynamic function in viscous liquid could be approximated as that in inviscid liquid and the imaginary part is approximated as zero.

In order to improve the analytical expression of the hydrodynamic function, the following forms

$$\Gamma_{\text{rect,tors,real}} = \left(c_{\text{R1}}\,\text{Re}^{-0.5} + c_{\text{R2}}\,\text{Re}^{-0.25} + c_{\text{R3}}\right)\left[1 + c_{\text{R4}}(h/b) + c_{\text{R5}}(h/b)^2\right], \qquad (3.18\text{a})$$

$$\Gamma_{\text{rect,tors,imag}} = \left(c_{\text{I1}}\,\text{Re}^{-1} + c_{\text{I2}}\,\text{Re}^{-0.75} + c_{\text{I3}}\,\text{Re}^{-0.5} + c_{\text{I4}}\right)\left[1 + c_{\text{I5}}(h/b) + c_{\text{I6}}(h/b)^2\right], \quad (3.18\text{b})$$

are assumed to obtain the surface fitting and a new analytical expression is given by

$$\Gamma_{\text{rect,tors,real}} = (0.21\text{Re}^{-0.5} + 0.075\text{Re}^{-0.25} + 0.057)[1 + 1.1(h/b) - 0.82(h/b)^2], \quad (3.19\text{a})$$

$$\Gamma_{\text{rect,tors,imag}} = (1.1\text{Re}^{-1} - 0.29\,\text{Re}^{-0.75} + 0.39\,\text{Re}^{-0.5} + 0.00018)[1 + 1.24(h/b)]. \quad (3.19\text{b})$$

For the ribbon case in inviscid liquids, the analytical expression of the hydrodynamic function, described by Eqs. (3.19a-b), reduces to 0.057 + 0.00018 j, which is close to 0.0625 given in Eq. (2.46) obtained by Chu [51]. The relative difference of these two real parts is 9.6%. In order to obtain better accuracy of the hydrodynamic function for viscous liquids, the constant terms 0.057 and 0.00018 are kept in the analytical expression rather than replaced by 0.0625 and 0, respectively.

By using this analytical expression of the hydrodynamic function described by Eq. (3.19a-b), the real part is within 5.9% of the numerical results, and the imaginary part is within 11.2% of the numerical results for the investigated aspect ratios (from 0.01 to 0.2) and Reynolds numbers (from 1 to 31,620). The discrepancy on the imaginary part of the hydrodynamic function does not much affect the accuracy of the prediction on the resonance frequency. On the other hand, it does affect the accuracy of the prediction on the quality factor because the quality factor is inversely proportional to the imaginary part of the hydrodynamic function. For the cases with very high Reynolds numbers such as

17,780, the analytical expression Eq. (3.19b) rather than Eq. (3.17b) should be used to evaluate the imaginary part of the hydrodynamic function.

The alternative method is to directly use the numerical values of the hydrodynamic function at the investigated Reynolds numbers and aspect ratios when calculating the quality factor. In Section 5.3, it will be shown in details how to design the microcantilever dimensions and calculate the characteristics (resonance frequency, quality factor, mass sensitivity, normalized mass limit of detection) by using the numerical results of the hydrodynamic function at the investigated Reynolds numbers and aspect ratios rather than the analytical expression of the hydrodynamic function. This approximation can only be used for the investigated Reynolds numbers and aspect ratios. It requires maintaining a table for the values of the hydrodynamic function, which is tedious. As a result, it is only used to design microcantilevers working with high Reynolds numbers.

4. CHARACTERISTICS OF TORSIONALLY VIBRATING RECTANGULAR MICROCANTILEVERS IN VISCOUS LIQUIDS

4.1 Introduction

Based on the analytical expression of the hydrodynamic function obtained in the previous chapter, the characteristics (frequency spectrum, resonance frequency and quality factor) of torsionally vibrating microcantilevers in viscous liquid media are theoretically evaluated in this chapter. The characteristics relevant to chemical sensor applications will be evaluated in the next chapter. A MATLAB program, whose source file is provided in APPENDIX D, was developed to calculate the characteristics and the design dimensions of rectangular microcantilevers.

In this chapter, the resonance frequencies and quality factors of torsionally vibrating microcantilevers in viscous liquids are evaluated and their dependences on the geometry of the microcantilever and the properties of the liquid are investigated. Then the evaluated characteristics of a torsionally vibrating microcantilever in water are compared to those of the same microcantilever operating in transverse and lateral modes, and to experimental data obtained from the Center for MEMS and Microsystems Technologies, Georgia Institute of Technology in collaboration with the Microsensor Research Lab at Marquette University [125].

In order to calculate the characteristics of a vibrating microcantilever in viscous liquids, the material properties such as Young's modulus and shear modulus should be determined. Silicon is the most common single material used in MEMS devices and it is an anisotropic crystalline material whose material properties depend on orientation relative to the crystal lattice [124]. In the frame of reference of a standard (100) wafer,

Table 4-1: Ratios of density (ρ_{ag}) and viscosity (η_{ag}) between aqueous glycerol solutions and water [117]

Percent (w/w)	0.5	1	2	3	4	5	6	7	8
ρ_{ag}/ρ_{water}	0.9994	1.0005	1.0028	1.0051	1.0074	1.0097	1.012	1.0144	1.0167
η_{ag}/η_{water}	1.009	1.02	1.046	1.072	1.098	1.125	1.155	1.186	1.218
Percent (w/w)	9	10	12	14	16	18	20	24	28
ρ_{ag}/ρ_{water}	1.0191	1.0215	1.0262	1.0311	1.036	1.0409	1.0459	1.0561	1.0664
η_{ag}/η_{water}	1.253	1.288	1.362	1.442	1.53	1.627	1.734	1.984	2.274
Percent (w/w)	32	36	40	44	48	52	56	60	64
ρ_{ag}/ρ_{water}	1.077	1.0876	1.0984	1.1092	1.12	1.1308	1.1419	1.153	1.1643
η_{ag}/η_{water}	2.632	3.082	3.646	4.434	5.402	6.653	8.332	10.66	13.63
Percent (w/w)	68	72	76	80	84	88	92	96	100
ρ_{ag}/ρ_{water}	1.1755	1.1866	1.1976	1.2085	1.2192	1.2299	1.2404	1.2508	1.2611
η_{ag}/η_{water}	18.42	27.57	40.49	59.78	84.17	147.2	383.7	778.9	1759.6

whose x, y , z axes are in the drections $[110]$, $[\bar{1}10]$, $[001]$, respectively, the Young's modulus (Ex) is 169 GPa and the shear modulus (Gyz) is 79.6 GPa [124].

For the calculations in this dissertation, if there is no further description, the following material properties are used. The Young's modulus, shear modulus and density of the silicon microcantilever are 169 GPa, 79.6 GPa, 2330 kg/m^3, respectively; the density and viscosity of air are 1.205 kg/m^3, 0.01827 cP, respectively; the density and viscosity of water are 1000 kg/m^3, 1 cP, respectively. Besides water, aqueous glycerol solutions are also simulated as the operating liquid media in this dissertation. The ratios of density and viscosity between the solutions and water are given in Table 4-1 for aqueous glycerol solutions [117].

In addition, if there is no further description, the investigated microcantilevers are 80 rectangular silicon microcantilevers with lengths of 200, 400, 600, 800, 1000 μm, widths of 45, 60, 75, 90 μm and thicknesses of 12, 6, 3, 1.5 μm. These geometries are similar to the geometries used to investigate the characteristics of laterally vibrating microcantilevers in viscous liquids in Ref 82, and are selected here for comparison purpose.

4.2 Resonance Frequency

4.2.1 Trends in the Resonant Frequency as a Function of Microcantilever Geometry

The resonance frequency of a torsionally vibrating microcantilever in vacuum calculated using Eq. (2.18a) is found to be dependent on $h/(bL)$. The simulated resonance frequencies of the investigated microcantilevers operating in the 1st torsional mode in water are shown in Figure 4-1 with respect to the parameter $h/(bL)$. Two theories are used to evaluate the resonance frequencies: one is the ribbon theory [88] which ignores the thickness effects; the other one is the theory proposed in Chapter 2 which considers all three thickness effects.

From Figure 4-1, it is seen that the 1st torsional resonance frequency is dependent on the parameter $h/(bL)$ for all investigated microcantilever geometries. On the other hand, the 1st lateral resonance frequency is dependent on b/L^2 [82-84]. Such different trends can be used to optimize device geometry in chemical sensing applications. It is

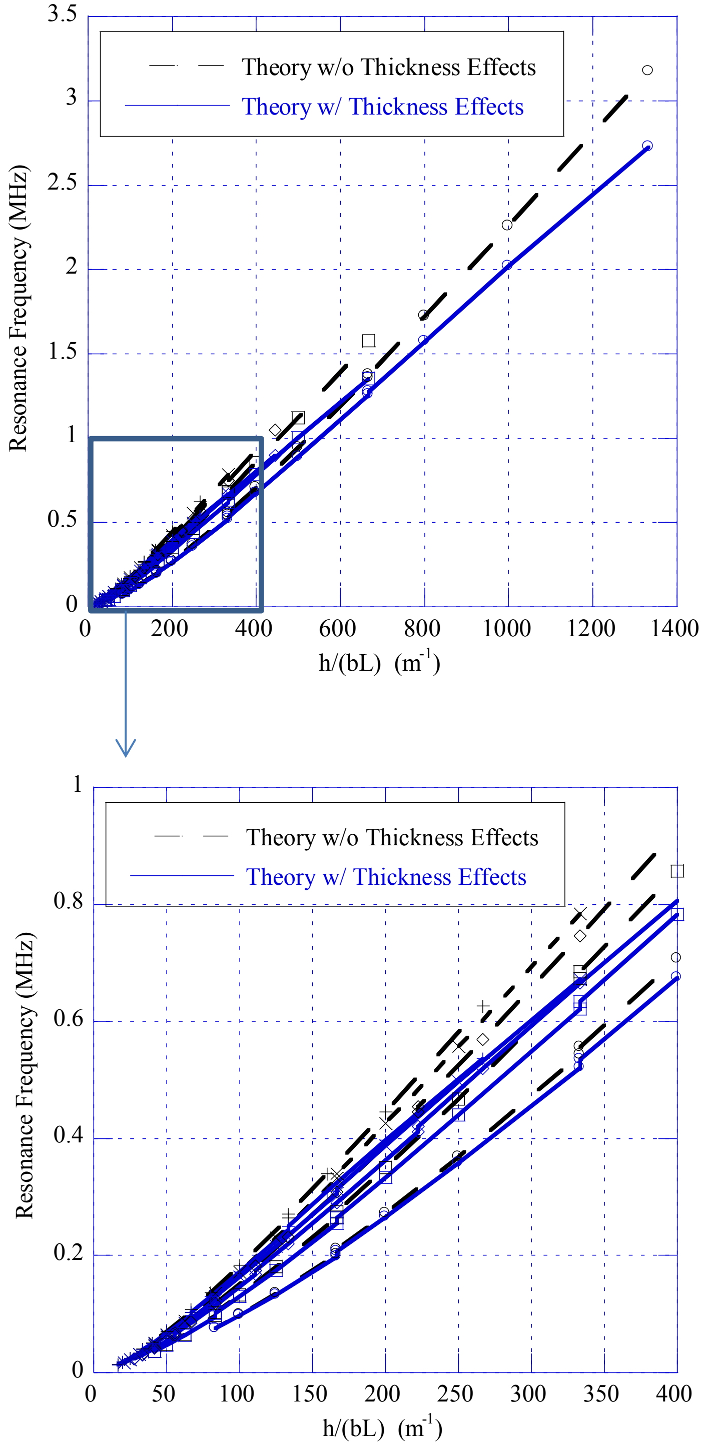

Figure 4-1: Simulated resonance frequencies of silicon microcantilevers vibrating in the first torsional mode in water as a function of $h/(bL)$ for widths of 45, 60, 75, and 90 μm, lengths of 200 μm (o), 400 μm (□), 600 μm (◊), 800 μm (×), 1000 μm (+), and thicknesses of 12, 6, 3, 1.5 μm.

also seen in Figure 4-1 that, as the aspect ratio (*h*/*b*) decreases, the resonance frequencies calculated by the theory in Chapter 2 approach those calculated by ribbon theory. In addition, the results indicate that the difference in the values of the 1st torsional resonance frequencies in water obtained by these two theories could be greater than 9% for microcantilevers with *h*/*b*>0.16. This means that the error in the resonance frequency for the 1st torsional mode could be also greater than 9% for microcantilevers with *h*/*b*>0.16 operating in water if the thickness effects are ignored.

4.2.2 Effects of the Liquid Medium's Viscosity on the Resonant Frequency

The resonance frequencies of two specific microcantilever geometries (200x60x6.7 μm^3 and 1000x90x10.9 μm^3) in aqueous glycerol solutions are investigated. The resonance frequencies calculated using the inviscid liquid theory [51-52], the ribbon theory [88] and the theory proposed in Chapter 2 are shown and compared in Figure 4-2 for aqueous glycerol solutions.

When the concentration of the aqueous glycerol solution is below 60%, from Figure 4-2, it is seen that the resonance frequency decreases approximately linearly as the concentration, hence the viscosity of the aqueous glycerol solution increases.The difference between the calculated values of the resonance frequency obtained by the ribbon theory [88] and the theory proposed in Chapter 2 is nearly constant. For example, this difference is around 80 kHz and the relative errors are greater than 8% for the 200x60x6.7 μm^3 microcantilever. This indicates that the error of the ribbon theory could be greater than 8% when evaluating the 1st torsional resonance frequency of the microcantilever whose aspect ratio is greater than 0.11 in aqueous glycerol solutions with

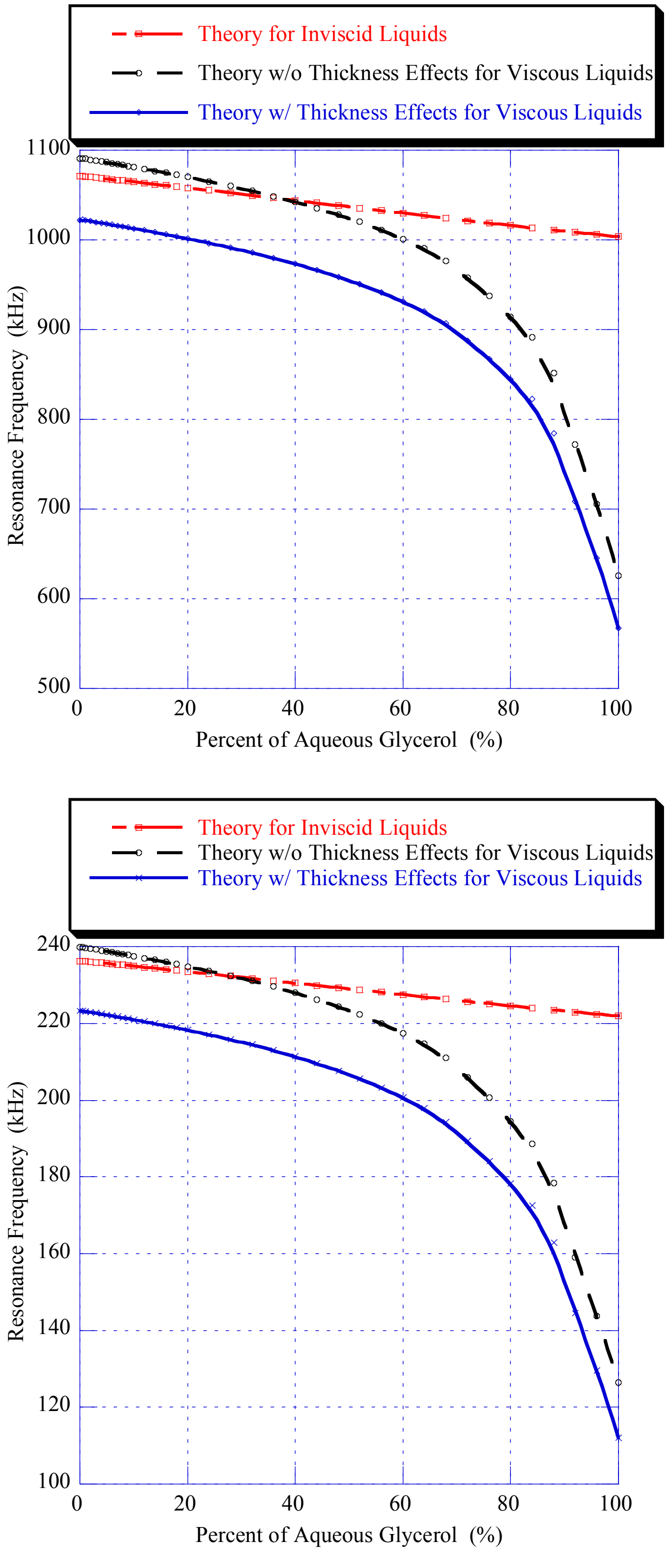

Figure 4-2: Resonance frequencies of the microcantilevers 200x60x6.7 µm^3 (top) & 1000x90x10.9 µm^3 (bottom) in aqueous glycerol solutions.

the glycerol concentration below 80%.

4.3 Quality Factor

4.3.1 Trends in the Quality Factor as a Function of Microcantilever Geometry

The quality factors of torsionally vibrating microcantilevers obtained by ribbon theory [88] and the theory proposed in Chapter 2 are shown and compared in Figure 4-3 as a function of $hL^{-0.5}$. From Figure 4-3, it is seen that the quality factor in the 1st torsional mode is dependent on the parameter $hL^{-0.5}$ for all investigated microcantilever geometries. On the other hand, the quality factor in the 1st lateral mode frequency is dependent on $hb^{0.5}/L$ [82-84]. Such different trends can be used to optimize the frequency stability in chemical sensing applications. It is also seen in Figure 4-3 that, as the aspect ratio (h/b) decreases, the quality factors calculated by the theory in Chapter 2 approach those calculated by ribbon theory. The results also indicate that the difference in the values of the quality factors obtained by these two theories could be greater than 5% for microcantilevers with $h/b>0.16$. This means that the error in the calculated quality factor for the 1st torsional mode could be also greater than 5% for microcantilevers with $h/b>0.16$ operating in water if the thickness effects are ignored.

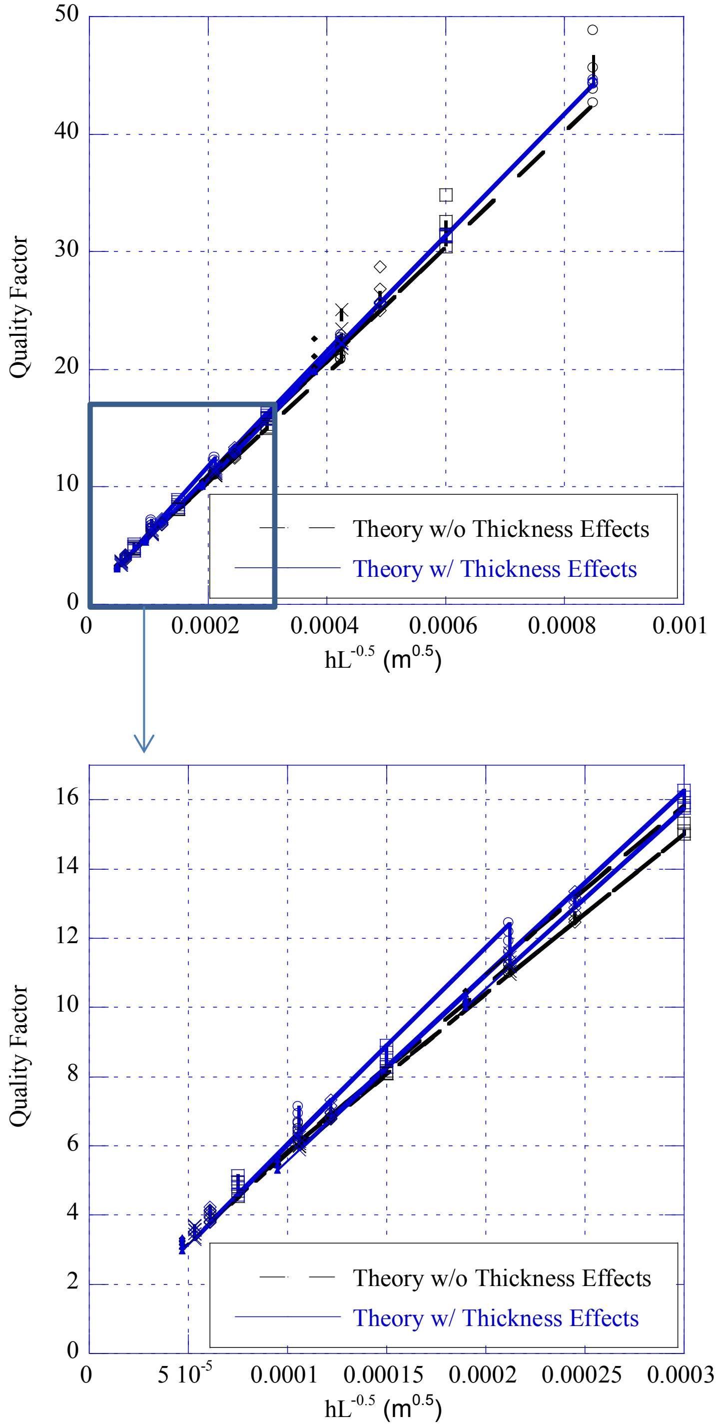

Figure 4-3: Simulated quality factors of silicon microcantilevers vibrating in the first torsional mode in water as a function of $hL^{-0.5}$ for widths of 45, 60, 75, and 90 µm, lengths of 200 µm (o), 400 µm (□), 600 µm (◊), 800 µm (×), 1000 µm (+), and thicknesses of 12, 6, 3, 1.5 µm.

4.3.2 Effects of the Liquid Medium's Viscosity on the Quality Factor

The quality factors of two specific microcantilever geometries (200x60x6.7 μm^3 and 1000x90x10.9 μm^3) in aqueous glycerol solutions are investigated. The quality factors calculated by the ribbon theory [88] and the theory proposed in Chapter 2 are shown and compared in Figure 4-4.

When the concentration of the aqueous glycerol solution is below 60%, from Figure 4-4, it is seen that the quality factor decreases approximately linearly as the concentration, hence the viscosity of the aqueous glycerol solution increases. When the concentration increases up to 60%, the difference between the calculated values of the quality factor obtained by ribbon theory [88] and the theory proposed in Chapter 2 decreases. The relative errors are greater than 7%. As expected, the error could be greater than 7% for evaluating the quality factor of the microcantilever operating in the 1st torsional mode in aqueous glycerol solutions with the glycerol concentration below 60% when the aspect ratio is greater than 0.11.

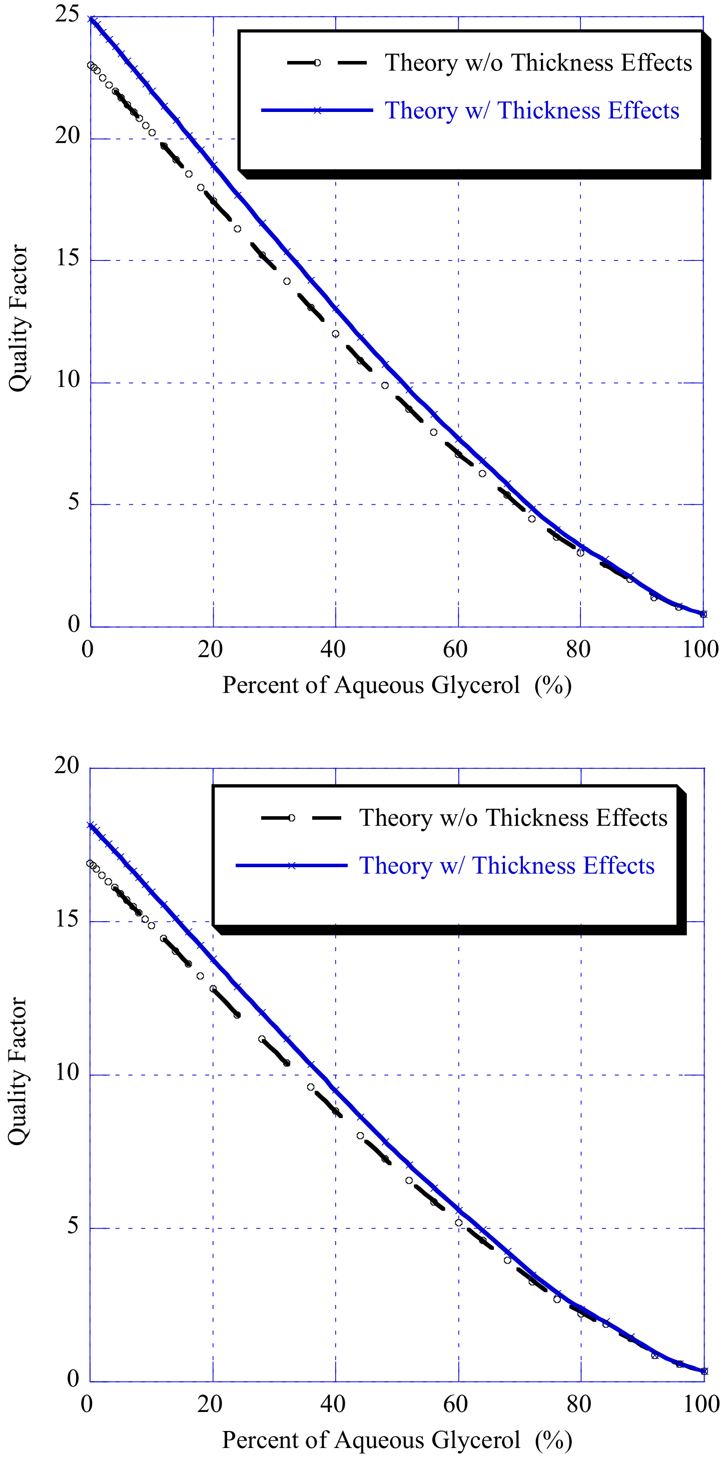

Figure 4-4: Quality Factors of the microcantilevers 200x60x6.7 µm^3 (top) & 1000x90x10.9 µm^3 (bottom) in aqueous glycerol solutions.

4.4 Comparison on Torsional, Lateral, and Transverse Modes

The resonance frequencies in air and water, the quality factors in water for four microcantilever geometries under torsional, lateral, and transverse modes are shown and compared in Table 4-2.

The 1st resonance frequency of a microcantilever operating torsionally, laterally, or transversely in water is found to shift to a lower value compared to that in air, as expected. However, the predicted resonance frequency shifts are found to be different for these three vibration modes. For instance, the 1st lateral resonance frequencies only drop by a value of up to 10% while the 1st torsional and 1st transverse resonance frequencies

Table 4-2: Comparison on resonance frequencies and quality factors for four microcantilevers under 1st torsional, 1st lateral, and 1st transverse modes

Geometry	$Lxbxh$ [µm^3]	400x45x12	200x45x6	200x45x12	200x90x12
Torsional Mode	f_{air} [MHz]	1.717	1.847	3.433	1.847
	f_{water} [MHz]	1.355	1.257	2.726	1.276
	Percent Change [%]	-21.1	-31.9	-20.6	-30.9
	Q_{water}	31.5	22.24	44.5	44.3
Lateral Mode [80]	f_{air} [MHz]	0.386	1.547	1.547	3.095
	f_{water} [MHz]	0.347	1.443	1.411	2.934
	Percent Change [%]	-10.1	-6.72	-8.79	-5.20
	Q_{water}	17.1	21.2	34.3	60.0
Transverse Mode [80]	f_{air} [MHz]	0.103	0.206	0.412	0.412
	f_{water} [MHz]	0.064	0.102	0.264	0.214
	Percent Change [%]	-37.8	-50.4	-35.9	-48.0
	Q_{water}	9.30	9.1	17.3	22.7

drop by as much as 32% and 50%, respectively. It is also shown in Table 4-2 that the 1st resonance frequency of torsionally or laterally vibrating microcantilevers in water is much higher than that of transversely vibrating microcantilevers with the same geometries. For liquid-phase chemical sensor applications, it is more advantageous to operate in the 1st torsional or 1st lateral mode because the sensitivity of a microcantilever as a chemical sensor is proportional to its resonance frequency.

Furthermore, for the same geometry, the quality factor of microcantilevers vibrating in the 1st torsional or 1st lateral mode is much higher than that of microcantilevers vibrating in the 1st transverse mode. It is also seen that the quality factor increases as the length of the microcantilever decreases or as the thickness of the microcantilever increases for all three modes. However, as the width of the microcantilever increases, the quality factors are found to remains almost constant for the torsional mode, whereas it increases for the lateral or transverse mode.

4.5 Characteristics Comparison for a Specific Microcantilever with Effective Material Properties

Before evaluating the characteristics of a microcantilever fabricated by hybrid layers with different materials, its effective material properties such as the Young's modulus and shear modulus have to be determined. The resonance frequencies of the torsional, lateral and transverse modes of a microcantilever in vacuum are well known [110,116] and are given as follows, respectively,

$$f_{\text{tors,vac,1}} = \frac{1}{4L}\sqrt{\frac{GK}{\rho J_p}}, \tag{4.1a}$$

$$f_{\text{lat,vac,1}} = \frac{1.875^2 b}{2\pi L^2}\sqrt{\frac{E}{12\rho}}, \tag{4.1b}$$

$$f_{\text{tran,vac,1}} = \frac{1.8751^2 h}{2\pi L^2}\sqrt{\frac{E}{12\rho}}, \tag{4.1c}$$

$$f_{\text{tran,vac,2}} = \frac{4.6941^2 h}{2\pi L^2}\sqrt{\frac{E}{12\rho}}, \tag{4.1d}$$

where L, b, h, G, K, ρ, J_p , E are length, width, thickness, shear modulus, torsional constant, mass density, polar moment of the cross-section area, Young's modulus of the microcantilever, respectively. The number in the subscript is the mode number. Since the resonance frequencies in vacuum are close to those in air, the effective material properties are approximated as

$$G_{\text{eq}} \approx \frac{16L^2 \rho J_p f^2_{\text{tors,air,1}}}{K}, \tag{4.2a}$$

$$E_{\text{eq}} = \frac{1}{3}\left(E_{\text{lat}} + E_{\text{tran,1}} + E_{\text{tran,2}}\right), \tag{4.2b}$$

$$E_{\text{lat}} \approx \frac{48\pi^2 L^4 \rho f^2_{\text{lat,air,1}}}{1.875^4 b^2}, \tag{4.2c}$$

$$E_{\text{tran,1}} \approx \frac{48\pi^2 L^4 \rho f^2_{\text{lat,air,1}}}{1.875^4 b^2}, \tag{4.2d}$$

$$E_{\text{tran}} \approx \frac{48\pi^2 L^4 \rho f^2_{\text{tran,air,2}}}{4.6941^4 h^2}. \tag{4.2e}$$

By using the experimental results [125] of the resonance frequencies in air, the effective material properties are calculated as G_{eq}=45.4 GPa and E_{eq}=110 GPa. They represent the values of the shear modulus and Young's modulus of the microcantilever used in the simulations in this section.

Table 4-3: Comparison of resonance frequencies and quality factors of a 400x90x22.3 μm^3 microcantilever

	1st Torsional Mode				1st Lateral Mode			
	f_{air} [kHz]	f_{water} [kHz]	Percent Change	Q_{water}	f_{air} [kHz]	f_{water} [kHz]	Percent Change	Q_{water}
Theory with Thickness Effects	1218.63	957.54	-21.42%	50.6	624.24	573	-8.21%	41.7
Ribbon Theory	1366.66	1100.3	-19.49%	53.4	624.32	620	-0.69%	73.4
Percent Change Between Ribbon Theory and Theory with Thickness Effect	12.1%	14.9%	1.93%	5.5%	0.013%	8.20%	7.52%	76%
Available Experimental Data [125]	1218.79	950.88	-21.98%	44	636.68	596	-6.39%	N/A
Percent Change Between Theory with Thickness Effects and the Experiment	-0.013%	0.7%	2.5%	15%	-1.95%	-3.86%	-28.5%	N/A
Percent Change Between Ribbon Theory and the Experiment	12.1%	15.7%	11.3%	21%	-1.94%	4.03%	89.2%	N/A

	1st Transverse Mode				2nd Transverse Mode			
	f_{air} [kHz]	f_{water} [kHz]	Percent Change	Q_{water}	f_{air} [kHz]	f_{water} [kHz]	Percent Change	Q_{water}
Ribbon Theory	154.53	97.639	-36.82%	19.96	968.58	622.58	-35.72%	43.8
Available Experimental Data [125]	154.6	96.074	-37.86%	20	954.57	615.01	-35.57%	42
Percent Change Between Ribbon Theory and the Experiment	-0.045%	1.63%	2.75%	-0.2%	1.47%	1.23%	-0.42%	4.3%

The resonance frequencies and quality factors of a 400x90x22.3 μm^3 (the length, width, thickness are 400, 90, 22.3 μm, respectively) microcantilever operating in the 1st torsional, 1st lateral, 1st transverse, and 2nd transverse modes are obtained by both theoretical simulations and experimental measurements and are compared in Table 4-3.

This microcantilever geometry is used because of the available set of experimental data. In this table, the experimental data are obtained in the Center for MEMS and Microsystems Technologies at Georgia Institute of Technology in collaboration with the Microsensor Research Lab at Marquette University [125]. The ribbon theories for torsional, lateral, and transverse modes were proposed in Ref 88, 75, 62, respectively. The theory with thickness effects for torsional mode are presented in Chapter 2, which considers thickness effects on torsional constant, hydrodynamic function, polar moment of cross-section area. The theory with thickness effects for lateral mode was proposed in Ref 82 and 84.

The simulated frequency spectra of this microcantilever vibrating torsionally, laterally, and transversely in air or water are shown in Figure 4-5. From Table 4-3 and Figure 4-5, it is seen that the resonance frequency of this microcantilever in air or water under 1st torsional or 1st lateral vibration mode is much higher than that under 1st transverse mode due to the higher stiffness in torsional or lateral mode. The quality factor of this microcantilever in air or water under 1st torsional or 1st lateral vibration mode is higher than that under 1st transverse mode. Experimental data [125] also show that the percent drop from air to water of the resonance frequency of this microcantilever for the 1st torsional, 1st lateral, 1st transverse, and 2nd transverse modes are 21.98%, 6.39%, 37.86%, 35.57%, respectively. These indicate that both 1st torsional and 1st lateral modes have better performance than the two transverse modes, and the 2nd transverse mode has better performance than the 1st transverse mode for this microcantilever, as expected.

Furthermore, from Table 4-3, the discrepancies between calculated values by the ribbon theory and the theory proposed in Chapter 2 are large for this microcantilever operating in the 1st torsional mode or 1st lateral mode in water. For example, the discrepancies between the calculated values of resonance frequencies and quality factors

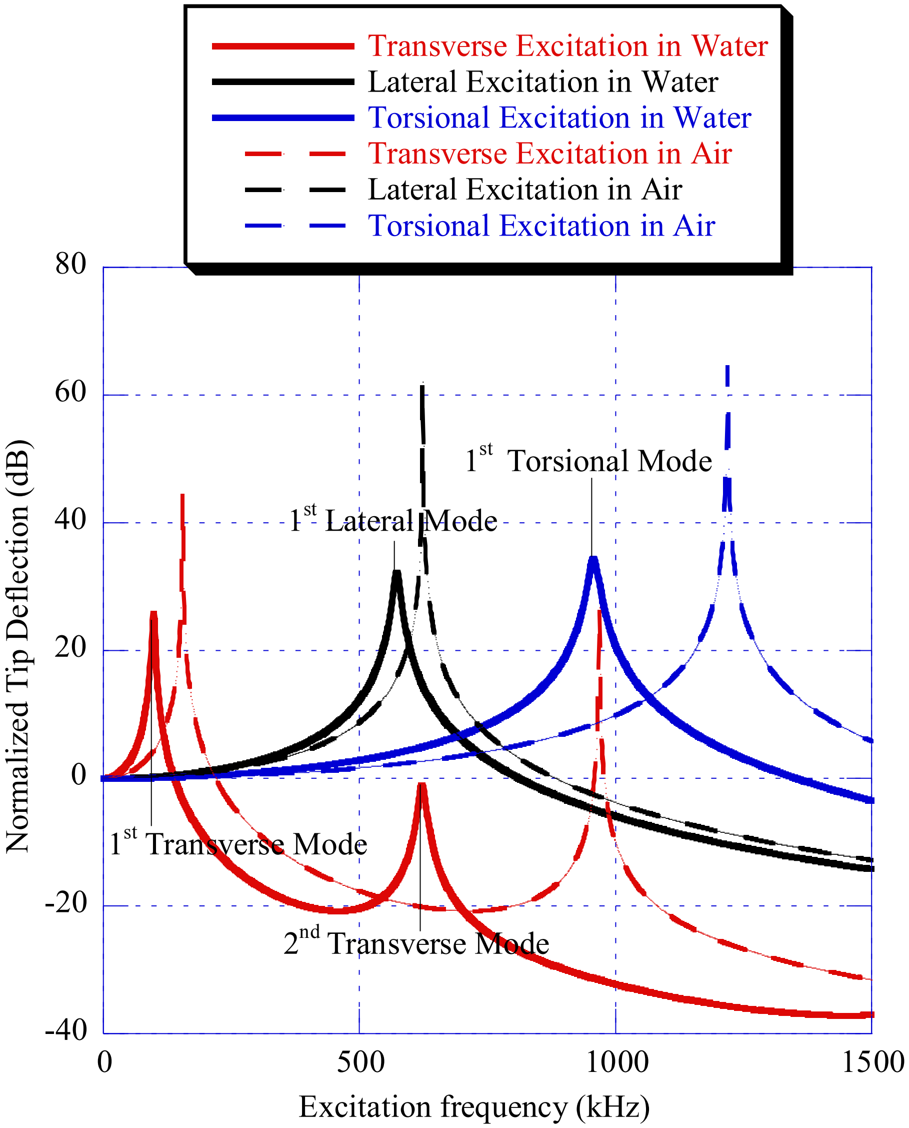

Figure 4-5: Simulated frequency spectra of a 400x90x22.3 µm^3 silicon microcantilever (*G*=45.4 GPa, *E*=110 GPa) vibrating torsionally, laterally, transversely in air or water.

in water for 1st torsional mode and 1st lateral mode are 14.9%, 8.2%, respectively. The discrepancies between calculated values by the theory proposed in Chapter 2 and experimental data are small for this microcantilever operating in the 1st torsional mode or 1st lateral mode in water. For example, the discrepancies between the calculated values of the resonance frequencies in water for 1st lateral and 1st torsional mode are 0.7%, -3.86%, respectively. These indicate that the theory proposed in Chapter 2 of this dissertation for torsional mode and the theory proposed in Ref 82 and 84 for lateral mode have improved the prediction of the resonance frequencies and quality factors in water, whereas the ribbon theory overestimates the resonance frequency in water. Ignoring thickness effects could result in high error for the microcantilever with such high aspect ratio (h/b) as 0.225 for both torsional and lateral modes, especially for the torsional mode. In contrast, the discrepancies between the calculated values by the ribbon theory and the experimental data are small for the two transverse modes in water, especially for the 1st transverse mode. It confirms that the thickness effect on transverse mode could be ignored in viscous liquids such as water, even for such high aspect ratio (h/b) as 0.224 for this microcantilever.

Thickness effects on the torsional constant, hydrodynamic function, and polar moment of cross-section area of this microcantilever under 1st torsional mode in water are compared in Table 4-4. In this table, the changes of the resonance frequency in the third column and the quality factor in the sixth column are the differences of the relevant calculated values between the other cases and the case considering all the thickness effects. The percentages in the fourth and senventh columns are weights of the charateristics change induced by one specific thickness effect. For example, the change of

Table 4-4: Comparison of the thickness effects on torsional constant (*K*), Hydrodynamic function ($\Gamma_{rect,tors}$), and polar moment of cross-section area (J_p) of a 400x90x22.3 µm^3 microcantilever under the 1st torsional mode in water

	f_{water} [kHz]	df_{water} [kHz]	Percent [%]	Q_{water}	dQ_{water}	Percent [%]
Consider all three thickness effects	957.542	N/A	N/A	50.6	N/A	N/A
Ignore thickness effect on *K*	1042.85	85.308	59.7	52.8	2.2	78.6
Ignore thickness effect on $\Gamma_{rect,tors}$	990.80	33.258	23.3	52.6	2.0	71.4
Ignore thickness effect on J_p	975.21	17.668	12.4	49.2	-1.4	-50
Sum of the 3 rows above	N/A	136.234	95.4	N/A	2.8	100
Ribbon Theory (ignore all three thickness effects)	1100.32	142.778	100	53.4	2.8	100

the resonance frequency in water between the case only considering the thickness effect of the torsional constant and the case considering all three thickness effects is 85.308 kHz. The change of the resonance frequency is 142.778 kHz between the ribbon case and the case considering all three thickness effects. The ratio between these two changes of resonance frequency is the weight of the thickness effect of torsional constant on the resonance frequency and is given by 59.7%.

From Table 4-4, it is seen that for this 400x90x22.3 µm^3 microcantilever under 1st torsional mode in water, ignoring the thickness effect on the torsional constant or the hydrodynamic function increases the calculated values of both the resonance frequency and the quality factor. Ignoring the thickness effect on the polar moment of the cross-section area increases the calculated values of the resonance frequency, but decreases the calculated values of the quality factor. The thickness effect on the torsional constant is dominant when evaluating the resonance frequency since the weights of the thickness effects of the torsional constant, hydrodynamic function, polar moment of cross-section area for calculated values of resonance frequencies are 59.7%, 23.3%, 12.4%, respectively. The thickness effects on both the torsional constant and hydrodynamic function are dominant when evaluating the quality factor since the weights of the thickness effects of the torsional constant, hydrodynamic function, polar moment of cross-section area are 78.6%, 71.4%, -50%, respectively. It also indicates that the thickness effects could be approximated as the superposition of each effect when evaluating the resonance frequency and quality factor for this microcantilever.

5. TORSIONALLY VIBRATING MICROCANTILEVERS AS CHEMICAL SENSORS IN VISCOUS LIQUIDS

5.1 Sensitivity

5.1.1 Definitions and Derivation

The sensitivity is the ratio of the magnitude of the output signal to the magnitude of the input quantity to be measured. For a dynamic mode MEMS-based sensor, the mass sensitivity is the ratio of the magnitude of the resonance frequency shift to the magnitude of the mass change and is given as

$$S_{M,i} = \left| \frac{\Delta f_{r,i}}{\Delta M} \right| . \tag{5.1}$$

$f_{r,i}$ is the resonance frequency associated with the i-th vibration mode. The resonance frequency and mass are associated with both the microcantilever and the film (sensing layer). It is assumed that the mass inertia and rotational inertia of the film are negligible compared to those of the microcantilever. Based on Eq. (2.18a), Eq. (2.19) and Eq. (2.42), the i-th torsional resonance frequency is rewritten as

$$f_{r,i} = f_{\mathrm{VisL},i} = \frac{2i-1}{4L}\sqrt{\frac{GK(1-2\xi_i^2)}{\rho J_p + g_{2,\mathrm{tors}}}} . \tag{5.2}$$

The resonance frequency shift is obtained using the chain rule and is given as

$$\frac{\Delta f_{r,i}}{f_{r,i}} \approx -\frac{\Delta(\rho J_p)}{2(\rho J_p + g_{2,\mathrm{tors}})} + \frac{\Delta(GK)}{2(GK)} - \frac{2\xi_i \Delta\xi_i}{1-2\xi_i^2} - \frac{\Delta g_{2,\mathrm{tors}}}{2(\rho J_p + g_{2,\mathrm{tors}})} . \tag{5.3}$$

The terms on the right side of Eq. (5.3) are associated with the resonance frequency shift due to the variation of the rotational inertia, stiffness, damping ratio and hydrodynamic inertial torque per unit length, respectively. The variations of the stiffness, damping ratio, and hydrodynamic inertial torque per unit length are generally negligible so that the resonance frequency shift is essentially due to the rotational inertia variation. Since the variations of mass and rotational inertia are only associated with the film, the sensing element, the sensitivity and frequency shift are rewritten as

$$S_{M,i} = \left|\frac{\Delta f_{r,i}}{\Delta M_f}\right|, \tag{5.4}$$

$$\Delta f_{r,i} \approx -\frac{f_{r,i}\,\Delta(\rho_f J_{p,f})}{2(\rho J_p + g_{2,\mathrm{tors}})}, \tag{5.5}$$

where M_f and $J_{p,f}$ are the mass and the polar moment of the cross-section area of the film, respectively. The film is assumed to be deposited on the top of the microcantilever surface and divided into two identical parts, as shown in Figure 5-1. Although such film may not be practical due to the difficulty to deposit, it is proposed as the general case because the second moment of area of the center part is negligible; as a result, replacing the center part with a reasonal gap would increase the sensitivity. The mass and the polar moment of the cross-section area of this film are given as

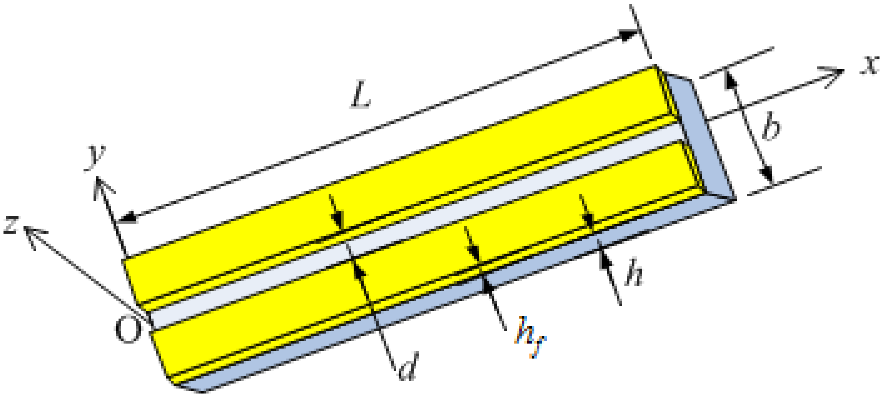

Figure 5-1: Geometry of the film (in yellow) and the microcantilever.

$$M_f = \rho_f (b-d) h_f L, \tag{5.6}$$

$$J_{p,f} = [bh_f(b^2 + h_f^2 + 3h^2) - dh_f(d^2 + h_f^2 + 3h^2)]/12, \tag{5.7}$$

where ρ_f, d, and h_f are the density, gap in width direction, and thickness of the film, respectively. It is assumed that the analyte sorption only changes the density of the film; it does not change the shape and size of the film. So the variations of mass and rotational inertia are obtained as

$$\Delta M_f = (b-d) h_f L \, \Delta\rho_f, \tag{5.8}$$

$$\Delta(\rho_f J_{p,f}) = J_{p,f} \, \Delta(\rho_f). \tag{5.9}$$

Substituting Eqs. (5.5)-(5.9) into Eq. (5.4), the sensitivity is rewritten as

$$S_{M,i}(d) = \frac{(b^2 + 3h^2 + h_f^2 + bd + d^2) f_{r,i}}{24L(\rho J_p + g_{2,\mathrm{tors}})}. \tag{5.10}$$

Eq. (5.10) indicates that the larger the thickness or the gap of the film, the higher the sensitivity. While improving the sensitivity by increasing the thickness of the film is also applicable for the microcantilevers operating in transverse, lateral or longitudinal mode, improving the sensitivity by increasing the gap is only applicable for the torsionally vibrating microcantilevers. Assuming the thickness of the film is much less than the thickness of the microcantilever and there is no gap in the film, the sensitivity expression is reduced to

$$S_{M,i} = \frac{(b^2 + 3h^2) f_{r,i}}{24L(\rho J_p + g_{2,\mathrm{tors}})}. \tag{5.11}$$

Eq. (5.11) is used to calculate the mass sensitivity in this dissertation. It always underestimates the mass sensitivity a little bit. The mass sensitivity could be improved by adding a gap in the film. For example, if the aspect ratio (h/b) is 0.1, adding a gap of half width (d/b=0.5) will improve the sensitivity by around 70%.

5.1.2 Trends in the Mass Sensitivity as a Function of Microcantilever Geometry

For the case of film without gap (d=0), the mass sensitivities of torsionally vibrating microcantilevers obtained from the ribbon theory [88] and the theory proposed in Chapter 2 are shown and compared in Figure 5-2 as a function of $h^{0.5}/(b^2L^{1.5})$. From Figure 5-2, it is seen that the mass sensitivity in torsional mode is approximately dependent on the parameter $h^{0.5}/(b^2L^{1.5})$ for all investigated microcantilever geometries. It is also shown in Figure 5-2 that, as the aspect ratio (h/b) decreases, the values of mass sensitivities calculated using the theory in Chapter 2 approach those calculated from the ribbon theory. The results also indicate that the difference in the values of mass sensitivities obtained from these two theories could be greater than 20% for microcantilevers with h/b>0.16. This also means that the error in the calculated mass sensitivity for the 1st torsional mode could be also greater than 20% for microcantilevers with h/b>0.16 in water if the thickness effects are ignored.

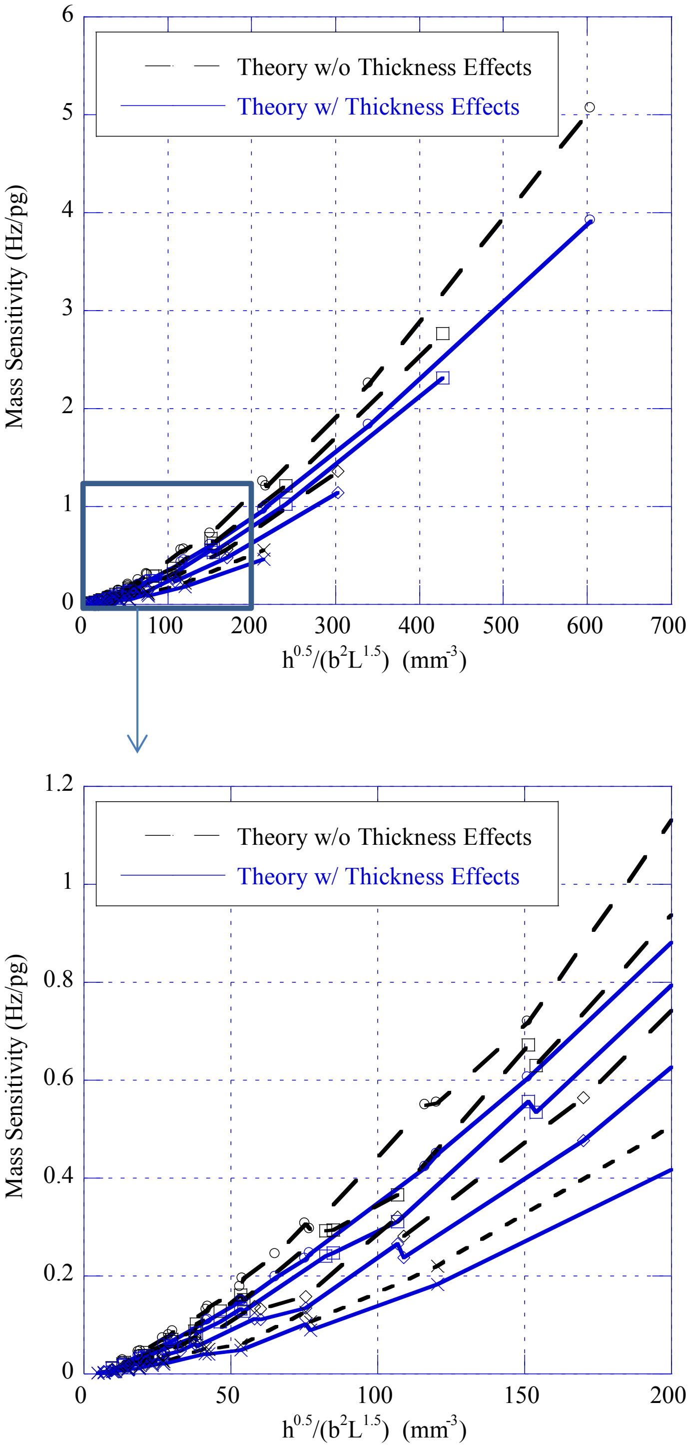

Figure 5-2: Simulated mass sensitivities of silicon microcantilevers vibrating in the first torsional mode in water as a function of $h^{0.5}/(b^2L^{1.5})$ for widths of 45, 60, 75, and 90 µm, lengths of 200, 400, 600, 800, 1000 µm, and thicknesses of 12 µm (o), 6 µm (□), 3 µm (◊), 1.5 µm (×).

5.1.3 Effects of the Liquid Medium's Viscosity on the Mass Sensitivity

For the case of film without gap (*d*=0), the mass sensitivities of two specific microcantilever geometries (200x60x6.7 μm^3 and 1000x90x10.9 μm^3) in aqueous glycerol solutions are investigated. The mass sensitivity calculated using the ribbon theory [88] and the theory proposed in Chapter 2 are shown and compared in Figure 5-3.

When the concentration of the aqueous glycerol solution is below 60%, from Figure 5-3, it is seen that the mass sensitivity decreases approximately linearly as the concentration, hence the viscosity of the aqueous glycerol solution increases. It is also shown that the difference between the calculated values of the mass sensitivities obtained from the ribbon theory [88] and the theory proposed in Chapter 2 is nearly constant and large. For example, this difference is around 0.15 Hz/pg and the relative errors are greater than 12% for the 200x60x6.7 μm^3 microcantilever. This indicates that the error could be greater than 12% when evaluating the mass sensitivity for microcantilevers whose aspect ratio is greater than 0.11 for the 1st torsional mode in aqueous glycerol solutions with any glycerol concentrations.

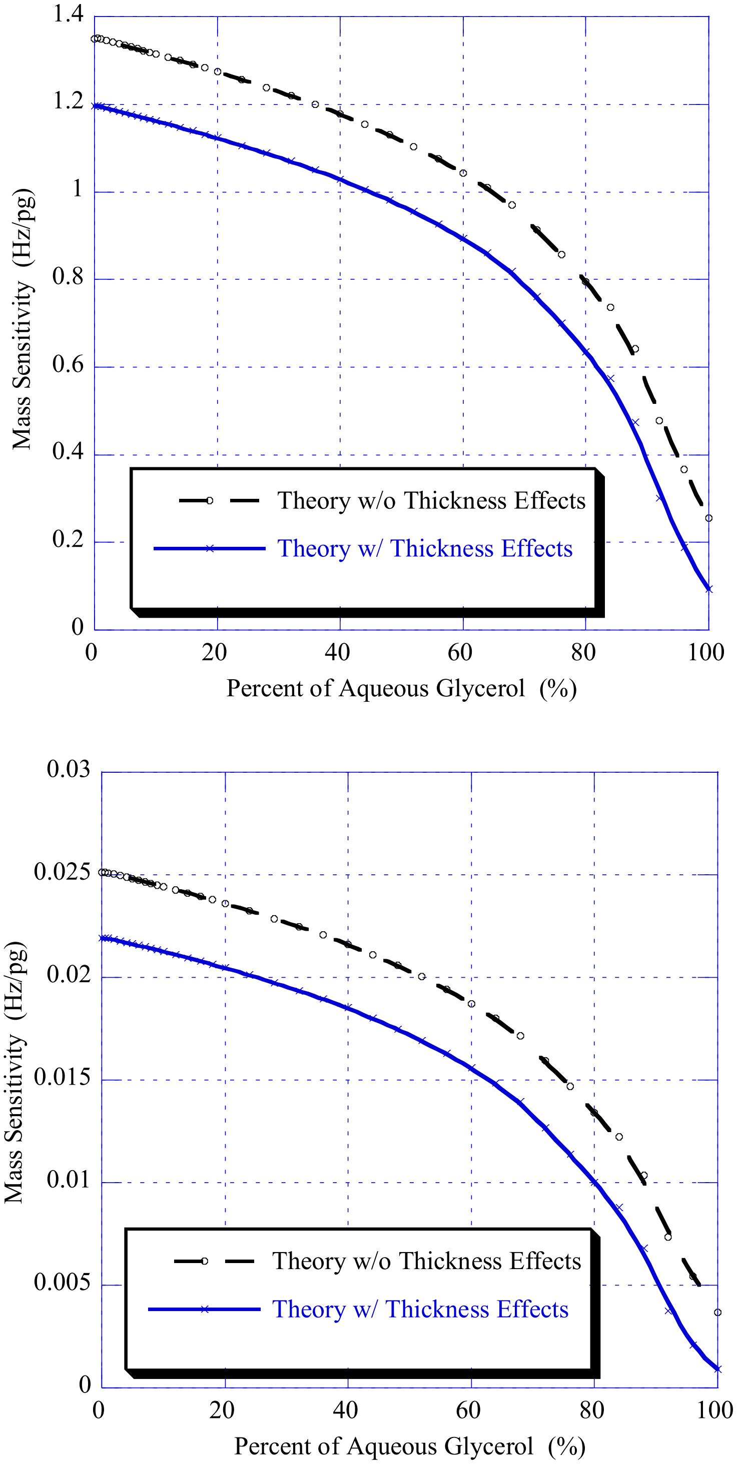

Figure 5-3: Mass sensitivities of the microcantilevers 200x60x6.7 μm^3 (top) & 1000x90x10.9 μm^3 (bottom) in aqueous glycerol solutions.

5.2 Limit of Detection

5.2.1 Definitions and Derivation

The limit of detection (LOD) is a measure of the minimum change of the input quantity to which the sensor can respond. For dynamic mode MEMS-based sensors, the mass limit of detection associated with the *i*-th mode is defined as three times ratio of device frequency noise to the mass sensitivity and is given as

$$LOD_{M,i} = \frac{3\Delta f_{\text{noise},i}}{S_{M,i}}. \tag{5.12}$$

The device frequency noise ($\Delta f_{\text{noise},i}$) is proportional to the phase noise ($\Delta\theta_{\text{n}}$) and the ratio of resonance frequency ($f_{r,i}$) to the quality factor (Q_i) [71] and is given as

$$\Delta f_{\text{noise},i} \approx \frac{f_{r,i}\,\Delta\theta_n}{2Q_i}. \tag{5.13}$$

Substituting Eq. (5.13) into Eq. (5.12), the mass limit of detection is rewritten as

$$LOD_{M,i} = \frac{3f_{r,i}\,\Delta\theta_n}{2Q_i\,S_{M,i}}. \tag{5.14}$$

The phase noise varies with the different sensor systems. In general, the normalized mass limit of detection is defined as the ratio of the mass limit of detection to the phase noise and is given as

$$\overline{LOD}_{M,i} = \frac{LOD_{\text{min},i}}{\Delta\theta_n} = \frac{3f_{r,i}}{2Q_i\,S_{M,i}}. \tag{5.15}$$

It indicates that the normalized mass limit of detection is proportional to the resonance frequency and inversely proportional to both the quality factor and the mass sensitivity.

5.2.2 Trends in the Normalized Mass Limit of Detection as a Function of Microcantilever Geometry

For the case of film without gap (d=0), the normalized mass limit of detection of torsionally vibrating microcantilevers obtained from the ribbon theory [88] and the theory proposed in Chapter 2 are shown and compared in Figure 5-4 as a function of $bL/h^{0.5}$. From Figure 5-4, it is seen that the normalized mass limit of detection in 1st torsional mode is approximately dependent on the parameter $bL/h^{0.5}$ for all investigated microcantilever geometries. It is also shown in Figure 5-4 that, as the aspect ratio (h/b) decreases, the normalized mass limits of detection calculated by the theory in Chapter 2 approach those calculated by ribbon theory. The results also indicate that the difference in the values of normalized mass limit of detection obtained from these two theories could be greater than 7% for microcantilevers with h/b>0.16. This also means that the error in the calculated normalized mass limit of detection for the 1st torsional mode could be also greater than 7% for microcantilevers with h/b>0.16 in water if the thickness effects are ignored.

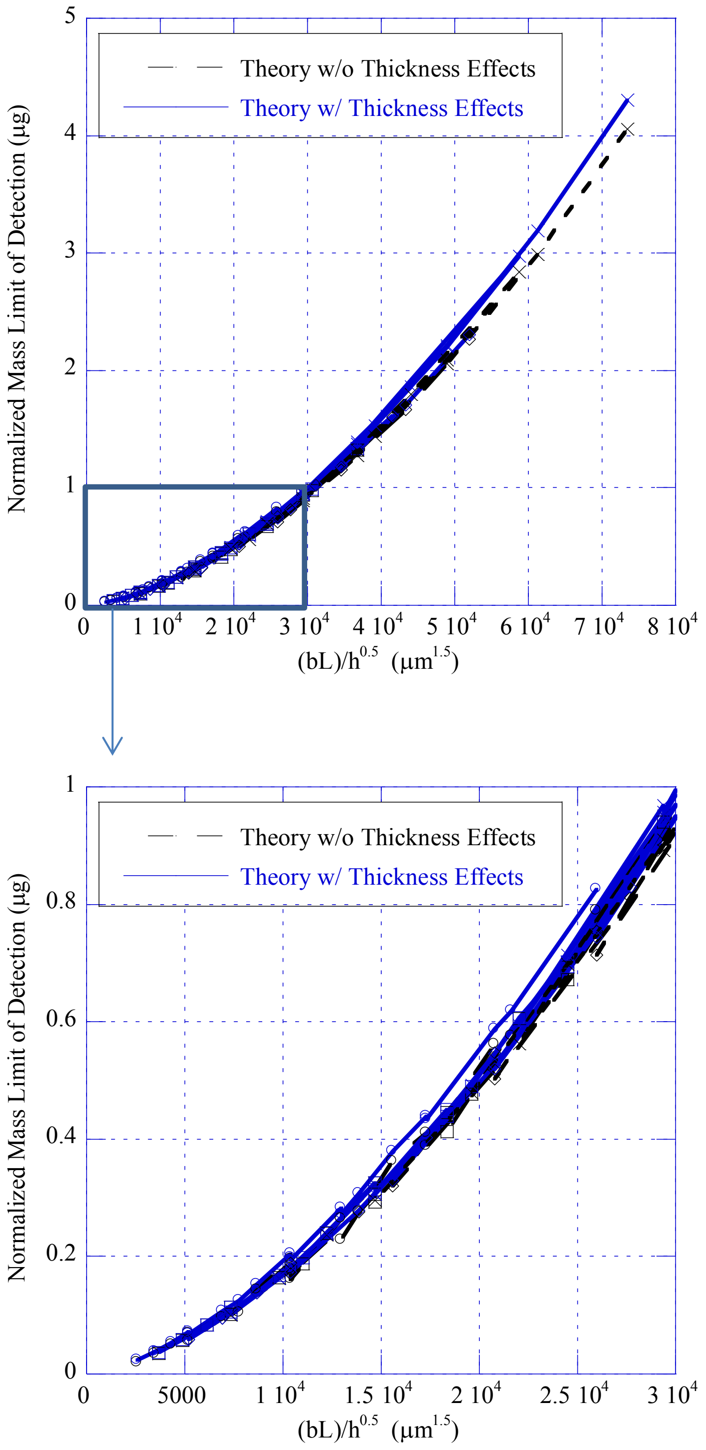

Figure 5-4: Simulated normalized mass limits of detection of silicon microcantilevers vibrating in the first torsional mode in water as a function of $bL/h^{0.5}$ for widths of 45, 60, 75, and 90 µm, lengths of 200, 400, 600, 800, 1000 µm, and thicknesses of 12 µm (o), 6 µm (□), 3 µm (◊), 1.5 µm (×).

5.2.3 Effects of the Liquid Medium's Viscosity on the Normalized Mass Limit of Detection

For the case of film without gap (*d*=0), the normalized mass limits of detection of two specific microcantilever geometries (200x60x6.7 μm^3 and 1000x90x10.9 μm^3) in aqueous glycerol solutions are investigated. The normalized mass limits of detection calculated from the the ribbon theory [88] and the theory proposed in Chapter 2 are shown and compared in Figure 5-5.

When the concentration of the aqueous glycerol solution is below 40%, from Figure 5-5, it is seen that the normalized mass limit of detection increases approximately linearly as the concentration, hence the viscosity of the aqueous glycerol solution increases. It is also shown that the difference between the calculated values of the normalized mass limit of detection obtained from the ribbon theory [88] and the theory proposed in Chapter 2 is very small. This indicates that the thickness effects can be ignored when evaluating the normalized mass limit of detection of the microcantilever, even whose aspect ratio is greater than 0.11, for the 1st torsional mode in aqueous glycerol solutions with the glycerol concentration below 70%.

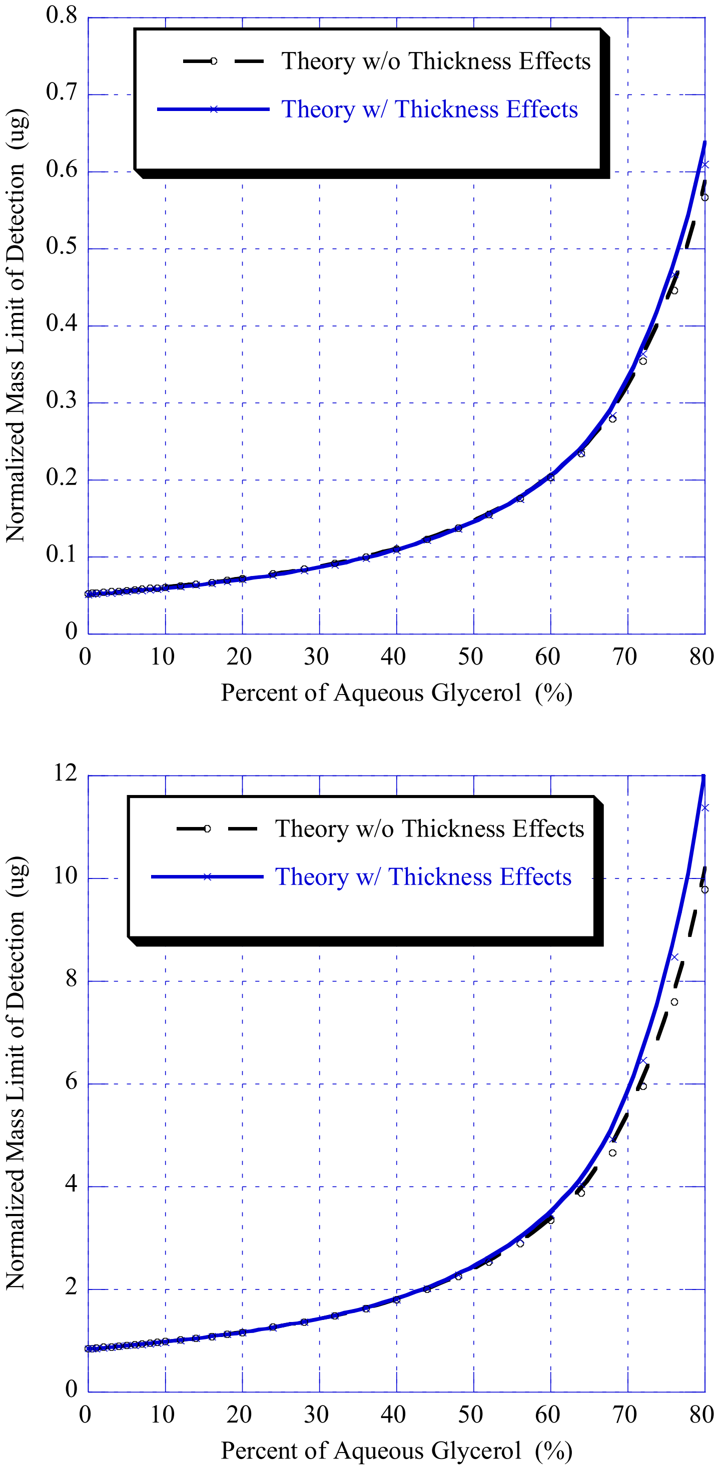

Figure 5-5: Normalized Mass Limits of detection of the microcantilevers 200x60x6.7 μm^3 (top) & 1000x90x10.9 μm^3 (bottom) in aqueous glycerol solutions.

5.3 Designs and Characteristics Calculations of Rectangular Microcantilever Dimensions

For chemical sensing applications, the design/seclection of the microcantilever dimensions is very important. If the *i*-th torsional resonance frequency ($f_{r,i}$) of the microcantilever is given, the following procedures are proposed to calculate the dimension and characteristics of the microcantilever.

(1). For the combination of each Reynolds number (Re) and each aspect ratio (h/b) investigated in this dissertation, calculate the width (b) and thickness (h) of the microcantilever using the following two equations,

$$b = \sqrt{\frac{2\eta \,\mathrm{Re}}{\pi \rho_l f_{r,i}}}, \tag{5.16}$$

$$h = \frac{h}{b} b. \tag{5.17}$$

Eq. (5.16) is written from the definition of the Reynolds number described by Eq. (2.1).

(2). Calculate the length (L) of the microcantilever using the following equation,

$$L = \frac{2i-1}{4f_{r,i}} \sqrt{\frac{GK(1-2\xi_{\mathrm{tors},i}^2)}{\rho J_p + g_{2,\mathrm{tors}}}}, \tag{5.18}$$

with

$$\xi_{\mathrm{tors},i} = \frac{g_{1,\mathrm{tors}}}{4\pi f_{r,i}(\rho J_p + g_{2,\mathrm{tors}})}, \tag{5.19a}$$

$$g_{1,\mathrm{tors}} = \frac{1}{2}\pi\eta \,\mathrm{Re}\, b^2 \Gamma_{\mathrm{rect,tors,imag}}\left(\mathrm{Re}, \frac{h}{b}\right), \tag{5.19b}$$

$$g_{2,\mathrm{tors}} = \frac{\eta \,\mathrm{Re}_i\, b^2 \Gamma_{\mathrm{rect,tors,real}}(\mathrm{Re}_i, h/b)}{4f_{r,i}}. \tag{5.19c}$$

Eqs. (5.19a-c) are written from Eq. (2.41), (2.6), and (2.7), respectively.

(3). Calculate the quality factor, an important parameter in determining the sensing charateristics of the device.

(4). Compare and choose the best reasonable dimension, which induces high quality factor.

By following the above procedures, microcantilevers operating in the first torsional mode in water are designed for given resonance frequencies; the results of the coomputations are listed in Table 5-1. In this table, the subscript N stands for results using the numerical calculated values of the hydrodynamic function. The subscript A stands for results using values of the hydrodynamic function obtained from the analytical expression as described by Eqs. (3.17a-b), which are given in terms of both the Reynolds number and the aspect ratio. The subscript S stands for results using the analytical expression of the hydrodynamic function as described by Eqs. (3.7a-f), which are given only in terms of the Reynolds number [88].

Table 5-1: Dimension and characteristics of designed microcantilevers operating in the 1st torsional mode in water

f_{water} [MHz]	0.25	0.75	1.25	1.25	1.25	1.25	1.25	1.25	1.25
Re	1000	1000	1000	5623	5623	5623	5623	5623	10000
h/b	0.05	0.05	0.05	0.01	0.02	0.05	0.1	0.2	0.2
h [µm]	2.523	1.457	1.128	0.535	1.070	2.676	5.351	10.703	14.273
b [µm]	50.46	29.13	22.57	53.51	53.51	53.51	53.51	53.51	71.36
L_N [µm]	275.97	91.99	55.19	5.95	16.15	57.43	141.15	322.63	323.58
L_A [µm]	279.41	93.14	55.88	6.06	16.45	58.39	142.68	320.96	322.63
L_S [µm]	287.93	95.98	57.59	6.05	16.56	60.05	151.11	358.99	360.64
$(L_A-L_N)/L_N$ [%]	1.25	1.25	1.25	1.86	1.90	1.66	1.08	-0.52	-0.29
$(L_S-L_N)/L_N$ [%]	4.33	4.33	4.33	1.59	2.54	4.56	7.06	11.27	11.45
Q_N [µm]	8.47	8.47	8.47	14.37	15.76	18.58	23.11	29.26	40.55
Q_A [µm]	8.53	8.53	8.53	15.52	16.53	19.36	23.64	31.21	41.50
Q_S [µm]	7.28	7.28	7.28	13.07	13.95	16.58	20.96	29.73	39.59
$(Q_A-Q_N)/Q_N$ [%]	0.69	0.69	0.69	8.05	4.84	4.18	2.29	6.68	2.35
$(Q_S-Q_N)/Q_N$ [%]	-14.06	-14.06	-14.06	-9.01	-11.51	-10.78	-9.29	1.62	-2.36

From Table 5-1, it is seen that the lengths obtained by applying the analytical expression of the hydrodynamic function in terms of both Reynolds number and aspect ratio are very close to those obtained by applying the numerical results of the hydrodynamic function. For some combinations of Reynolds number and aspect ratio, the length obtained is not much larger than the width or even less than the width, which invalidates the assumption of $L>>b$ and should not be chosen even when the resuting quality factor is high. The error on the predicted length or quality factor is determined by the Reynolds number and aspect ratio (h/b) but not dependent on the resonance frequency.

When $h/b \geq 0.05$, the relative error on predicted length and quality factor obtained from the ribbon theory could be larger than 10% and 14%, respectively. Thus it is better to take the thickness effects into account in calculating the length and quality factor when the aspect ratio (h/b) is equal or greater than 0.05. For any given working resonance frequency, some good designs could be found by using the numerical values of the hydrodynamic function at the investigated Reynolds numbers and aspect ratios. For example, for a resonant frequency of 1.25 MHz, the best design is shown in the last column of Table 5-1.

6. SUMMARY, CONCLUSIONS AND FUTURE WORK

6.1 Summary

The primary objective of this study was to theoretically investigate torsionally vibrating resonant rectangular microcantilevers for high performance liquid-phase chemical sensor applications and note the improvement in liquids when the microcantilever is excited in torsional mode compared to transverse mode. Microcantilevers operating in the transverse mode have applications in both gas and liquid phases. However, in liquid phase, this mode of operation does not have good performance because of the larger fluidic resistance inertial and damping forces. In order to improve the characteristics of transversely vibrating microcantilevers, the microcantilevers could be made to operate in the torsional or lateral mode to achieve higher resonance frequency and quality factor, hence higher sensitivity. The lateral mode microcantilevers were widely investigated in the literature [71-86]. The focus in this study is the torsional mode microcantilevers.

Solving for the characteristics of the torsionally vibrating microcantilevers in viscous liquids is a fluid-structure interaction problem. This original complicated problem was divided into two sub-problems: a structure vibration problem with the external resistance inertial and damping torques from the liquid, and a liquid dynamic problem to obtain the resistance inertial and damping torques per unit length by solving the Navier-Stokes equations in the liquid domain.

The equation of motion was first established and solved for the rotational deflection of a microcantilever vibrating torsionally in a viscous liquid. Then the characteristics such as the frequency spectrum, resonance frequency, quality factor, mass sensitivity and normalized mass limit of detection of a microcantilever vibrating torsionally were obtained in analytical forms in terms of the excitation frequency and the hydrodynamic function, which is the normalized hydrodynamic torques per unit length.

The hydrodynamic function was obtained by solving Navier-Stokes equations for incompressible Newtonian liquids. The values of the hydrodynamic function for rectangular microcantilevers at 19 Reynolds numbers and 11 aspect ratios (h/b) were obtained using numerical simulations in COMSOL. Three methods were used to extract the magnitude, phase, real part and imaginary part of the hydrodynamic function in order to confirm the numerical results were convergent and accurate. An analytical expression of the hydrodynamic function was obtained for rectangular microcantilevers vibrating torsionally in viscous liquids by fitting the numerical results.

By using the expressions for the hydrodynamic function (both the real and imaginary parts), the characteristics of torsionally vibrating microcantilevers in viscous liquids were calculated. The resonance frequencies and quality factors of a 400x90x22.3 μm^3 microcantilever vibrating torsionally in water were calculated and compared to available experimental results [125] and to the results for microcantilevers vibrating transversely or laterally. The resonance frequencies, quality factors, mass sensitivity, and normalized mass limit of detection of torsionally vibrating rectangular microcantilevers in viscous liquids such as water and aqueous glycerol solutions were evaluated. The dependencies of the characteristics on the microcantilever geometry and the material properties of the liquid were investigated. In addition, the rectangular microcantilever dimension design procedure was proposed for a given desired resonance frequency.

In summary, the main contributions of this study are as follows:

(1). the hydrodynamic function in terms of both the Reynolds number and the aspect ratio (*h*/*b*) for torsionally vibrating microcantilevers in viscous liquids was obtained by numerical simulations. The numerical values of the hydrodynamic function at the investigated Reynolds numbers and aspect ratios were provided and an analytical expression of the hydrodynamic function was proposed by fitting the numerical data.

(2). the general expressions for the resonance frequency and quality factor of torsionally vibrating microcantilevers in viscous liquids were derived and presented.

(3). the characteristics (resonance frequency, quality factor, mass sensitivity, normalized mass limit of detection) of torsionally vibrating microcantilevers in viscous liquids were calculated and the trends or dependence of the characteristics were investigated as a function of the microcantilever geometry and the material properties (viscosity) of the liquid.

(4). a procedure to design/select the dimension of torsionally vibrating rectangular microcantilever in viscous liquid was presented.

6.2 Conclusions

It was found that the thickness effects on the torsional constant, the hydrodynamic function, polar moment of cross-section area are significant when evaluating the characteristics of torsionally vibrating microcantilevers with $h/b \geq 0.11$, especially $h/b \geq 0.16$, in viscous liquids. The thickness effects could be approximated as the superposition of each effect when evaluating the resonance frequency and quality factor. For example, for the 400x90x22.3 μm^3 microcantilever under first torsional mode in water, ignoring the thickness effect on the torsional constant or the hydrodynamic function increases the calculated values of both the resonance frequency and the quality factor. Ignoring the thickness effect on the polar moment of the cross-section area increases the calculated values of the resonance frequency, but decreases the calculated values of the quality factor. The thickness effect on the torsional constant is dominant when evaluating the resonance frequency. The thickness effects on both the torsional constant and hydrodynamic function are dominant when evaluating the quality factor. This indicates that, in general, all three thickness effects have to be considered when evaluating the characteristics of a torsionally vibrating microcantilever in a viscous liquid.

Furthermore, the characteristics (resonance frequency, quality factor, mass sensitivity, normalized mass limit of detection) of microcantilevers vibrating under the first torsional mode in water and aqueous glycerol solutions were evaluated by using both the ribbon theory [88] ignoring thickness effects, and the theory developed in this dissertation considering all three thickness effects. The characteristics obtained from the theory considering thickness effects was found to approach that obtained from the ribbon theory as the aspect ratio (h/b) decreases. As the viscosity of the liquid medium increases for aqueous glycerol solutions with glycerol concentrations below 40%, the resonance frequency, quality factor, mass sensitivity were found to decrease approximately linearly, whereas the normalized mass limit of detection was found to increase approximately linearly. For the investigated microcantilever geometries, the mass sensitivity in torsional mode was found to be approximately dependent on the parameter $h^{0.5}/(b^2L^{1.5})$ and the normalized mass limit of detection in torsional mode was found to be approximately dependent on the parameter $bL/h^{0.5}$. The mass sensitivity was found to be improved by adding/increasing a gap in the film, whose layout is shown in Figure 5-1. However, it is noted that depositing such film with a gap may not be practical, as it may require the use of additional mask(s).

In addition, the first resonance frequency of a microcantilever operating torsionally, laterally, or transversely in water was found to shift to a lower value compared to that in air, as expected. However, the predicted resonance frequency shifts were found to be different for these three vibration modes. For example, the first lateral resonance frequencies only drop by a value of up to 10% while the first transverse and first torsional resonance frequencies drop by as much as 50% and 32%, respectively. The first resonance frequency of laterally or torsionally vibrating microcantilevers in water was found to be much higher than that of transversely vibrating microcantilevers with the same geometries. For liquid-phase chemical sensor applications, it is more advantageous to operate in the first tosional or first lateral mode because the sensitivity of a microcantilever as a chemical sensor is proportional to its resonance frequency. For the same geometry, the quality factor of microcantilevers vibrating in the first torsional or first lateral mode was found to be much higher than that of microcantilevers vibrating in the first transverse mode. The quality factor was found to increase as the length of the microcantilever decreases or as the thickness of the microcantilever increases for all three modes. However, as the width of the microcantilever increases, the quality factor was found to increase for the transverse or lateral mode, whereas it remains almost constant for the torsional mode.

Finally, The resonance frequency is found to be dependent on $h/(bL)$ and the quality factor is found to be dependent on $h/L^{0.5}$ for microcantilevers vibrating under the first torsional mode in viscous liquids. In contrast, for microcantilevers vibrating under the first lateral mode, the resonance frequency is dependent on b/L^2 and the quality factor is dependent on $hb^{0.5}/L$ [82-84]. Such different trends can be used to optimize device geometry and maximize frequency stability in chemical sensing applications.

6.3 Future Work

The work done in this dissertation can easily be expanded upon and improved. In this study, the microcantilever is assumed to be perfectly clamped on one end and the support effect was not considered. Basically, ignoring the support effect overestimates the stiffness of the system and thus overestimates the resonance frequency. For torsionally vibrating microcantilevers, the shorter the microcantilever, the higher the resonance frequency, quality factor, mass sensitivity and the lower the limit of detection. But if the microcantilever is too short, the support effect will not be negligible. The support effect of torsionally vibrating microcantilevers in viscous liquids could be modeled by a cantilever with a support spring or beam. The hydrodynamic function for torsional mode proposed in Chapter 3 could be used in this model to evaluate the hydrodynamic resistance torque per unit length acted on the microcantilever from the liquid.

In this study, only microcantilevers in viscous liquids were investigated and the sensing layer film was assumed to have negligible mass and stiffness. Actually, both the mass and the stiffness of the film change as the analyte is sorbed. A model to simulate the viscoelastic film is needed to extend the study in this dissertation and predict the characteristics of the system more accurately. Furthermore, in the range of the small thickness of the film compared to the thickness of the microcantilever, the thicker the film, the higher the mass sensitivity. So the thickness of the film is another parameter that should be optimized.

In this study, only microcantilevers with uniform rectangular cross-section were investigated. Although microcantilevers with some other shapes such as T-shape (hammerhead) beams [54,90-91,98-100], U-shaped beams [54], V-shaped beams [53-54] have also been investigated and described in the literature, most of the published work focused on the transverse or lateral mode. The work done in this dissertation could be extended to model microcantilevers with some other shapes such as T-shape and the trampoline-shape micro-structures [101-104]. Especially for the T-shape (hammerhead) microcantilevers, the hydrodynamic function proposed in Chapter 3 could be directly used to evaluate the liquid resistance torque per unit length.

Comparison of the different dynamic modes is also important to optimize the microcantilever geometry in a liquid medium. Transverse mode microcantilever-based sensors have found many (bio)chemical applications, especially in air. Lateral and torsional mode microcantilever-based sensors have much better performance in liquid-phase sensing applications. Beside these three modes, the microcantilevers operating in longitudinal mode [95-96] or coupled mode [97] could be also valuable and should be investigated.

BIBLIOGRAPHY

[1] K. Iniewski, *Optical, Acoustic, Magnetic, and Mechanical Sensor Technologies*, New York: CRC Press, Taylor & Francis Group, 2012.

[2] A. M. K. Dagamseh, T. S. J. Lammerink, M. L. Kolster, C. M. Bruinink, R. J. Wiegerink, and G. J. M. Krijnen, "Dipole-source localization using biomimetic flow-sensor arrays positioned as lateral line system," *Sensors and Actuators A: Physical*, 162, pp. 355-360, 2010.

[3] K. A. A. Makinwa, and J. H. Huijsing, "A smart wind sensor using thermal sigma-delta modulation techniques," *Sensors and Actuators A: Physical*, 97-98, pp. 15-20, 2002.

[4] F. Kohl, R. Fashing, F. Keplinger, R. Chabicovsky, A. Jachimowicz, and G. Urban, "Development of miniaturized semiconductor flow sensors," *Measurement*, 33, pp. 109-119, 2003.

[5] P. Furjes, G. Legradi, Cs. Ducso, A. Aszodi, and I. Barsony, "Thermal characterization of a direction dependent flow sensor," *Sensors and Actuators A: Physical*, pp. 417-423, 2004.

[6] J. Laconte, J. –P. Raskin, and D. Flandre, *Micromachined Thin-Film Sensors for SOI-CMOS Co-integration*, Dordrecht, The Netherlands: Springer Science, pp. 186, 2006.

[7] L. Moreno-Hagelsieb, P. E. Lobert, R. Pampin, D. Bourgeois, J. Remacle, D. Flandre, "Sensitive DNA electrical detection based on interdigitated Al/Al_2O_3 microelectrodes," *Sensors and Actuators B: Chemical*, 98, pp. 269-274, 2004.

[8] N. Andre, S. Druart, P. Gerard, R. Pampin, L. Moreno-Haglesieb, T. Kezai, L. A. Francis, D. Flandre, and J. –P. Raskin, "Miniaturized wireless sensing system for real-time breath activity recording," *IEEE Sensors Journal*, 10 pp. 178-184, 2010.

[9] B. Calhoun, D. Daly, N. Verma, D. Finchelstein, D. Wentzloff, A. Wang, S. –H. Cho, and A. Chandrakasan, " Design considerations for ultra-low energy wireless microsensor nodes," *IEEE Transactions on Computers*, 54(6), pp. 727-740, 2005.

[10] M. Hempstead, N. Tripathi, P. Mauro, G. –Y. Wei, and D. Brooks, "An ultra low power system architecture for sensor network applications," in *Proceedings of the 32nd International Symposium on Computer Architecture ISCA 2005*, June 4-8, 2005, pp. 208-219.

[11] T. Hui Teo, G. K. Lim, D. Sutomo, K. H. Tan, P. K. Gopalakrishnan, and R. Singh, "Ultra low-power sensor node for wireless health monitoring system," in

Proceedings of the IEEE International Symposium on Circuits and Systems ISCAS 2007, May 27-30, 2007, pp. 2363-2366, 2007.

[12] S. Beeby, M. Tudor, and N. White, "Energy harvesting vibration sources for microsystems applications," *Measurement Science and Technology*, 17(12), R175-R195, 2006.

[13] T. Sterken, P. Fiorini, K. Baert, R. Puers and G. Borghs, "An electret-based electrostatic u-generator," in *Proceedings of the 12th International Conference on Transducers, Solid-State Sensors, Actuators and Microsystems,* vol. 2, pp. 1291-1294, 2003.

[14] P. Glynne-Jones, M. Tudor, S. Beeby, and N. White, "An electromagnetic, vibration-powered generator for intelligent sensor systems, *Sensors and Actuators A: Physical*, 110, pp. 344-349, 2004.

[15] S. Roundy, P. K. Wright, and J. Rabaey, "A study of low level vibrations as a power source for wireless sensor nodes," *Computer Communications*, 26, pp. 1131-1144, 2003.

[16] A. J. du Plessis, M. J. Huigsloot, and F. D. Discenzo, "Resonant packaged piezoelectric power harvester for machinery health monitoring," *Proceedings of SPIE*, 5762(1), pp224-235, 2005.

[17] S. W. Arms, C. P. Townsend, D. L. Churchill, J. H. Galbreath, and S. W. Mundell, "Power management for energy harvesting wireless sensors," *Proceedings of SPIE*, 5763(1), pp267-275, 2005.

[18] T. Tsurumi, H, Kakemoto, and S. Wada, "Dielectric, elastic and piezoelectric losses of PZT ceramics in the resonance state," in *Proceedings of the 13th IEEE International Symposium on Application of Ferroelectrics ISAF 2002*, pp. 375-378, 2002.

[19] U. Dibbern, "A substrate for thin-film gas sensors in microelectronic technology," *Sensors and Actuators B: Chemical,* 2(1), pp. 63-70, 1990.

[20] J. W. Gardner, A. Pike, N. F. De Rooij, M. Koudelka-Hep, P. A. Clerc, A. Hierlemann, and W. Gopel, "Integrated array sensor for detecting organic solvents," *Sensors and Actuators B: Chemical,* 26(1-3), pp. 135-139, 1995.

[21] D. Briand, A. Krauss, B. van der Schoot, U. Weimar, N. Barsan, W. Gopel, and N. F. de Rooij, "Design and fabrication of high-temperature micro-hotplates for drop-coated gas sensors," *Sensors and Actuators B: Chemical,* 68(1-3), pp. 223-233, 2000.

[22] H. Campanella, *Acoustic Wave and Electromechanical Resonators: Concept to Key Applications*: Boston, Artech House, 2010.

[23] F. R. Blom, et al, “Dependence of the Quality Factor of Micromachined silicon Beam Resonators on Pressure and Geometry,” *Journal of Vacuum Science and Technology B*, vol. 10, pp. 19-26, 1992.

[24] R. A. Mangiarotty, “Acoustic Radiation Damping of Vibrating Structures,” *Journal of the Acoustical Society of America*, vol. 35, pp. 369-377, 1963.

[25] H. Hosaka, K. Itao, and S. Kuroda, “Damping Characteristics of Beam-Shaped Micro-Oscillators,” *Sensors and Actuators A: Physical*, vol. 49, pp. 87-95, 1995.

[26] E. Sanin, “MEMS Resonant Sensors: An Overview,” B.S. Thesis, University of Toronto, March 2007.

[27] A.M. Madni and L.A. Wan, “Microelectromechanical Systems (MEMS): An Overview of Current State-of-the-Art,” in *Proceedings of the IEEE Aerospace Conference*, pp. 421-427, 1998.

[28] J.M. Lippmann, “Design and Fabrication of MEMS Resonant Strain Sensor in SOI,” M.S. thesis, University of California at Berkley, Berkley, CA, USA, 2004.

[29] D.W. Carr, and H.G. Craighead, “Fabrication of Nanoelectromechanical Systems in Single Crystal Silicon Using Silicon on Insulator Substrates and Electron Beam Lithography,” *Journal of Vacuum Science & Technology B: Microelectronics and Nanometer Structures*, vol. 15, iss. 6, pp. 2760-2763, 1997.

[30] C.T.-C. Nguyen, “Micromechanical Signal Processors,” Ph.D. Dissertation, University of California at Berkley, Berkley, CA, USA, 1994.

[31] B. Ilic, and H.G. Craighead, “Attogram Detection Using Nanoelectro-mechanical Oscillators,” *Journal of Applied Physics*, vol. 95, no. 7, pp. 3694-3703, April 2004.

[32] Z. Hao, R. Abdolvand, and F. Ayazi, “A High-Q Length-Extensional Bulk-Mode Mass Sensor with Annexed Sensing Platforms,” presented at *19th IEEE International Conference on Micro Electro Mechanical Systems*, Istanbul, Turkey, 2006.

[33] S.X.P. Su, H.S. Yang, and A.M. Agogino, “A Resonant Accelerometer with Two-Stage Microleverage Mechanisms Fabricated by SOI-MEMS Technology,” *IEEE Sensors Journal*, vol. 5, no. 6, pp. 1214-1223, December 2005.

[34] Y.M. Tseytlin, “High resonant mass sensor evaluation: An effective method,” *Review of Scientific Instruments*, vol. 76, no. 11, pp. 115101.1-115101.6, 2005.

[35] Y. Lee, G. Lim, and W. Moon, “A self-excited micro cantilever biosensor actuated by PZT using the mass micro balancing technique,” *Sensors and Actuators A*, vol. 130-131, pp. 105-110, 2006.

[36] I.B. Bahadur, J. Mills, and Y. Sun, "Design of MEMS-Based Resonant Force Sensor for Compliant, Passive Microgripping," in *Proceedings of the IEEE International Conference on Mechatronics & Automation Niagara Falls*, Canada, pp. 77-82, 2005.

[37] A. Qiu, S. Wang, and B. Zhou, "A Micromachined Resonant Gyroscope," presented at *Fifth International Symposium on Instrumentation and Control Technology*, 2003.

[38] J.R. Westra, C.J.M Verhoeven, and A.H.M van Roermund, "Resonance-Mode Selection and Crosstalk Elimination Using Resonator-Synchronised Relaxation Oscillators," in *Proceedings of the 24th European Solid-State Circuits Conference*, pp. 88-91, 1998.

[39] K.E. Wojciechowski, B.E. Boser, and A.P. Pisano, "A MEMS Resonant Strain Sensor Operated in Air," presented at *17th IEEE International Conference on Micro Electro Mechanical Systems*, 2004.

[40] R. Liu, and B. Paden, "MEMS Resonators That Are Robust to Process-Induced Feature Width Variation," *Journal of Microelectromechanical Systems*, vol. 11, no. 5, October 2002.

[41] L. He, Y.-P. Xu, and A. Qiu, "Folded Silicon Resonant Accelerometer with Temperature Compensation," in *Proceedings of IEEE Sensors*, pp. 512-515, 2004.

[42] N.V. Lavrik, and P.G. Datskos, "Femtogram Mass Detection Using Photothermally Actuated Nanomechanical Resonators," *Applied Physics Letters*, vol. 82, no. 16, pp. 2697-2699, April 2003.

[43] G. Zhou, and P. Dowd, "Tilted Folded-Beam Suspension for Extending the Stable Travel Range of Comb-Drive Actuators," *Journal of Micromechanics and Microengineering*, vol. 13, pp. 178-183, 2003.

[44] C. Vancura, Y. Li, J. Lichtenberg, K.-U. Kirstein, A. Hierlemann, and F. Josse, "Liquid-Phase Chemical and Biochemical Detection Using Fully Integrated Magnetically Actuated Complementary Metal Oxide Semiconductor Resonant Cantilever Sensor Systems," *Analytical Chemistry*, vol. 79, pp. 1646-1654, 2007.

[45] X. Xu and A. Raman, "Comparative dynamics of magnetically, acoustically, and Brownian motion driven microcantilevers in liquids," *Journal of Applied Physics*, vol. 102, 034303, pp. 1-8, 2007.

[46] W.A. Johnson, and L.K. Warne, "Electrophysics of Micromechanical Comb Actuators," *Journal of Microelectromechanical Systems*, vol. 4, no.1, pp. 49-59, March 1995.

[47] A.A. Seshia, W. Low, S.A. Bhave, R.T. Howe, and S. Montague, "Micromechanical Pierce Oscillator for Resonant Sensing Applications," *Nanotech*, vol. 1, pp. 162-165, 2002.

[48] C.H. Nguyen, S.J. Pietrzko, "FE Analysis of a PZT-Actuated Adaptive Beam with Vibration Damping Using a Parallel R-L Shunt Circuit," *Finite Elements in Analysis and Design*, vol. 42, is. 14, pp. 1231-1239, October 2006.

[49] T.A. Roessig, R.T. Howe, and A.P. Pisano, "Surface-Micromachined 1MHz Oscillator with Low-Noise Pierce Configuration," in *Solid State Sensor and Actuator Workshop*, Hilton Head, 1998.

[50] M. Wenzel, "Polymer-Coated and Polymer-Based Microcantilever Chemical Sensors: Analysis and Sensor Signal Processing," Ph.D. Dissertation, Marquette University, Milwaukee, WI, USA, August 2009.

[51] W.-H. Chu, Technical Report No. 2, DTMB, Contract Nobs-86396(X), Southwest Research Institute, San Antonio, Texas, 1963.

[52] U. S. Lindholm, D. D. Kana, W.-H. Chu, and H. N. Abramson, "Elastic Vibration Characteristics of Cantilever Plates in Water," *Journal of Ship Research,* pp. 11-22, 1965.

[53] C. P. Green, H. Lioe, J. P. Cleveland, R. Proksch, P. Mulvaney, and J. E. Sader, "Normal and torsional spring constants of atomic force microscope cantilevers," *Review of Scientific Instruments,* vol. 75, pp. 1988-1996, 06/00/ 2004.

[54] S. Basak, A. Raman, and S. V. Garimella, "Hydrodynamic loading of microcantilevers vibrating in viscous fluids," *Journal of Applied Physics,* vol. 99, 114906, pp. 1-10, 06/01/ 2006.

[55] C. A. Van Eysden and J. E. Sader, "Small amplitude oscillations of a flexible thin blade in a viscous fluid: Exact analytical solution," *Physics of Fluids,* vol. 18, 123102, pp. 1-11, 12/00/ 2006.

[56] C. A. Van Eysden and J. E. Sader, "Resonant frequency of a rectangular cantilever beam immersed in a fluid," *Journal of Applied Physics*, vol. 100, 114916, pp. 1-8, 2006.

[57] C. A. Van Eysden and J. E. Sader, "Frequency response of cantilever beams immersed in viscous fluids with applications to the atomic force microscope: Arbitrary mode order," *Journal of Applied Physics,* vol. 101, 044908, pp. 1-11, 2007.

[58] C. A. Van Eysden and J. E. Sader, "Compressible viscous flows generated by oscillating flexible cylinders," *Physics of Fluids*, vol. 21, 013104, pp. 1-12, 2009.

[59] C. A. Van Eysden and J. E. Sader, "Frequency response of cantilever beams immersed in compressible fluids with applications to the atomic force microscope," *Journal of Applied Physics,* vol. 106, 094904, pp. 1-8, 2009.

[60] B. N. Johnson and R. Mutharasan, "Persistence of bending and torsional modes in piezoelectric-excited millimeter-sized cantilever (PEMC) sensors in viscous liquids – 1 to 10^3 cP", *Journal of Applied Physics*, vol. 109, 066105, pp. 1-3, 2011.

[61] E. O. Tuck, "Calculation of unsteady flows due to small motions of cylinders in a viscous fluid," *Journal of Engineering Mathematics,* vol. 3, p. 29, 1969.

[62] J. E. Sader, "Frequency response of cantilever beams immersed in viscous fluids with applications to the atomic force microscope," *Journal of Applied Physics,* vol. 84, pp. 64-76, 1998.

[63] J. W. M. Chon, P. Mulvaney, and J. E. Sader, "Experimental validation of theoretical models for the frequency response of atomic force microscope cantilever beams immersed in fluids," *Journal of Applied Physics,* vol. 87, pp. 3978-3988, 04/15/ 2000.

[64] Z. J. Davis, G. Abadal, O. Kuhn, O. Hansen, F. Grey, and A. Boisen, "Fabrication and characterization of nanoresonating devices for mass detection," *Journal of Vacuum Science & Technology B*, vol. 18, no. 2, pp. 612-616, 2000.

[65] D. Lange, C. Hagleitner, A. Hierlemann, O. Brand, and H. Baltes, "Complementary Metal Oxide Semiconductor Cantilever Arrays on a Single Chip: Mass-Sensitive Detection of Volatile Organic Compounds," *Analytical Chemistry,* vol. 74, pp. 3084-3095, 2002/07/01 2002.

[66] L. A. Pinnaduwage, V. Boiadjiev, J. E. Hawk, and T. Thundat, "Sensitive detection of plastic explosives with self-assembled monolayer-coated microcantilevers," *Applied Physics Letters*, vol. 83, no. 7, pp. 1471, 2003.

[67] A. Maali, C. Hurth, R. Boisgard, C. Jai, T. Cohen-Bouhacina, and J.-P. Aime, "Hydrodynamics of oscillating atomic force microscopy cantilevers in viscous fluids," *Journal of Applied Physics,* vol. 97, 074907, pp. 1-6, 2005.

[68] J. Verd, A. Uranga, J. Teva, G. Abadal, F. Torres, N. Barniol, F. Perez-Murano, and J. Esteve, "CMOS cantilever-based oscillator for attograms mass sensing," in *Proceedings of the IEEE International Symposium on Circuits and Systems ISCAS 2007*, May 27-30, 2007, pp. 3319-3322, 2007.

[69] J. Lu, T. Ikehara, Y. Zhang, T. Mihara, T. Itoh, and R. Maeda, "High quality factor silicon cantilever driven by PZT actuator for resonant based mass detection," in *Design, Test, Integration and Packaging of MEMS/MOEMS. Symposium on*, pp. 60-65, 2008.

[70] M. Aureli, M. E. Basaran, and M. Porfiri, “Nonlinear finite amplitude vibrations of sharp-edged beams in viscous fluids,” *Journal of Sound and Vibration,* vol. 331, pp. 1624-1654, 3/26/ 2012.

[71] I. Dufour; S.M. Heinrich; F. Josse, “Strong-axis bending mode vibrations for resonant microcantilever (bio)chemical sensors in gas or liquid phase,” *Frequency Control Symposium and Exposition, Proceedings of the 2004 IEEE International*, pp. 193-199, 23-27 August 2004.

[72] Xiaoyuan Xia; Ping Zhou; Xinxin Li, “Effect of Resonance-mode Order on Mass-sensing Resolution of Microcantilever Sensors,” *IEEE Sensors Conference*, Lecce, Italy, pp. 577-580, 2008.

[73] D. R. Brumley, M. Willcox, and J. E. Sader, “Oscillation of cylinders of rectangular cross section immersed in fluid,” *Physics of Fluids,* vol. 22, 052001, pp. 1-15, 05/00/ 2010.

[74] D. R. Brumley, M. Willcox, and J. E. Sader, “Erratum: Oscillation of cylinders of rectangular cross section immersed in fluid" [Phys. Fluids [bold 22], 052001 (2010)],” *Physics of Fluids,* vol. 22, pp. 099902-1, 09/00/ 2010.

[75] Stokes, G., “On the Effects of the Internal Friction of Fluids on the Motion of Pendulums,” *Transactions of the Cambridge Philosophical Society*, vol. 9, pp. 8-106, 1851.

[76] Russell Cox, “Theoretical Analysis of Dynamically Operating Polymer-Coated Microcantilever Chemical Sensors in a Viscous Liquid Medium,” Master Thesis, Marquette University, August 2007.

[77] L. A. Beardslee, A. M. Addous, S. Heinrich, F. Josse, I. Dufour, and O. Brand, “Thermal Excitation and Piezoresistive Detection of Cantilever In-Plane Resonance Modes for Sensing Applications,” *Microelectromechanical Systems, Journal of,* vol. 19, pp. 1015-1017, 2010.

[78] S. M. Heinrich, R. Maharjan, L. Beardslee, O. Brand, I. Dufour, and F. Josse, “An analytical model for in-plane flexural vibrations of thin cantilever-based sensors in viscous fluids: applications to chemical sensing in liquids,” *Proceedings, International Workshop on Nanomechanical Cantilever Sensors*, Banff, Canada, pp. 2, 2010.

[79] S. M. Heinrich, R. Maharjan, I. Dufour, F. Josse, L. Beardslee, and O. Brand, “An analytical model of a thermally excited microcantilever vibrating laterally in a viscous fluid,” *Proceedings IEEE Sensors 2010 Conference*, Waikoloa, Hawaii, pp. 1399-1404., 2010.

[80] R. Cox, F. Josse, S. Heinrich, I. Dufour, and O. Brand, “Resonant microcantilevers vibrating laterally in viscous liquid media,” in *Frequency Control Symposium (FCS), 2010 IEEE International*, 2010, pp. 85-90.

[81] R. Cox, J. Zhang, F. Josse, S. M. Heinrich, I. Dufour, L. A. Beardslee*, et al.*, "Damping and mass sensitivity of laterally vibrating resonant microcantilevers in viscous liquid media," in *Frequency Control and the European Frequency and Time Forum (FCS), 2011 Joint Conference of the IEEE International*, 2011, pp. 1-6.

[82] R. Cox, "Theoretical analysis of laterally vibrating microcantilever sensors in a viscous liquid medium," Ph.D. Dissertation, Marquette University, Milwaukee, WI, USA, May 2011.

[83] Y. Tao, X. Li, T. Xu, H. Yu, P. Xu, B. Xiong, and C. Wei, "Resonant cantilever sensors operated in a high-Q in-plane mode for real-time bio/chemical detection in liquids," *Sensors and Actuators B: Chemical*, vol. 157, pp. 606-614, 2011.

[84] R. Cox, F. Josse, S. M. Heinrich, O. Brand, and I. Dufour, "Characteristics of laterally vibrating resonant microcantilevers in viscous liquid media," *Journal of Applied Physics,* vol. 111, 014907, pp. 1-14, 2012.

[85] L.B. Sharos; A. Raman; S. Crittenden; and R. Reifenberger, "Enhanced mass sensing using torsional and lateral resonances in microcantilevers," *Applied Physics Letters*, vol. 84, no. 23, pp. 4638-4640, 2004.

[86] B. N. Johnson, H. Sharma, and R. Mutharasan, "Torsional and Lateral Resonant Modes of Cantilevers as Biosensors: Alternatives to Bending Modes", *Analytical Chemistry*, 85, pp. 1760-1766, 2013.

[87] G. G. Stokes, "On the Effect of the Rotations of the Cylinders or Spheres round their own Axes in increasing the Logarithmic Decrement of the Arc of Vibration," in *Mathematical and Physical Papers*, Cambridge, United Kingdom: Cambridge University Press, pp. 207-214, 1886.

[88] C. P. Green and J. E. Sader, "Torsional frequency response of cantilever beams immersed in viscous fluids with applications to the atomic force microscope," *Journal of Applied Physics,* vol. 92, pp. 6262-6274, 11/15/ 2002.

[89] X. Hui, J. Vitard, S. Haliyo, and S. Regnier, "Enhanced Sensitivity of Mass Detection Using the First Torsional Mode of Microcantilevers," in *Mechatronics and Automation, 2007. ICMA 2007. International Conference on*, 2007, pp. 39-44.

[90] Nic Mullin; Cvetelin Vasilev; Jaimey D. Tucker; etc., "Torsional tapping atomic force microscopy using T-shaped cantilevers," *Applied Physics Letters*, 94, 173109, 2009.

[91] M.G. Reitsma; R.S. Gates; R.F. Cook, "Torsional spring constant measurement of a T-shaped atomic force microscope cantilever," *Proceedings of the SEM Annual Conference*, Albuquerque, New Mexico, USA, 2009.

[92] T. Cai, F. Josse, I. Dufour, S. Heinrich, N. Nigro, and O. Brand, "Resonant characteristics of rectangular microcantilevers vibrating torsionally in viscous liquid media," in *Frequency Control Symposium (FCS), 2012 IEEE International*, 2012, pp. 1-6.

[93] M. Aureli, C. Pagano, and M. Porfiri, "Nonlinear finite amplitude torsional vibrations of cantilevers in viscous fluids," *Journal of Applied Physics,* vol. 111, 124915, pp. 1-16, 2012.

[94] P. H. Kim, C. Doolin, B. D. Hauer, A. J. R. MacDonald, M. R. Freeman et al, "Nanoscale torsional optomechanics", *Applied Physics Letters*, 102, 053102, 2013.

[95] W. Y. Shih; Q. Zhu; and W.-H. Shih, "Length and thickness dependence of longitudinal flexural resonance frequency shifts of a piezoelectric microcantilever sensor due to Young's modulus change," *Journal of Applied Physics*, vol. 104, 074503, pp. 1-5, 2008.

[96] G. Iosilevskii, "Longitudinal Waves in a Submerged Cylindrical Rod," *Journal of Applied Mechanics*, 78, 024502, 2011.

[97] Y. Song and B. Bhushan, "Coupling of cantilever lateral bending and torsion in torsional resonance and lateral excitation modes of atomic force microscopy," *Journal of Applied Physics,* vol. 99, 094911, pp. 1-12, 2006.

[98] S.-D. Kwon, "A T-shaped piezoelectric cantilever for fluid energy harvesting," *Applied Physics Letters*, vol. 97, 164102, pp. 1-3, 2010.

[99] J. E. Kim and Y. Y. Kim, "Analysis of Piezoelectric Energy Harvesters of a Moderate Aspect Ratio With a Distributed Tip Mass," *Journal of Vibration and Acoustics*, vol. 133, 041010-16, 2011.

[100] J. Zhang, "Theoretical Analysis of Laterally Vibrating Hammerhead Microcantilevers for Liquid-Phase Sensing Applications," Ph.D. Dissertation, Marquette University, Milwaukee, WI, May, 2013.

[101] A. Manut and M. I. Syono, "Effects of Mechanical Geometries on Resonance Sensitivity of MEMS Out-of-Plane Accelerometer," in *Semiconductor Electronics, 2006. ICSE '06. IEEE International Conference on*, 2006, pp. 25-28.

[102] C. Riesch, E. K. Reichel, A. Jachimowicz, J. Schalko, B. Jakoby, and F. Keplinger, "A micromachined suspended plate viscosity sensor featuring in-plane vibrations and integrated piezoresistive readout," in *Solid-State Sensors, Actuators and Microsystems Conference, 2009. TRANSDUCERS 2009. International*, 2009, pp. 1178-1181.

[103] P. S. Waggoner, C. P. Tan, L. Bellan, and H. G. Craighead, "High-Q, in-plane modes of nanomechanical resonators operated in air," *Journal of Applied Physics,* vol. 105, 094315, pp. 1-6, 05/01/ 2009.

[104] K. Park, J. Shim, V. Solovyeva, E. Corbin, S. Banerjee, and R. Bashir, “Hydrodynamic loading and viscous damping of patterned perforations on microfabricated resonant structures,” *Applied Physics Letters,* vol. 100, 154107, pp. 1-5, 04/09/ 2012.

[105] Amir Rahafrooz and Siavash Pourkamali, “Rotational Mode Disk Resonators for High-Q Operation in Liquid,” Proc. IEEE Sensors Conference, (2010).

[106] Amir Rahafrooz and Siavash Pourkamali, “Characterization of Rotational Mode Disk Resonator Quality Factors in Liquid,” IFCS/EFTF Joint Conference, May 2011, San Francisco, CA, pp. 198.

[107] Jae Hyeong Seo and Oliver Brand, “High Q-Factor In-Plane-Mode Resonant Microsensor Platform for Gaseous/Liquid Environment,” JMEMS, 17(2), 483-493, (2008).

[108] S. Timoshenko and J. N. Goodier, *Theory of Elasticity, by S. Timoshenko and J. N. Goodier, 2nd Edition*: McGraw-Hill book Company, 1951.

[109] I. S. Sokolnikoff, *Mathematical theory of elasticity*: McGraw-Hill, 1956.

[110] L. D. Landau and E. M. Lifshitz, *Theory of elasticity*: London, Reading, Mass.,: Pergamon Press; Addison-Wesley Pub. Co., 1959.

[111] M. Itskov, *Tensor algebra and Tensor Analysis for Engineers*: Springer, New York, 2007.

[112] Y. L. Luke, *The Special Functions and Their Approximations*: Academic, New York, 1969.

[113] W. F. Hughes, *An Introduction to Viscous Flow*: McGraw-Hill, New York, 1979.

[114] G. K. Batchelor, *Introduction to Fluid Dynamics*: New York: Cambridge University Press, 1977.

[115] L. Rosenhead, *Laminar Boundary Layers*: Clarendon, Oxford, 1963.

[116] W. C. Young, R. J. Roark, and R. G. Budynas, *Roark's formulas for stress and strain*, 7th ed. New York: McGraw-Hill, 2002.

[117] C. R. Weast, ed., *Handbook of Chemisttry and Physics*, Ohio, 54th edition, 1973.

[118] C. R. Weast, ed., *Handbook of Chemistry and Physics*, Ohio, 65th edition, 1984.

[119] COMSOL 4.1 documentations. COMSOL, Inc. Los Angeles, CA 90024: COMSOL, Inc., 2011.

[120] C.-C. Liang, C.-C. Liao, Y.-S. Tai, and W.-H. Lai, "The free vibration analysis of submerged cantilever plates," *Ocean Engineering,* vol. 28, pp. 1225-1245, 9// 2001.

[121] M. U. Demirci and C. T. C. Nguyen, "Mechanically Corner-Coupled Square Microresonator Array for Reduced Series Motional Resistance," *Journal of Microelectromechanical Systems,* vol. 15, pp. 1419-1436, 2006.

[122] V. Agache, M. Cochet, R. Blanc, F. Baleras, and P. Caillat, "High Q factor plate resonators for ultrasensitive mass sensing applications," in *Solid-State Sensors, Actuators and Microsystems Conference, 2009. TRANSDUCERS 2009. International*, 2009, pp. 1630-1633.

[123] C.-C. Ma and K.-C. Chuang, "A Point-Wise Fiber Bragg Grating Sensor to Measure the Vibration of a Cantilever Plate Subjected to Impact Loadings," *Sensors Journal, IEEE,* vol. 11, pp. 2113-2121, 2011.

[124] M. A. Hopcroft, W. D. Nix, and T. W. Kenny, "What is the Young's Modulus of Silicon?" *Journal of Microelectromechanical System*, vol. 19, no. 2, pp. 229-238, 2010.

[125] The experimental data are provided by Dr. Oliver Brand from the Center for MEMS and Microsystems Technologies at Georgia Institute of Technology in collaboration with the Microsensor Research Lab at Marquette University.

APPENDIX A JAVA PROGRAM USED TO GENERATE COMSOL MODELS AND COMPUTE NORMALIZED TORQUE PER UNIT LENGTH

```
/*
 * Torsional_Rect_Fluid_2D.java
 */

import com.comsol.model.*;
import com.comsol.model.util.*;
import java.io.IOException;
import java.io.BufferedReader;
import java.io.File;
import java.io.FileReader;


public class Torsional_Rect_Fluid_2D {
  static String[] vWidth, vAspectRatio, vNumNode, vPara, vReynolds, vGeoRatio;
  static int[]    vnStEdW, vnStEdAR, vnStEdCase, vnStEdRe;
  static String[] vstOutBC = {"Pressure", "PressureNoViscousStress"};
  static Model    model = ModelUtil.create("Model"); // Global Definitions and Results
  static String   stPath;


  public static void main(String[] args) {
  /* Function: COMSOL Modeling, Calculation and Postprocessing
     Called by: None
     Call:      read_parameters(path)
                              pre0_parameter(iWi, jAr, kRe, iCase)
                pre1_view(s_Width, s_GeoRatio)
                pre2_geometry()
                pre3_selection()
                pre4_material()
                pre5_physics(iCase)
                pre6_mesh()
                pre7_solution(iWi, jAr, kRe, iCase)
                post_processing(iWi, jAr, kRe, iCase)
                export_each_case(iWi, jAr, kRe, iCase)
  */
    int iFirst = 1;

    try {
      read_parameters("./Torsional_Rect_Fluid_2D.ini");
    }
    catch (IOException e) {
      System.out.println( e.getMessage() );
    }

    pre0_parameter(vnStEdW[0], vnStEdAR[0], vnStEdRe[0], vnStEdCase[0]);
    pre1_view(vWidth[vnStEdW[0]], vGeoRatio[vnStEdRe[0]]);
          pre2_geometry();
          pre3_selection();
          pre4_material();
          pre5_physics(vnStEdCase[0]);
          pre6_mesh();
```

```
        pre7_solution(vnStEdW[0], vnStEdAR[0], vnStEdRe[0], vnStEdCase[0]);
        post_processing(vnStEdW[0], vnStEdAR[0], vnStEdRe[0], vnStEdCase[0]);

        for (int iWi = vnStEdW[0]; iWi < vnStEdW[1]; iWi++) {
                for (int j = vnStEdAR[0]; j < vnStEdAR[1]; j++) {
                        for (int i = vnStEdCase[0]; i < vnStEdCase[1]; i++) {
//  i=1:  Case 1 Exact Velocity History at Inner Boundary, Coarse Mesh
//  i=2:  Case 2 Exact Velocity History at Inner Boundary,  Fine  Mesh
//  i=3:  Case 3 Approximated Velocity History at Inner Boundary, Coarse Mesh
//  i=4:  Case 4 Approximated Velocity History at Inner Boundary,  Fine  Mesh
                                for (int k = vnStEdRe[0]; k < vnStEdRe[1]; k++) {
                                        if (iFirst==1) {
                                                iFirst=0;
                                        } else {
                                                pre1_view(vWidth[iWi], vGeoRatio[k]);
                                                export_each_case(iWi, j, k, i);
                                        }
                                }
                        }
                }
        //t export_each_group(i, j, k);
        }
  }


  static void read_parameters(String path) throws IOException {
  /* Function: Read parameters from the ini file
     Called by: main()
     Call:      conver_data(s,n)
  */
    FileReader fr = new FileReader(path);
    BufferedReader textReader = new BufferedReader(fr);

    String[] textArray = textReader.readLine().split("%");
    String textPath = textArray[0].replaceAll(" *$","").replaceAll("^ *","");
    if (textPath.equals(".")) {
          stPath = new java.io.File(".").getCanonicalPath() + "/";
    } else {
          stPath = textPath + "/";
    }

    textArray = textReader.readLine().split("%");
    vWidth = textArray[0].replaceAll(" ","").split(",");

    textArray = textReader.readLine().split("%");
    vAspectRatio = textArray[0].replaceAll(" ","").split(",");

    textArray = textReader.readLine().split("%");
    vNumNode = textArray[0].replaceAll(" ","").split(",");

    textArray = textReader.readLine().split("%");
    vPara = textArray[0].replaceAll(" ","").split(",");

    textArray = textReader.readLine().split("%");
    vReynolds = textArray[0].replaceAll(" ","").split(",");
```

```
  textArray = textReader.readLine().split("%");
  vGeoRatio = textArray[0].replaceAll(" ","").split(",");

  textArray = textReader.readLine().split("%");
  textArray = textArray[0].replaceAll(" ","").split(",");
  vnStEdW = convert_data(textArray, vWidth.length);

  textArray = textReader.readLine().split("%");
  textArray = textArray[0].replaceAll(" ","").split(",");
  vnStEdAR = convert_data(textArray, vAspectRatio.length);

  textArray = textReader.readLine().split("%");
  textArray = textArray[0].replaceAll(" ","").split(",");
  vnStEdCase = convert_data(textArray, 5);
  if (vnStEdCase[0]==0) vnStEdCase[0] = 1;

  textArray = textReader.readLine().split("%");
  textArray = textArray[0].replaceAll(" ","").split(",");
  vnStEdRe = convert_data(textArray, vReynolds.length);

  textReader.close( );
}


static int[] convert_data(String[] s, int n) {
/* Function: Read parameters from the ini file
   Called by: read_parameters(path)
   Call:      None
*/
  int[] vn = new int [s.length];
  for (int i=0; i<s.length; i++) {
     vn[i] = Integer.parseInt(s[i]);
  }
  if (vn[0] < 0) vn[0] = 0;
  if (vn[1] < 0) vn[1] = n;
  if (vn[1] > n) vn[1] = n;
  return vn;
}


static void pre0_parameter(int iWi, int jAr, int kRe, int iCase) {
/* Function:  0. Nodes, Parameters and variables, Pre-Processing of Comsol Model
   Called by: main()
   Call:      None
*/
  if (iCase > 2) iCase = iCase - 2;
  model.modelPath(stPath);
  model.modelNode().create("mod1");       // Model and Definitions
  model.geom().create("geom1", 2);        // Geometry and Materials
  model.mesh().create("mesh1", "geom1");
  model.physics().create("spf", "CreepingFlow", "geom1");
  model.study().create("std1");
  model.study("std1").feature().create("time", "Transient");

  model.param().set("us_geo_w_c", vWidth[iWi] + " [um]", "Cantilever Width");
```

```
   model.param().set("us_geo_t_c",
Double.parseDouble(vWidth[iWi])*Double.parseDouble(vAspectRatio[jAr]) + " [um]",
"Cantilever Thickness");
   model.param().set("us_geo_w_f",
Double.parseDouble(vWidth[iWi])*Double.parseDouble(vGeoRatio[kRe]), "Fluid Width");
   model.param().set("us_geo_t_f", "us_geo_w_f", "Fluid Thickness");
   model.param().set("us_geo_w_rec", "(us_geo_w_f-us_geo_w_c)/2", "Fluid Width of the
rectangles at the corners");
   model.param().set("us_geo_t_rec", "(us_geo_t_f-us_geo_t_c)/2", "Fluid Thickness of
the rectangles at the corners");
   model.param().set("us_mat_f_rho", "1E3 [kg/m^3]", "Density of the fluid");
   model.param().set("us_mat_f_eta", "1E-3 [Pa*s]", "Dynamic Viscosity of the fluid");
   model.param().set("us_Re", vReynolds[kRe], "Reynolds Number");
   model.param().set("us_omega_ex",
"4*us_mat_f_eta*us_Re/us_mat_f_rho/us_geo_w_c^2", "Beam Exciting Angular
Frequency");
   model.param().set("us_freq_ex", "us_omega_ex/2/pi", "Beam Exciting Frequency");
   model.param().set("us_u_amp", "0.2[um]", "Beam Displacement Amplitude");
   model.param().set("us_v_amp", "us_omega_ex*us_u_amp", "Beam Velocity
Amplitude");
   model.param().set("us_mesh_hc_num",   Double.parseDouble(vPara[0])*iCase,
"Number of Elements along each horizontal center line");
   model.param().set("us_mesh_hc_ratio", vPara[1], "Ratio of Element sizes along each
horizontal center line");
   model.param().set("us_mesh_hs_num",   Double.parseDouble(vPara[2])*iCase,
"Number of Elements along each horizontal side line");
   model.param().set("us_mesh_hs_ratio", vPara[3], "Ratio of Element sizes along each
horizontal side line");
   model.param().set("us_mesh_vc_num",   Double.parseDouble(vNumNode[jAr])*iCase,
"Number of Elements along each vertical center line");
   model.param().set("us_mesh_vc_ratio", vPara[4], "Ratio of Element sizes along each
vertical center line");
   model.param().set("us_mesh_vs_num",   Double.parseDouble(vPara[5])*iCase,
"Number of Elements along each vertical side line");
   model.param().set("us_mesh_vs_ratio", vPara[6], "Ratio of Element sizes along each
vertical side line");
   model.param().set("us_t0", "0 [us]", "Start Time");
   model.param().set("us_num_period",    vPara[7], "Number of the periods");
   model.param().set("us_num_interval",  Double.parseDouble(vPara[8])*iCase, "Number
of the intervals in each period");
   model.param().set("us_tf", "us_num_period/us_freq_ex", "Stop Time");
   model.param().set("us_ts", "1/us_freq_ex/us_num_interval", "Time Step");

   model.variable().create("var1");
   model.variable("var1").set("uv_v1_tors_beam", "-
us_v_amp*cos(us_omega_ex*t)*2*y/sqrt(us_geo_w_c^2+us_geo_t_c^2)", "History of
beam velocity in lateral direction");
        model.variable("var1").set("uv_v2_tors_beam",
"us_v_amp*cos(us_omega_ex*t)*2*x/sqrt(us_geo_w_c^2+us_geo_t_c^2)", "History of
beam velocity in transverse direction");
   model.variable("var1").set("uv_v_tors_beam",
"us_v_amp*cos(us_omega_ex*t)*2*x/us_geo_w_c", "History of beam velocity in
transverse direction, ignore velocity in lateral direction");

   model.view().create("view2", "geom1");
   model.view("view2").name("View 2 - Center");
```

```
  model.view("view2").set("locked", "on");
  model.view("view2").set("showlabels", "off");

  model.view().create("view3", "geom1");
  model.view("view3").name("View 3 - All");
  model.view("view3").set("locked", "on");
  model.view("view3").set("showlabels", "off");
}


static void pre1_view(String s_Width, String s_GeoRatio) {
/* Function:  1. views, Pre-Processing of Comsol Model
   Called by: main()
   Call:      None
*/
  double sMax = Double.parseDouble(s_Width) * 2;
  model.view("view2").axis().set("xmin", -sMax);
  model.view("view2").axis().set("xmax",  sMax);
  model.view("view2").axis().set("ymin", -sMax);
  model.view("view2").axis().set("ymax",  sMax);

  sMax = sMax * Double.parseDouble(s_GeoRatio) / 4;
  model.view("view3").axis().set("xmin", -sMax);
  model.view("view3").axis().set("xmax",  sMax);
  model.view("view3").axis().set("ymin", -sMax);
  model.view("view3").axis().set("ymax",  sMax);
}


static void pre2_geometry() {
/* Function:  2. Geometry, Pre-Processing of Comsol Model
   Called by: main()
   Call:      None
*/
  model.geom("geom1").lengthUnit("\u00b5m");
  model.geom("geom1").feature().create("r1", "Rectangle");
  model.geom("geom1").feature("r1").setIndex("size", "us_geo_w_rec", 0);
  model.geom("geom1").feature("r1").setIndex("size", "us_geo_t_rec", 1);
  model.geom("geom1").feature("r1").setIndex("pos", "-us_geo_w_f/2", 0);
  model.geom("geom1").feature("r1").setIndex("pos", "us_geo_t_c/2", 1);

  model.geom("geom1").feature().create("r2", "Rectangle");
  model.geom("geom1").feature("r2").setIndex("size", "us_geo_w_c", 0);
  model.geom("geom1").feature("r2").setIndex("size", "us_geo_t_rec", 1);
  model.geom("geom1").feature("r2").setIndex("pos", "-us_geo_w_c/2", 0);
  model.geom("geom1").feature("r2").setIndex("pos", "us_geo_t_c/2", 1);

  model.geom("geom1").feature().create("r3", "Rectangle");
  model.geom("geom1").feature("r3").setIndex("size", "us_geo_w_rec", 0);
  model.geom("geom1").feature("r3").setIndex("size", "us_geo_t_rec", 1);
  model.geom("geom1").feature("r3").setIndex("pos", "us_geo_w_c/2", 0);
  model.geom("geom1").feature("r3").setIndex("pos", "us_geo_t_c/2", 1);

  model.geom("geom1").feature().create("r4", "Rectangle");
  model.geom("geom1").feature("r4").setIndex("size", "us_geo_w_rec", 0);
  model.geom("geom1").feature("r4").setIndex("size", "us_geo_t_c", 1);
```

```
  model.geom("geom1").feature("r4").setIndex("pos", "-us_geo_w_f/2", 0);
  model.geom("geom1").feature("r4").setIndex("pos", "-us_geo_t_c/2", 1);

  model.geom("geom1").feature().create("r5", "Rectangle");
  model.geom("geom1").feature("r5").setIndex("size", "us_geo_w_rec", 0);
  model.geom("geom1").feature("r5").setIndex("size", "us_geo_t_c", 1);
  model.geom("geom1").feature("r5").setIndex("pos", "us_geo_w_c/2", 0);
  model.geom("geom1").feature("r5").setIndex("pos", "-us_geo_t_c/2", 1);

  model.geom("geom1").feature().create("r6", "Rectangle");
  model.geom("geom1").feature("r6").setIndex("size", "us_geo_w_rec", 0);
  model.geom("geom1").feature("r6").setIndex("size", "us_geo_t_rec", 1);
  model.geom("geom1").feature("r6").setIndex("pos", "-us_geo_w_f/2", 0);
  model.geom("geom1").feature("r6").setIndex("pos", "-us_geo_t_f/2", 1);

  model.geom("geom1").feature().create("r7", "Rectangle");
  model.geom("geom1").feature("r7").setIndex("size", "us_geo_w_c", 0);
  model.geom("geom1").feature("r7").setIndex("size", "us_geo_t_rec", 1);
  model.geom("geom1").feature("r7").setIndex("pos", "-us_geo_w_c/2", 0);
  model.geom("geom1").feature("r7").setIndex("pos", "-us_geo_t_f/2", 1);

  model.geom("geom1").feature().create("r8", "Rectangle");
  model.geom("geom1").feature("r8").setIndex("size", "us_geo_w_rec", 0);
  model.geom("geom1").feature("r8").setIndex("size", "us_geo_t_rec", 1);
  model.geom("geom1").feature("r8").setIndex("pos", "us_geo_w_c/2", 0);
  model.geom("geom1").feature("r8").setIndex("pos", "-us_geo_t_f/2", 1);

  model.geom("geom1").run();
}


static void pre3_selection() {
/* Function:  3. Geometry Selections, Pre-Processing of Comsol Model
   Called by: main()
   Call:      None
*/
  model.selection().create("sel1");
  model.selection("sel1").geom(1);
  model.selection("sel1").name("Selection 1B- Inner Interface");
  model.selection("sel1").set(new int[]{10, 11, 13, 17});

  model.selection().create("sel2");
  model.selection("sel2").geom(1);
  model.selection("sel2").name("Selection 2B - Outer Boundary");
  model.selection("sel2").set(new int[]{1, 2, 3, 5, 7, 9, 14, 16, 21, 22, 23, 24});

  model.selection().create("sel3");
  model.selection("sel3").geom(1);
  model.selection("sel3").name("Selection 3B - Horizontal Left Lines");
  model.selection("sel3").set(new int[]{2, 4, 6, 7});

  model.selection().create("sel4");
  model.selection("sel4").name("Selection 4B - Horizontal Center Lines");
  model.selection("sel4").geom(1);
  model.selection("sel4").set(new int[]{9, 11, 13, 14});
```

```
    model.selection().create("sel5");
    model.selection("sel5").name("Selection 5B - Horizontal Right Lines");
    model.selection("sel5").geom(1);
    model.selection("sel5").set(new int[]{16, 18, 20, 21});

    model.selection().create("sel6");
    model.selection("sel6").name("Selection 6B - Vertical Top Lines");
    model.selection("sel6").geom(1);
    model.selection("sel6").set(new int[]{5, 12, 19, 24});

    model.selection().create("sel7");
    model.selection("sel7").name("Selection 7B - Vertical Center Lines");
    model.selection("sel7").geom(1);
    model.selection("sel7").set(new int[]{3, 10, 17, 23});

    model.selection().create("sel8");
    model.selection("sel8").name("Selection 8B - Vertical Bottom Lines");
    model.selection("sel8").geom(1);
    model.selection("sel8").set(new int[]{1, 8, 15, 22});
  }


  static void pre4_material() {
  /* Function:  4. Material, Pre-Processing of Comsol Model
     Called by: main()
     Call:      None
  */
    model.material().create("mat1");
    model.material("mat1").name("Water");
    model.material("mat1").materialModel("def").set("density", new
String[]{"us_mat_f_rho"});
    model.material("mat1").materialModel("def").set("dynamicviscosity", new
String[]{"us_mat_f_eta"});
  }


  static void pre5_physics(int iCase) {
  /* Function:  5. Boundary Conditions and Loads, Pre-Processing of Comsol Model
     Called by: main()
     Call:      None
  */
    model.physics("spf").prop("CompressibilityProperty").set("Compressibility", 1,
"Incompressible");
    model.physics("spf").feature().create("wall2", "Wall", 1);
    model.physics("spf").feature("wall2").name("Inner Interface");
    model.physics("spf").feature("wall2").selection().named("sel1");
    model.physics("spf").feature("wall2").set("BoundaryCondition", 1, "MovingWall");
    if (iCase < 3) {
          model.physics("spf").feature("wall2").set("uwall", new
String[]{"uv_v1_tors_beam", "uv_v2_tors_beam", "0"});
    } else {
          model.physics("spf").feature("wall2").set("uwall", new String[]{"0",
"uv_v_tors_beam", "0"});
    }

    model.physics("spf").feature().create("out1", "Outlet", 1);
```

```
      model.physics("spf").feature("out1").name("Outer Boundary");
  model.physics("spf").feature("out1").selection().named("sel2");
 }


 static void pre6_mesh() {
 /* Function:  6. Meshes, Pre-Processing of Comsol Model
   Called by: main()
   Call:      None
 */
  model.mesh("mesh1").feature().create("map1", "Map");
  model.mesh("mesh1").feature("map1").selection().geom("geom1");

  model.mesh("mesh1").feature("map1").feature().create("dis1", "Distribution");
  model.mesh("mesh1").feature("map1").feature("dis1").selection().named("sel3");
  model.mesh("mesh1").feature("map1").feature("dis1").set("type", "predefined");
  model.mesh("mesh1").feature("map1").feature("dis1").set("elemcount",
"us_mesh_hs_num");
  model.mesh("mesh1").feature("map1").feature("dis1").set("elemratio",
"us_mesh_hs_ratio");

  model.mesh("mesh1").feature("map1").feature().create("dis2", "Distribution");
  model.mesh("mesh1").feature("map1").feature("dis2").selection().named("sel4");
  model.mesh("mesh1").feature("map1").feature("dis2").set("type", "predefined");
  model.mesh("mesh1").feature("map1").feature("dis2").set("elemcount",
"us_mesh_hc_num");
  model.mesh("mesh1").feature("map1").feature("dis2").set("elemratio",
"us_mesh_hc_ratio");
  model.mesh("mesh1").feature("map1").feature("dis2").set("symmetric", "on");

  model.mesh("mesh1").feature("map1").feature().create("dis3", "Distribution");
  model.mesh("mesh1").feature("map1").feature("dis3").selection().named("sel5");
  model.mesh("mesh1").feature("map1").feature("dis3").set("type", "predefined");
  model.mesh("mesh1").feature("map1").feature("dis3").set("elemcount",
"us_mesh_hs_num");
  model.mesh("mesh1").feature("map1").feature("dis3").set("elemratio",
"us_mesh_hs_ratio");
  model.mesh("mesh1").feature("map1").feature("dis3").set("reverse", "on");

  model.mesh("mesh1").feature("map1").feature().create("dis4", "Distribution");
  model.mesh("mesh1").feature("map1").feature("dis4").selection().named("sel6");
  model.mesh("mesh1").feature("map1").feature("dis4").set("type", "predefined");
  model.mesh("mesh1").feature("map1").feature("dis4").set("elemcount",
"us_mesh_vs_num");
  model.mesh("mesh1").feature("map1").feature("dis4").set("elemratio",
"us_mesh_vs_ratio");

  model.mesh("mesh1").feature("map1").feature().create("dis5", "Distribution");
  model.mesh("mesh1").feature("map1").feature("dis5").selection().named("sel7");
  model.mesh("mesh1").feature("map1").feature("dis5").set("type", "predefined");
  model.mesh("mesh1").feature("map1").feature("dis5").set("elemcount",
"us_mesh_vc_num");
  model.mesh("mesh1").feature("map1").feature("dis5").set("elemratio",
"us_mesh_vc_ratio");
  model.mesh("mesh1").feature("map1").feature("dis5").set("symmetric", "on");
```

```
  model.mesh("mesh1").feature("map1").feature().create("dis6", "Distribution");
  model.mesh("mesh1").feature("map1").feature("dis6").selection().named("sel8");
  model.mesh("mesh1").feature("map1").feature("dis6").set("type", "predefined");
  model.mesh("mesh1").feature("map1").feature("dis6").set("elemcount",
"us_mesh_vs_num");
  model.mesh("mesh1").feature("map1").feature("dis6").set("elemratio",
"us_mesh_vs_ratio");
  model.mesh("mesh1").feature("map1").feature("dis6").set("reverse", "on");

  model.mesh("mesh1").run();
}


 static void pre7_solution(int iWi, int jAr, int kRe, int iCase) {
 /* Function:  7. Solution Settings, Pre-Processing of Comsol Model
   Called by: main()
   Call:      None
 */
  model.study("std1").feature("time").set("tlist", "range(us_t0,us_ts,us_tf)");

     String stSolution = "sol_W" + iWi + "_Ar" + jAr + "_Case" + iCase + "_Re" + kRe;
  model.sol().create(stSolution);
  model.sol(stSolution).study("std1");
  model.sol(stSolution).feature().create("st1", "StudyStep");
  model.sol(stSolution).feature("st1").set("study", "std1");
  model.sol(stSolution).feature("st1").set("studystep", "time");
  model.sol(stSolution).feature().create("v1", "Variables");
  model.sol(stSolution).feature().create("t1", "Time");
  model.sol(stSolution).feature("t1").set("tlist", "range(us_t0,us_ts,us_tf)");
  model.sol(stSolution).feature("t1").set("plot", "off");
  model.sol(stSolution).feature("t1").set("plotfreq", "tout");
  model.sol(stSolution).feature("t1").set("probesel", "all");
  model.sol(stSolution).feature("t1").set("probes", new String[]{});
  model.sol(stSolution).feature("t1").set("probefreq", "tsteps");
  model.sol(stSolution).feature("t1").set("estrat", "exclude");
  model.sol(stSolution).feature("t1").set("maxorder", 2);
  model.sol(stSolution).feature("t1").set("control", "time");
  model.sol(stSolution).feature("t1").feature().create("fc1", "FullyCoupled");
  model.sol(stSolution).feature("t1").feature("fc1").set("jtech", "once");
  model.sol(stSolution).feature("t1").feature("fc1").set("maxiter", 5);
  model.sol(stSolution).feature("t1").feature().create("d1", "Direct");
  model.sol(stSolution).feature("t1").feature("d1").set("linsolver", "pardiso");
  model.sol(stSolution).feature("t1").feature("fc1").set("linsolver", "d1");
  model.sol(stSolution).feature("t1").feature("fc1").set("jtech", "once");
  model.sol(stSolution).feature("t1").feature("fc1").set("maxiter", 5);
  model.sol(stSolution).feature("t1").feature().remove("fcDef");
  model.sol(stSolution).attach("std1");
  model.sol(stSolution).runAll();
 }



 static void post_processing(int iWi, int jAr, int kRe, int iCase) {
 /* Function:  Post-Processing of Comsol Model
   Called by: main()
   Call:      None
```

```
  */
        String stFpre = "Torsional_Rect_Fluid_2D-W" + iWi + "=" + vWidth[iWi] + "_Ar"
+ jAr + "=" + vAspectRatio[jAr] + "_Case" + iCase + "_Re" + kRe + "=" + vReynolds[kRe]
+ "-";

   model.result().create("pg1", "PlotGroup2D");
   model.result("pg1").feature().create("surf1", "Surface");
   model.result("pg1").feature("surf1").set("expr", "p");
   model.result("pg1").feature("surf1").set("unit", "kPa");
   model.result("pg1").feature().create("str1", "Streamline");
   model.result("pg1").feature().create("arws1", "ArrowSurface");
   model.result("pg1").set("window", "graphics");
   model.result("pg1").set("windowtitle", "Graphics");
   model.result("pg1").set("view", "view3");
   model.result("pg1").run();

   model.result("pg1").set("view", "view2");
   model.result().export().create("anim1", "Animation");
   model.result().export("anim1").set("giffilename", stPath + stFpre + ".gif");

   model.result().table().create("tbl1", "Table");
   model.result().table("tbl1").name("Table 1 - Normalized Torque per unit length");
   model.result().table("tbl1").comments("Line Integration 1 (x*spf.T_stressy -
y*spf.T_stressx)/(pi*us_geo_w_c*us_v_amp*us_mat_f_eta*us_Re)");

   model.result().numerical().create("gev1", "EvalGlobal");
   model.result().numerical("gev1").set("expr", "t*us_num_interval*us_freq_ex");
   model.result().numerical("gev1").set("table", "tbl1");
   model.result().numerical("gev1").setResult();
   model.result().table("tbl1").removeColumn(0);

   model.result().numerical().create("int1", "IntLine");
   model.result().numerical("int1").selection().named("sel1");
   model.result().numerical("int1").set("expr", "(x*spf.T_stressy -
y*spf.T_stressx)/(pi*us_geo_w_c*us_v_amp*us_mat_f_eta*us_Re)");
   model.result().numerical("int1").set("table", "tbl1");
   model.result().numerical("int1").appendResult();
   model.result().table("tbl1").save(stPath + stFpre + "Normalized Torque per Unit
Length.txt");

   model.result().create("pg2", "PlotGroup1D");
   model.result("pg2").set("window", "window1");
   model.result("pg2").set("windowtitle", "Normalized Velocity and Torque per Unit
Length");
   model.result("pg2").set("titleactive", "on");
   model.result("pg2").set("title", "Normalized Velocity and Torque per Unit Length");
   model.result("pg2").set("ylabelactive", "on");
   model.result("pg2").set("ylabel", "Normalized Velocity and Torque per Unit Length");

   model.result("pg2").feature().create("glob1", "Global");
   model.result("pg2").feature("glob1").set("xdata", "expr");
   model.result("pg2").feature("glob1").set("xdataexpr", "t");
   model.result("pg2").feature("glob1").set("xdataunit", "\u00b5s");
   model.result("pg2").feature("glob1").set("legendmethod", "manual");
   model.result("pg2").feature("glob1").setIndex("expr", "cos(us_omega_ex*t)", 0);
   model.result("pg2").feature("glob1").setIndex("legends", "cos(us_omega_ex*t)", 0);
```

```
   model.result("pg2").feature().create("tblp1", "Table");
   model.result("pg2").feature("tblp1").set("xaxisdata", "1");
   model.result("pg2").feature("tblp1").set("legend", "on");
   model.result("pg2").feature("tblp1").set("legendmethod", "manual");
   model.result("pg2").feature("tblp1").setIndex("legends", "Line Integral
(spf.sr/2/pi/us_v_amp/us_Re)", 0);

   model.result("pg2").run();

   model.result().create("pg3", "PlotGroup1D");
   model.result("pg3").feature().create("lngr1", "LineGraph");
   model.result("pg3").feature("lngr1").selection().named("sel2");
   model.result("pg3").feature("lngr1").set("expr", "spf.U/us_v_amp");
   model.result("pg3").run();

   model.result().export().create("plot1", "pg3", "lngr1", "Plot");
   model.result().export("plot1").set("filename",  stPath + stFpre + "Speed Ratio at Outer
Boundary.txt");
   model.result().export("plot1").run();

  }


  static void export_each_case(int iWi, int jAr, int kRe, int iCase) {
  /* Function:  Export Comsl Results for Each Case
     Called by: main()
     Call:      None
  */
         String stFpre = "Torsional_Rect_Fluid_2D-W" + iWi + "=" + vWidth[iWi] + "_Ar"
+ jAr + "=" + vAspectRatio[jAr] + "_Case" + iCase + "_Re" + kRe + "=" + vReynolds[kRe]
+ "-";
        String stSolution = "sol_W" + iWi + "_Ar" + jAr + "_Case" + iCase + "_Re" + kRe;
         if (iCase > 2) iCase = iCase - 2;

   model.param().set("us_geo_w_c", vWidth[iWi] + " [um]", "Cantilever Raduis");
   model.param().set("us_geo_t_c",
Double.parseDouble(vWidth[iWi])*Double.parseDouble(vAspectRatio[jAr]) + " [um]",
"Cantilever Thickness");
   model.param().set("us_geo_w_f",
Double.parseDouble(vWidth[iWi])*Double.parseDouble(vGeoRatio[kRe]), "Fluid Width");
   model.param().set("us_Re", vReynolds[kRe], "Reynolds Number");
   model.param().set("us_mesh_hc_num",   Double.parseDouble(vPara[0])*iCase,
"Number of Elements along each horizontal center line");
   model.param().set("us_mesh_hs_num",   Double.parseDouble(vPara[2])*iCase,
"Number of Elements along each horizontal side line");
   model.param().set("us_mesh_vc_num",   Double.parseDouble(vNumNode[jAr])*iCase,
"Number of Elements along each vertical center line");
   model.param().set("us_mesh_vs_num",   Double.parseDouble(vPara[5])*iCase,
"Number of Elements along each vertical side line");
   model.param().set("us_num_interval",  Double.parseDouble(vPara[8])*iCase, "Number
of the intervals in each period");
   model.mesh("mesh1").run();

   model.sol().create(stSolution);
   model.sol(stSolution).study("std1");
```

```
    model.sol(stSolution).feature().create("st1", "StudyStep");
    model.sol(stSolution).feature("st1").set("study", "std1");
    model.sol(stSolution).feature("st1").set("studystep", "time");
    model.sol(stSolution).feature().create("v1", "Variables");
    model.sol(stSolution).feature().create("t1", "Time");
    model.sol(stSolution).feature("t1").set("tlist", "range(us_t0,us_ts,us_tf)");
    model.sol(stSolution).feature("t1").set("plot", "off");
    model.sol(stSolution).feature("t1").set("plotfreq", "tout");
    model.sol(stSolution).feature("t1").set("probesel", "all");
    model.sol(stSolution).feature("t1").set("probes", new String[]{});
    model.sol(stSolution).feature("t1").set("probefreq", "tsteps");
    model.sol(stSolution).feature("t1").set("estrat", "exclude");
    model.sol(stSolution).feature("t1").set("maxorder", 2);
    model.sol(stSolution).feature("t1").set("control", "time");
    model.sol(stSolution).feature("t1").feature().create("fc1", "FullyCoupled");
    model.sol(stSolution).feature("t1").feature("fc1").set("jtech", "once");
    model.sol(stSolution).feature("t1").feature("fc1").set("maxiter", 5);
    model.sol(stSolution).feature("t1").feature().create("d1", "Direct");
    model.sol(stSolution).feature("t1").feature("d1").set("linsolver", "pardiso");
    model.sol(stSolution).feature("t1").feature("fc1").set("linsolver", "d1");
    model.sol(stSolution).feature("t1").feature("fc1").set("jtech", "once");
    model.sol(stSolution).feature("t1").feature("fc1").set("maxiter", 5);
    model.sol(stSolution).feature("t1").feature().remove("fcDef");
    model.sol(stSolution).attach("std1");
    model.sol(stSolution).runAll();

    model.result().dataset("dset1").set("solution", stSolution);
          model.result("pg1").set("window", "graphics");
    model.result("pg1").set("windowtitle", "Graphics");
    model.result("pg1").set("view", "view3");
    model.result("pg1").run();

    model.result("pg1").set("view", "view2");
    model.result().export("anim1").set("giffilename", stPath + stFpre + ".gif");

    model.result().numerical("gev1").setResult();
    model.result().table("tbl1").removeColumn(0);
    model.result().numerical("int1").selection().named("sel1");
    model.result().numerical("int1").appendResult();
    model.result().table("tbl1").save(stPath + stFpre + "Normalized Torque per Unit
Length.txt");

    model.result("pg3").feature("lngr1").selection().named("sel2");
    model.result().export("plot1").set("filename",  stPath + stFpre + "Speed Ratio at Outer
Boundary.txt");
    model.result().export("plot1").run();

  }

}
```

APPENDIX B MATLAB PROGRAM USED TO EXTRACT THE MAGNITUDE, PHASE, REAL AND IMAGINARY PARTS OF THE HYDRODYNAMIC FUNCTION

```
function HDF_Plots()
%% Extract Hydrodynamic Function from COMSOL Numerical Results
%% Called by: postprocess.m
%% Call: getHDF_Ribbon(), getHDF_tors_rect_comsol(), plotEachCase(),
%%       plotEachAR(), plotHDF()

% Names used to identify results files
sPath = 'Rectangular_Torsional_2D.zip\'; % Path of the root folder of
result files
sAnalysis = 'Torsional_Rect_Fluid_2D-W1=20'; % Initial part of the
result filename
mVar = {'Normalized Torque per Unit Length' 'Speed Ratio at Outer
Boundary'};

% Parameters: Aspect Ratio h/b, Reynolds number Re, ...
vAspectRatio = [0.001 0.002 0.005 0.01 0.02 0.05 0.1 0.2 0.3 0.5 1];
vReynolds = [1 1.778 3.162 5.623 10 17.78 31.62 56.23 100 177.8
316.2 ...
               562.3 1000 1778 3162 5623 10000 17780 31620];
vInterval = [60 120]; % vInterval = [60 120 60 120]; % Number of
intervals in each period of the response
nCase = length(vInterval); % Number of Cases per h/b per Re
nPeriod = 3; % Number of period of the response

mHDF_Sader = getHDF_Ribbon('Torsional Rectangular', vReynolds');
m5HDF = zeros(length(vAspectRatio), nCase, length(vReynolds), 5, 8);
for i = 0:length(vAspectRatio)-1
    for j = 1:nCase
        nLast = (nPeriod-1)*vInterval(j) + 1;
        for k = 0:length(vReynolds)-1
            disp(['  AspectRatio' num2str(i) ' = '
num2str(vAspectRatio(i+1)) ...
                  '    CaseNo. ' num2str(j) ...
                  '    Reynolds#' num2str(k) ' = '
num2str(vReynolds(k+1))]);
            sfname = ['Ar' num2str(i) '=' num2str(vAspectRatio(i+1)) ...
                      '\' sAnalysis '_Ar' num2str(i) '='
num2str(vAspectRatio(i+1)) ...
                      '_Case' num2str(j) '_Re' num2str(k) '='
num2str(vReynolds(k+1)) '-'];
            mTorque = dlmread([sPath sfname mVar{1} '.txt'], '', 5, 0);
            mTorque(:,1) = (0:vInterval(j)*nPeriod)';
            mSpeed = dlmread([sPath sfname mVar{2} '.txt'], '',
1729*120+8, 0);
            m5HDF(i+1,j,k+1,:,:)  = getHDF_tors_rect_comsol(vInterval(j),
mTorque(nLast:end,2));
            mHDF = shiftdim(m5HDF(i+1,j,k+1,:,:),3);
            figure(1); % Torque per unit length, Speeds on the outer
boundaries
```

```
            plotEachRe(nLast, mVar, vAspectRatio(i+1), j, ...
                          vReynolds(k+1), mTorque, mHDF, mSpeed);
            set(gcf, 'PaperPosition', [0.25 2.5 13.33 10.0]);
            print('-dtiff', ['Results\Ar' num2str(i) '='
num2str(vAspectRatio(i+1)) ...
                    '\EachRe-Ar' num2str(i) '='
num2str(vAspectRatio(i+1)) ...
                    '_Case' num2str(j) '_Re' num2str(k) '='
num2str(vReynolds(k+1)) '.tif']);
        end
        m3HDF= shiftdim(m5HDF(i+1,j,:,:,:),2);
        figure(2); % Magnitude, Phase, Real, Imag of Hydrodynamic
Functions for each case
        plotEachCase(vAspectRatio(i+1), j, vReynolds, m3HDF, vReynolds,
mHDF_Sader);
        set(gcf, 'PaperPosition', [0.25 2.5 13.33 10.0]);
        print('-dtiff', ['Results\EachCase-Ar' num2str(i) '='
num2str(vAspectRatio(i+1)) '_Case' num2str(j) '.tif']);
    end
    m3HDF= shiftdim(m5HDF(i+1,:,:,:,4),1);
    figure(3); % Magnitude, Phase, Real, Imag of Hydrodynamic Functions
for each aspect ratio.
    plotEachAR(nCase, vAspectRatio(i+1), vReynolds, m3HDF, vReynolds,
mHDF_Sader);
    set(gcf, 'PaperPosition', [0.25 2.5 13.33 10.0]);
    print('-dtiff', ['Results\EachAr-Ar' num2str(i) '='
num2str(vAspectRatio(i+1)) '.tif']);
end
m3HDF = squeeze(m5HDF(:,2,:,:,4))
mHDF1Mag  = m3HDF(:,:,1);  mHDF2Phase = m3HDF(:,:,2);
mHDF3Real = m3HDF(:,:,3);  mHDF4Imag  = m3HDF(:,:,4);  mHDF5Err =
m3HDF(:,:,5);
save('postprocess11_mHDF.mat', 'vAspectRatio', 'vReynolds',
'mHDF_Sader', ...
     'mHDF1Mag', 'mHDF2Phase', 'mHDF3Real', 'mHDF4Imag', 'mHDF5Err');
save('postprocess12_m3HDF_m5HDF.mat', 'vAspectRatio', 'vReynolds',
'm3HDF', 'm5HDF');

figure(4); % Hydrodynamic Functions 2D
plotHDF(vAspectRatio, vReynolds, m3HDF, vReynolds, mHDF_Sader);
set(gcf, 'PaperPosition', [0.25 2.5 13.33 10.0]);
print('-dtiff', ['Results\All Hydrodynamic Functions - 2D.tif']);

figure(5);  % Hydrodynamic Functions 3D Mesh
mColor = 10*ones(length(vAspectRatio), length(vReynolds));
subplot(2,2,1); mesh(log10(vReynolds), log10(vAspectRatio),
log10(m3HDF(:,:,1)), -mColor);
hold on; mesh(log10(vReynolds), log10(vAspectRatio),
kron(log10(mHDF_Sader(:,1)'), ones(length(vAspectRatio),1)), mColor);
xlabel('log(Re)'); ylabel('log(h/b)'); zlabel('Magnitude, Hydrodynamic
Function [log scale]');
legend('h/b\neq0', 'h/b=0 (Sader)', 'Location', 'Best');
subplot(2,2,2); mesh(log10(vReynolds), log10(vAspectRatio),
log10(m3HDF(:,:,3)), -mColor);
hold on; mesh(log10(vReynolds), log10(vAspectRatio),
kron(log10(mHDF_Sader(:,3)'), ones(length(vAspectRatio),1)), mColor);
```

```
xlabel('log(Re)'); ylabel('log(h/b)'); zlabel('Real, Hydrodynamic
Function [log scale]');
legend('h/b\neq0', 'h/b=0 (Sader)', 'Location', 'Best');
subplot(2,2,3); mesh(log10(vReynolds), log10(vAspectRatio),
log10(m3HDF(:,:,2)), -mColor);
hold on; mesh(log10(vReynolds), log10(vAspectRatio),
kron(log10(mHDF_Sader(:,2)'), ones(length(vAspectRatio),1)), mColor);
xlabel('log(Re)'); ylabel('log(h/b)'); zlabel('Phase, Hydrodynamic
Function [log scale]');
legend('h/b\neq0', 'h/b=0 (Sader)', 'Location', 'Best');
subplot(2,2,4); mesh(log10(vReynolds), log10(vAspectRatio),
log10(m3HDF(:,:,4)), -mColor);
hold on; mesh(log10(vReynolds), log10(vAspectRatio),
kron(log10(mHDF_Sader(:,4)'), ones(length(vAspectRatio),1)), mColor);
xlabel('log(Re)'); ylabel('log(h/b)'); zlabel('Imaginary, Hydrodynamic
Function [log scale]');
legend('h/b\neq0', 'h/b=0 (Sader)', 'Location', 'Best');
set(gcf, 'PaperPosition', [0.25 2.5 13.33 10.0]);
print('-dtiff', ['Results\All Hydrodynamic Functions - 3D - Mesh.tif']);

figure(6);  % Hydrodynamic Functions 3D Surf
subplot(2,2,1); surf(log10(vReynolds), log10(vAspectRatio),
log10(m3HDF(:,:,1)), -mColor);
hold on; surf(log10(vReynolds), log10(vAspectRatio),
kron(log10(mHDF_Sader(:,1)'), ones(length(vAspectRatio),1)), mColor);
xlabel('log(Re)'); ylabel('log(h/b)'); zlabel('Magnitude, Hydrodynamic
Function [log scale]');
legend('h/b\neq0', 'h/b=0 (Sader)', 'Location', 'Best');
subplot(2,2,2); surf(log10(vReynolds), log10(vAspectRatio),
log10(m3HDF(:,:,3)), -mColor);
hold on; surf(log10(vReynolds), log10(vAspectRatio),
kron(log10(mHDF_Sader(:,3)'), ones(length(vAspectRatio),1)), mColor);
xlabel('log(Re)'); ylabel('log(h/b)'); zlabel('Real, Hydrodynamic
Function [log scale]');
legend('h/b\neq0', 'h/b=0 (Sader)', 'Location', 'Best');
subplot(2,2,3); surf(log10(vReynolds), log10(vAspectRatio),
log10(m3HDF(:,:,2)), -mColor);
hold on; surf(log10(vReynolds), log10(vAspectRatio),
kron(log10(mHDF_Sader(:,2)'), ones(length(vAspectRatio),1)), mColor);
xlabel('log(Re)'); ylabel('log(h/b)'); zlabel('Phase, Hydrodynamic
Function [log scale]');
legend('h/b\neq0', 'h/b=0 (Sader)', 'Location', 'Best');
subplot(2,2,4); surf(log10(vReynolds), log10(vAspectRatio),
log10(m3HDF(:,:,4)), -mColor);
hold on; surf(log10(vReynolds), log10(vAspectRatio),
kron(log10(mHDF_Sader(:,4)'), ones(length(vAspectRatio),1)), mColor);
xlabel('log(Re)'); ylabel('log(h/b)'); zlabel('Imaginary, Hydrodynamic
Function [log scale]');
legend('h/b\neq0', 'h/b=0 (Sader)', 'Location', 'Best');
set(gcf, 'PaperPosition', [0.25 2.5 13.33 10.0]);
print('-dtiff', ['Results\All Hydrodynamic Functions - 3D - Surf.tif']);


function m_HDF = getHDF_Ribbon(str_Method, v_Reynolds)
%% Calculate Hydrodynamic Function for Microcantilevers with negligible
thickness
```

```
%% str_Method  string variable, Name or Type of Expressions or Methods
%% v_Reynolds  vector variable, Reynolds Number
%% Called by: getHDF_Thick(), Freq_Q_Torsional(), HDF_Plots()
%% m_HDF        matrix variable, Hydrodynamic Function (Magnitude, Phase,
Real part and Imaginary Part)
%%             at different Reynolds Numbers
switch str_Method
    case 'Transverse Circular' % [L. Rosenhead, Laminar Boundary Layers
(Clarendon, Oxford, 1963)]
        vt = sqrt(1j*v_Reynolds);
        vGamma_circ = 1 + 4*1j*besselk(1, -1j*vt) ./ vt ./ besselk(0, -
1j*vt);
        vreal = real(vGamma_circ);
        vimag = imag(vGamma_circ);

    case 'Transverse Rectangular' % [Sader 1998 JAP]
        vt = sqrt(1j*v_Reynolds);
        vGamma_circ = 1 + 4*1j*besselk(1, -1j*vt) ./ vt ./ besselk(0, -
1j*vt);
        vtau = log10(v_Reynolds);
        mtau = [vtau vtau.^2 vtau.^3 vtau.^4 vtau.^5 vtau.^6];
        vPara_r1 = [-0.48274; 0.46842; -0.12886; 0.044055; -0.0035117;
0.00069085];
        vPara_r2 = [-0.56964; 0.48690; -0.13444; 0.045155; -0.0035862;
0.00069085];
        vPara_i1 = [-0.029256; 0.016294; -0.00010961; 0.000064577; -
0.000044510; 0];
        vPara_i2 = [-0.59702; 0.55182; -0.18357; 0.079156; -0.014369;
0.0028361];
        vOmega_r = ( 0.91324  + mtau * vPara_r1) ./ (1 + mtau *
vPara_r2);
        vOmega_i = (-0.024134 + mtau * vPara_i1) ./ (1 + mtau *
vPara_i2);
        vGamma_rect = vGamma_circ .* ( vOmega_r + 1j*vOmega_i);
        vreal = real(vGamma_rect);
        vimag = imag(vGamma_rect);

    case 'Torsional Rectangular' % [Green+Sader 2002 JAP]
        mtau = ones(length(v_Reynolds),7);    vtau = log10(v_Reynolds);
        for i=1:6
            mtau(:,i+1)=mtau(:,i) .* vtau;
        end
        v1 = mtau * [4.17950 -0.25269 2.88308 -0.08680 0.33837 0.03318
0.01884]';
        v2 = mtau * [1       -2.27659 2.10179 -0.11365 0.34989 0.03779
0.01884]';
        vreal = (5*v_Reynolds - 15*log(v_Reynolds) + 8)/80 ./
(v_Reynolds + 1) .* v1 ./ v2;
        v1 = mtau * [0.82494 -0.67701 0.41150 -0.16748 0.04897 -0.01107
0.00148]';
        v2 = mtau * [1       -0.72962 0.40663 -0.16517 0.04907 -0.01110
0.00148]';
        vimag = 0.41 ./ sqrt(v_Reynolds) + 1 ./ v_Reynolds .* v1 ./ v2;
end
vmag = sqrt(vreal .* vreal + vimag .* vimag);
vphase = atan(vimag ./ vreal) * 180 / pi;
```

```
m_HDF = [vmag vphase vreal vimag];


function m_HDF = getHDF_tors_rect_comsol(n_Interval, v_Var)
%% Extract Hydrodynamic Function for Torsionally Vibrating Rectangular
Microcantilevers
%% from COMSOL Numerical Results
%% n_Interval    integer variable, Number of intervals in each period
%% v_Var         vector variable, Normalized Torque per unit length
%% Called by: HDF_Plots()
%% m_HDF         matrix variable, Hydrodynamic Function (Magnitude,
Phase, Real, Imaginary, Error)
%%               for 8 different methods to retrieve the information
m_HDF = zeros(5,8); [sMax, nMax] = max(v_Var); [sMin, nMin] =
min(v_Var);

% Compare Last two Zeros
[sTemp nZero] = min(abs(v_Var(1:nMin))); % Zero before Last Zero
if nZero == 1
    nZero = nZero - v_Var(1)/( v_Var(2) - v_Var(1) );
else
    vZero = v_Var(nZero-1:nZero+1)';
    if vZero(1) * vZero(2) > 0
        nZero = nZero - vZero(2)/( vZero(3) - vZero(2) );
    else
        nZero = nZero - 1 - vZero(1)/( vZero(2) - vZero(1) );
    end
end
sPhase = pi/2 - (n_Interval/4+1-nZero)/n_Interval*2*pi;
vNT = sMax*cos([0:n_Interval]'/n_Interval*2*pi + pi/2 - sPhase);
sError = sqrt(dot(vNT-v_Var, vNT-v_Var))/(n_Interval+1);
m_HDF(:,7) = [sMax sPhase*180/pi sMax*cos(sPhase) sMax*sin(sPhase)
sError]';

[sTemp nZero] = min(abs(v_Var(nMin:nMax))); % Last Zero
vZero = v_Var(nMin+nZero-2:nMin+nZero)';
if vZero(1) * vZero(2) > 0
    nZero = (nMin + nZero - 1) - vZero(2)/( vZero(3) - vZero(2) );
else
    nZero = (nMin + nZero - 2) - vZero(1)/( vZero(2) - vZero(1) );
end
sPhase = pi/2 - (n_Interval*3/4+1-nZero)/n_Interval*2*pi;
vNT = sMax*cos([0:n_Interval]'/n_Interval*2*pi + pi/2 - sPhase);
sError = sqrt(dot(vNT-v_Var, vNT-v_Var))/(n_Interval+1);
m_HDF(:,8) = [sMax sPhase*180/pi sMax*cos(sPhase) sMax*sin(sPhase)
sError]';

sPhase = (m_HDF(2,7) + m_HDF(2,8))*pi/360; % Average
vNT = sMax*cos([0:n_Interval]'/n_Interval*2*pi + pi/2 - sPhase);
sError = sqrt(dot(vNT-v_Var, vNT-v_Var))/(n_Interval+1);
m_HDF(:,2) = [sMax sPhase*180/pi sMax*cos(sPhase) sMax*sin(sPhase)
sError]';

% Compare Last Maximum and Minimum
if v_Var(nMax+1) > v_Var(nMax-1)  % Maximum
    nMax = nMax + v_Var(nMax)/( v_Var(nMax) + v_Var(nMax+1) );
```

```
else
    nMax = nMax - v_Var(nMax)/( v_Var(nMax) + v_Var(nMax-1) );
end
sPhase = pi/2 - (n_Interval+1-nMax)/n_Interval*2*pi;
vNT = sMax*cos([0:n_Interval]'/n_Interval*2*pi + pi/2 - sPhase);
sError = sqrt(dot(vNT-v_Var, vNT-v_Var))/(n_Interval+1);
m_HDF(:,5) = [sMax sPhase*180/pi sMax*cos(sPhase) sMax*sin(sPhase)
sError]';

if v_Var(nMin+1) < v_Var(nMin-1)  % Minimum
    nMin = nMin + v_Var(nMin)/( v_Var(nMin) + v_Var(nMin+1) );
else
    nMin = nMin - v_Var(nMin)/( v_Var(nMin) + v_Var(nMin-1) );
end
sPhase = pi/2 - (n_Interval/2+1-nMin)/n_Interval*2*pi;
vNT = sMax*cos([0:n_Interval]'/n_Interval*2*pi + pi/2 - sPhase);
sError = sqrt(dot(vNT-v_Var, vNT-v_Var))/(n_Interval+1);
m_HDF(:,6) = [sMax sPhase*180/pi sMax*cos(sPhase) sMax*sin(sPhase)
sError]';

sPhase = pi/2 - (n_Interval*3/2+2-nMax-nMin)/n_Interval*pi; % Average
vNT = sMax*cos([0:n_Interval]'/n_Interval*2*pi + pi/2 - sPhase);
sError = sqrt(dot(vNT-v_Var, vNT-v_Var))/(n_Interval+1);
m_HDF(:,1) = [sMax sPhase*180/pi sMax*cos(sPhase) sMax*sin(sPhase)
sError]';

% Integral Method
vCos = cos([1:n_Interval]'/n_Interval*2*pi);
sPhase = pi/2 - acos(v_Var(2:end)'*vCos*2/sMax/n_Interval);
vNT = sMax*cos([0:n_Interval]'/n_Interval*2*pi + pi/2 - sPhase);
sError = sqrt(dot(vNT-v_Var, vNT-v_Var))/(n_Interval+1);
m_HDF(:,3) = [sMax sPhase*180/pi sMax*cos(sPhase) sMax*sin(sPhase)
sError]';

% Least Square Method (LSM)
vCos = cos([0:n_Interval]'/n_Interval*2*pi); s1 = dot(v_Var,
vCos)/dot(vCos, vCos);
vSin = sin([0:n_Interval]'/n_Interval*2*pi); s2 = dot(v_Var,
vSin)/dot(vSin, vSin);
sMag = sqrt(s1*s1 + s2*s2);                    sPhase = pi/2 - atan(-
s2/s1);
vNT = sMag*cos([0:n_Interval]'/n_Interval*2*pi + pi/2 - sPhase);
sError = sqrt(dot(vNT-v_Var, vNT-v_Var))/(n_Interval+1);
m_HDF(:,4) = [sMag sPhase*180/pi sMag*cos(sPhase) sMag*sin(sPhase)
sError]';
m_HDF


function plotEachRe(n_Last, m_Var, s_AspectRatio, s_Case, s_Reynolds,
m_Torque, m_HDF, m_Speed)
%% Called by: HDF_Plots()
%% Call: plotTorque()
subplot(2,2,1);
plotTorque(0, m_Var{1}, s_AspectRatio, s_Case, s_Reynolds, m_Torque,
m_HDF);
subplot(2,2,2);
```

```
plot(m_Speed(:,1),m_Speed(:,2)*100);   title([m_Var{2} ' (%)']);
xlabel('Arc Length (\mum)'); ylabel([m_Var{2} ' (%)']); grid on;
subplot(2,2,3);
plotTorque(1, m_Var{1}, s_AspectRatio, s_Case, s_Reynolds,
m_Torque(n_Last:end,:), m_HDF);
subplot(2,2,4);
bar(m_HDF(5,:), 'group'); title('Root Mean Square Error');
xlabel('Max&Min Zeros  Integral     LSM     Max      Min     Zero1
Zero2');


function plotTorque(n_Type, v_Var, s_AspectRatio, s_Case, s_Reynolds,
m_Torque, m_HDF)
%% Called by: plotEachRe()
if n_Type==0
    vTitle = ['(AspectRatio=' num2str(s_AspectRatio)];
    vTitle = [vTitle '  CaseNo=' num2str(s_Case)];
    vTitle = [vTitle '  Re=' num2str(s_Reynolds) ')'];
    mTitle = {v_Var, vTitle};
    plot(m_Torque(:,1), m_Torque(:,2), 'b.');
else
    mPara = {'Mag=', '  Phase=', '  Real=', '  Img='};
    mTitle = {'Max&Min: ' 'Zeros: ' 'Integral: ' 'LSM: '};
    for j=1:4
        for i=1:4
            mTitle{j} = [mTitle{j} mPara{i} num2str(m_HDF(i,j))];
        end
    end
    sPhase = 2*pi*(m_Torque(:,1) - m_Torque(1,1)) / (m_Torque(end,1) -
m_Torque(1,1));
    plot(m_Torque(:,1), m_HDF(1,4)*cos(sPhase), 'k', m_Torque(:,1),
m_Torque(:,2), 'b.');
end
title(mTitle);    xlabel('Time Step'); ylabel(v_Var);    grid on;


function plotEachCase(s_AspectRatio, s_Case, v_Reynolds, m_HDF, v_Re_ex,
m_HDF_Sader)
%% Called by: HDF_Plots()
vLegend1 = ['h/b=' num2str(s_AspectRatio) ' Case' num2str(s_Case) '
Max&Min'];
vLegend2 = ['h/b=' num2str(s_AspectRatio) ' Case' num2str(s_Case) '
Zeros'];
vLegend3 = ['h/b=' num2str(s_AspectRatio) ' Case' num2str(s_Case) '
Integral'];
vLegend4 = ['h/b=' num2str(s_AspectRatio) ' Case' num2str(s_Case) '
LSM'];

subplot(2,2,1);
loglog(v_Re_ex, m_HDF_Sader(:,1), 'k-', v_Reynolds, m_HDF(:,1,1),
'rv', ...
         v_Reynolds, m_HDF(:,1,2), 'rx', v_Reynolds, m_HDF(:,1,3),
'bo', ...
         v_Reynolds, m_HDF(:,1,4), 'b+');
title('Magnitude of Hydrodynamic Function'); %grid on;
xlabel('Re'); ylabel('Magnitude');
```

```
legend('h/b=0 (Sader)', vLegend1, vLegend2, vLegend3, vLegend4);

subplot(2,2,2);
loglog(v_Re_ex, m_HDF_Sader(:,3), 'k-', v_Reynolds, m_HDF(:,3,1),
'rv', ...
         v_Reynolds, m_HDF(:,3,2), 'rx', v_Reynolds, m_HDF(:,3,3),
'bo', ...
         v_Reynolds, m_HDF(:,3,4), 'b+');
title('Real Part of Hydrodynamic Function'); %grid on;
xlabel('Re'); ylabel('Real Part');
legend('h/b=0 (Sader)', vLegend1, vLegend2, vLegend3, vLegend4);

subplot(2,2,3);
semilogx(v_Re_ex, m_HDF_Sader(:,2), 'k-', v_Reynolds, m_HDF(:,2,1),
'rv', ...
           v_Reynolds, m_HDF(:,2,2), 'rx', v_Reynolds, m_HDF(:,2,3),
'bo', ...
           v_Reynolds, m_HDF(:,2,4), 'b+');
title('Phase of Hydrodynamic Function'); %grid on;
xlabel('Re'); ylabel('Phase (Degree)');
legend('h/b=0 (Sader)', vLegend1, vLegend2, vLegend3, vLegend4);

subplot(2,2,4);
loglog(v_Re_ex, m_HDF_Sader(:,4), 'k-', v_Reynolds, m_HDF(:,4,1),
'rv', ...
         v_Reynolds, m_HDF(:,4,2), 'rx', v_Reynolds, m_HDF(:,4,3),
'bo', ...
         v_Reynolds, m_HDF(:,4,4), 'b+');
title('Imaginary Part of Hydrodynamic Function'); %grid on;
xlabel('Re'); ylabel('Imaginary Part');
legend('h/b=0 (Sader)', vLegend1, vLegend2, vLegend3, vLegend4);


function plotEachAR(n_Case, s_AspectRatio, v_Reynolds, m_HDF, v_Re_ex,
m_HDF_Sader)
%% Called by: HDF_Plots()
%% n_Case=2 or 4
vLegend1 = ['h/b=' num2str(s_AspectRatio) ' Case1 LSM'];
vLegend2 = ['h/b=' num2str(s_AspectRatio) ' Case2 LSM'];
vLegend3 = ['h/b=' num2str(s_AspectRatio) ' Case3 LSM'];
vLegend4 = ['h/b=' num2str(s_AspectRatio) ' Case4 LSM'];

subplot(2,2,1);
if (n_Case==4)
    loglog(v_Re_ex, m_HDF_Sader(:,1), 'k-', v_Reynolds, m_HDF(1,:,1),
'bv', ...
        v_Reynolds, m_HDF(2,:,1), 'bx',  v_Reynolds, m_HDF(3,:,1),
'ro', ...
        v_Reynolds, m_HDF(4,:,1), 'r+');
    legend('h/b=0 (Sader)', vLegend1, vLegend2, vLegend3, vLegend4);
else
    loglog(v_Re_ex, m_HDF_Sader(:,1), 'k-', v_Reynolds, m_HDF(1,:,1),
'rv', ...
        v_Reynolds, m_HDF(2,:,1), 'bx');
    legend('h/b=0 (Sader)', vLegend1, vLegend2);
end
```

```
title('Magnitude of Hydrodynamic Function'); %grid on;
xlabel('Re'); ylabel('Magnitude');

subplot(2,2,2);
if (n_Case==4)
    loglog(v_Re_ex, m_HDF_Sader(:,3), 'k-', v_Reynolds, m_HDF(1,:,3),
'bv', ...
        v_Reynolds, m_HDF(2,:,3), 'bx',  v_Reynolds, m_HDF(3,:,3),
'ro', ...
        v_Reynolds, m_HDF(4,:,3), 'r+');
    legend('h/b=0 (Sader)', vLegend1, vLegend2, vLegend3, vLegend4);
else
    loglog(v_Re_ex, m_HDF_Sader(:,3), 'k-', v_Reynolds, m_HDF(1,:,3),
'rv', ...
        v_Reynolds, m_HDF(2,:,3), 'bx');
    legend('h/b=0 (Sader)', vLegend1, vLegend2);
end
title('Real Part of Hydrodynamic Function'); %grid on;
xlabel('Re'); ylabel('Real Part');

subplot(2,2,3);
if (n_Case==4)
    semilogx(v_Re_ex, m_HDF_Sader(:,2), 'k-', v_Reynolds, m_HDF(1,:,2),
'bv', ...
        v_Reynolds, m_HDF(2,:,2), 'bx',  v_Reynolds, m_HDF(3,:,2),
'ro', ...
        v_Reynolds, m_HDF(4,:,2), 'r+');
    legend('h/b=0 (Sader)', vLegend1, vLegend2, vLegend3, vLegend4);
else
    semilogx(v_Re_ex, m_HDF_Sader(:,2), 'k-', v_Reynolds, m_HDF(1,:,2),
'rv', ...
        v_Reynolds, m_HDF(2,:,2), 'bx');
    legend('h/b=0 (Sader)', vLegend1, vLegend2);
end
title('Phase of Hydrodynamic Function'); %grid on;
xlabel('Re'); ylabel('Phase (Degree)');

subplot(2,2,4);
if (n_Case==4)
    loglog(v_Re_ex, m_HDF_Sader(:,4), 'k-', v_Reynolds, m_HDF(1,:,4),
'bv', ...
        v_Reynolds, m_HDF(2,:,4), 'bx',  v_Reynolds, m_HDF(3,:,4),
'ro', ...
        v_Reynolds, m_HDF(4,:,4), 'r+');
    legend('h/b=0 (Sader)', vLegend1, vLegend2, vLegend3, vLegend4);
else
    loglog(v_Re_ex, m_HDF_Sader(:,4), 'k-', v_Reynolds, m_HDF(1,:,4),
'rv', ...
        v_Reynolds, m_HDF(2,:,4), 'bx');
    legend('h/b=0 (Sader)', vLegend1, vLegend2);
end
title('Imaginary Part of Hydrodynamic Function'); %grid on;
xlabel('Re'); ylabel('Imaginary Part');


function plotHDF(v_AspectRatio, v_Reynolds, m_HDF, v_Re_ex, m_HDF_Sader)
```

```
%% Called by: HDF_Plots()
%% Call: plotLegend()
subplot(2,2,1);
loglog(v_Re_ex, m_HDF_Sader(:,1), 'k-', v_Reynolds, m_HDF(:,:,1));
title('Magnitude of Hydrodynamic Function'); %grid on;
xlabel('Re'); ylabel('Magnitude');
plotLegend('h/b=', v_AspectRatio);

subplot(2,2,2);
loglog(v_Re_ex, m_HDF_Sader(:,3), 'k-', v_Reynolds, m_HDF(:,:,3));
title('Real Part of Hydrodynamic Function'); %grid on;
xlabel('Re'); ylabel('Real Part');
plotLegend('h/b=', v_AspectRatio);

subplot(2,2,3);
semilogx(v_Re_ex, m_HDF_Sader(:,2), 'k-', v_Reynolds, m_HDF(:,:,2));
title('Phase of Hydrodynamic Function'); %grid on;
xlabel('Re'); ylabel('Phase (Degree)');
plotLegend('h/b=', v_AspectRatio);

subplot(2,2,4);
loglog(v_Re_ex, m_HDF_Sader(:,4), 'k-', v_Reynolds, m_HDF(:,:,4));
title('Imaginary Part of Hydrodynamic Function'); %grid on;
xlabel('Re'); ylabel('Imaginary Part');
plotLegend('h/b=', v_AspectRatio);


function plotLegend(v_Text, v_AspectRatio)
%% Called by: plotHDF()
switch length(v_AspectRatio)
    case 1
        legend('h/b=0 (Sader)', [v_Text num2str(v_AspectRatio(1))]);
    case 2
        legend('h/b=0 (Sader)', [v_Text num2str(v_AspectRatio(1))], ...
               [v_Text num2str(v_AspectRatio(2))]);
    case 3
        legend('h/b=0 (Sader)', [v_Text num2str(v_AspectRatio(1))], ...
               [v_Text num2str(v_AspectRatio(2))], ...
               [v_Text num2str(v_AspectRatio(3))]);
    case 4
        legend('h/b=0 (Sader)', [v_Text num2str(v_AspectRatio(1))], ...
               [v_Text num2str(v_AspectRatio(2))], ...
               [v_Text num2str(v_AspectRatio(3))], ...
               [v_Text num2str(v_AspectRatio(4))]);
    case 5
        legend('h/b=0 (Sader)', [v_Text num2str(v_AspectRatio(1))], ...
               [v_Text num2str(v_AspectRatio(2))], ...
               [v_Text num2str(v_AspectRatio(3))], ...
               [v_Text num2str(v_AspectRatio(4))], ...
               [v_Text num2str(v_AspectRatio(5))]);
    case 6
        legend('h/b=0 (Sader)', [v_Text num2str(v_AspectRatio(1))], ...
               [v_Text num2str(v_AspectRatio(2))], ...
               [v_Text num2str(v_AspectRatio(3))], ...
               [v_Text num2str(v_AspectRatio(4))], ...
               [v_Text num2str(v_AspectRatio(5))], ...
```

```
                [v_Text num2str(v_AspectRatio(6))]);
    case 7
        legend('h/b=0 (Sader)', [v_Text num2str(v_AspectRatio(1))], ...
                [v_Text num2str(v_AspectRatio(2))], ...
                [v_Text num2str(v_AspectRatio(3))], ...
                [v_Text num2str(v_AspectRatio(4))], ...
                [v_Text num2str(v_AspectRatio(5))], ...
                [v_Text num2str(v_AspectRatio(6))], ...
                [v_Text num2str(v_AspectRatio(7))]);
    case 8
        legend('h/b=0 (Sader)', [v_Text num2str(v_AspectRatio(1))], ...
                [v_Text num2str(v_AspectRatio(2))], ...
                [v_Text num2str(v_AspectRatio(3))], ...
                [v_Text num2str(v_AspectRatio(4))], ...
                [v_Text num2str(v_AspectRatio(5))], ...
                [v_Text num2str(v_AspectRatio(6))], ...
                [v_Text num2str(v_AspectRatio(7))], ...
                [v_Text num2str(v_AspectRatio(8))]);
    case 9
        legend('h/b=0 (Sader)', [v_Text num2str(v_AspectRatio(1))], ...
                [v_Text num2str(v_AspectRatio(2))], ...
                [v_Text num2str(v_AspectRatio(3))], ...
                [v_Text num2str(v_AspectRatio(4))], ...
                [v_Text num2str(v_AspectRatio(5))], ...
                [v_Text num2str(v_AspectRatio(6))], ...
                [v_Text num2str(v_AspectRatio(7))], ...
                [v_Text num2str(v_AspectRatio(8))], ...
                [v_Text num2str(v_AspectRatio(9))]);
    case 10
        legend('h/b=0 (Sader)', [v_Text num2str(v_AspectRatio(1))], ...
                [v_Text num2str(v_AspectRatio(2))], ...
                [v_Text num2str(v_AspectRatio(3))], ...
                [v_Text num2str(v_AspectRatio(4))], ...
                [v_Text num2str(v_AspectRatio(5))], ...
                [v_Text num2str(v_AspectRatio(6))], ...
                [v_Text num2str(v_AspectRatio(7))], ...
                [v_Text num2str(v_AspectRatio(8))], ...
                [v_Text num2str(v_AspectRatio(9))], ...
                [v_Text num2str(v_AspectRatio(10))]);
    case 11
        legend('h/b=0 (Sader)', [v_Text num2str(v_AspectRatio(1))], ...
                [v_Text num2str(v_AspectRatio(2))], ...
                [v_Text num2str(v_AspectRatio(3))], ...
                [v_Text num2str(v_AspectRatio(4))], ...
                [v_Text num2str(v_AspectRatio(5))], ...
                [v_Text num2str(v_AspectRatio(6))], ...
                [v_Text num2str(v_AspectRatio(7))], ...
                [v_Text num2str(v_AspectRatio(8))], ...
                [v_Text num2str(v_AspectRatio(9))], ...
                [v_Text num2str(v_AspectRatio(10))], ...
                [v_Text num2str(v_AspectRatio(11))]);
    otherwise
        legend('h/b=0 (Sader)', [v_Text num2str(v_AspectRatio(1))], ...
                [v_Text num2str(v_AspectRatio(2))], ...
                [v_Text num2str(v_AspectRatio(3))], ...
                [v_Text num2str(v_AspectRatio(4))], ...
                [v_Text num2str(v_AspectRatio(5))], ...
```

```
                              [v_Text num2str(v_AspectRatio(6))], ...
                              [v_Text num2str(v_AspectRatio(7))], ...
                              [v_Text num2str(v_AspectRatio(8))], ...
                              [v_Text num2str(v_AspectRatio(9))], ...
                              [v_Text num2str(v_AspectRatio(10))], ...
                              [v_Text num2str(v_AspectRatio(11))], ...
                              [v_Text num2str(v_AspectRatio(12))]);
end
```

APPENDIX C NUMERICAL RESULTS FROM COMSOL AND MATLAB

Table C-1: Magnitude of the hydrodynamic function of a torsionally vibrating microcantilever found as a function of Reynolds number and aspect ratio (*h*/*b*)

h / *b* Re	0.001	0.002	0.005	0.01	0.02	0.05	0.1	0.2	0.3	0.5	1
1	1.1715	1.1750	1.1795	1.1892	1.2047	1.2474	1.3201	1.4672	1.6204	1.9446	2.8650
1.778	0.7333	0.7357	0.7385	0.7449	0.7548	0.7815	0.8267	0.9183	1.0145	1.2206	1.8374
3.162	0.4802	0.4817	0.4837	0.4875	0.4939	0.5110	0.5401	0.5989	0.6606	0.7953	1.2220
5.623	0.3315	0.3325	0.3335	0.3360	0.3402	0.3519	0.3712	0.4097	0.4502	0.5396	0.8445
10	0.2419	0.2430	0.2428	0.2447	0.2474	0.2553	0.2686	0.2945	0.3217	0.3818	0.6041
17.78	0.1853	0.1859	0.1864	0.1884	0.1904	0.1952	0.2055	0.2227	0.2421	0.2822	0.4459
31.62	0.1501	0.1501	0.1510	0.1508	0.1534	0.1564	0.1643	0.1775	0.1893	0.2158	0.3388
56.23	0.1259	0.1261	0.1261	0.1270	0.1283	0.1319	0.1374	0.1469	0.1553	0.1730	0.2658
100	0.1089	0.1092	0.1094	0.1099	0.1109	0.1143	0.1187	0.1256	0.1311	0.1425	0.2146
177.8	0.0972	0.0976	0.0976	0.0980	0.0989	0.1018	0.1062	0.1116	0.1148	0.1211	0.1782
316.2	0.0887	0.0883	0.0888	0.0894	0.0905	0.0930	0.0972	0.1008	0.1028	0.1059	0.1519
562.3	0.0821	0.0820	0.0824	0.0831	0.0845	0.0870	0.0901	0.0932	0.0949	0.0955	0.1333
1000	0.0775	0.0775	0.0778	0.0785	0.0797	0.0827	0.0848	0.0880	0.0883	0.0878	0.1191
1778	0.0738	0.0737	0.0742	0.0750	0.0761	0.0789	0.0819	0.0838	0.0841	0.0817	0.1095
3162	0.0710	0.0716	0.0718	0.0725	0.0736	0.0762	0.0784	0.0808	0.0802	0.0774	0.1022
5623	0.0693	0.0692	0.0697	0.0709	0.0719	0.0743	0.0771	0.0787	0.0778	0.0745	0.0971
10000	0.0678	0.0681	0.0686	0.0694	0.0705	0.0733	0.0760	0.0776	0.0770	0.0722	0.0930
17780	0.0668	0.0669	0.0677	0.0684	0.0694	0.0726	0.0746	0.0759	0.0753	0.0705	0.0896
31620	0.0659	0.0663	0.0668	0.0676	0.0688	0.0714	0.0741	0.0755	0.0738	0.0693	0.0874

Table C-2: Phase of the hydrodynamic function of a torsionally vibrating microcantilever found as a function of Reynolds number and aspect ratio (*h*/*b*)

h / *b* Re	0.001	0.002	0.005	0.01	0.02	0.05	0.1	0.2	0.3	0.5	1
1	73.446	73.459	73.456	73.464	73.425	73.469	73.524	73.651	73.745	73.514	70.810
1.778	67.630	67.643	67.650	67.599	67.687	67.735	67.876	68.177	68.437	68.493	65.901
3.162	60.845	60.867	60.873	60.921	60.970	61.084	61.327	61.847	62.363	62.967	60.765
5.623	53.470	53.503	53.528	53.601	53.676	53.762	54.171	54.950	55.772	57.022	55.452
10	45.928	45.899	46.101	46.165	46.266	46.459	46.855	47.860	48.999	50.983	50.427
17.78	38.937	38.969	39.006	39.025	39.035	39.336	39.700	40.918	42.279	45.008	45.610
31.62	32.406	32.484	32.491	32.517	32.578	32.754	33.255	34.482	36.033	39.302	40.868
56.23	26.760	26.775	26.940	26.831	26.793	26.854	27.178	28.585	30.360	33.968	36.341
100	21.832	21.905	21.861	21.877	21.813	21.784	21.990	23.331	25.069	28.967	32.017
177.8	17.789	17.924	17.767	17.688	17.548	17.428	17.971	19.053	20.539	24.262	28.268
316.2	14.395	14.378	14.207	14.212	14.108	13.810	14.314	15.025	16.450	20.060	23.666
562.3	11.438	11.582	11.450	11.241	11.287	11.164	11.056	11.840	13.509	16.873	20.539
1000	9.1078	9.2187	9.0571	9.0810	8.7230	8.7501	9.0709	9.4912	11.407	13.657	17.189
1778	7.3602	7.7177	7.2134	7.0920	7.1145	6.7003	6.9052	7.3758	8.3030	11.282	13.472
3162	6.0364	5.7342	6.0482	5.5089	5.5981	5.4995	6.0809	6.0862	7.2833	8.8285	11.177
5623	4.8634	4.8489	4.9457	4.2591	4.1283	4.1072	4.0817	4.5158	5.5149	6.3905	8.7003
10000	3.6137	3.4838	3.4489	3.6213	3.3491	3.1181	3.2958	3.2859	4.1201	5.1145	6.5911
17780	2.8749	2.8618	3.0242	2.6605	2.5993	2.6592	2.7601	3.1622	4.0697	4.6986	5.3963
31620	2.4091	2.1405	2.1526	1.9450	2.0109	2.0086	1.8001	1.9517	2.4977	2.9956	4.5383

Table C-3: Real part of the hydrodynamic function of a torsionally vibrating microcantilever found as a function of Reynolds number and aspect ratio (*h*/*b*)

h / b **Re**	**0.001**	**0.002**	**0.005**	**0.01**	**0.02**	**0.05**	**0.1**	**0.2**	**0.3**	**0.5**	**1**
1	0.3338	0.3345	0.3359	0.3385	0.3437	0.3549	0.3744	0.4130	0.4536	0.5519	0.9417
1.778	0.2791	0.2798	0.2808	0.2839	0.2866	0.2961	0.3113	0.3414	0.3729	0.4475	0.7503
3.162	0.2339	0.2345	0.2355	0.2369	0.2397	0.2471	0.2591	0.2826	0.3064	0.3615	0.5968
5.623	0.1973	0.1977	0.1983	0.1994	0.2015	0.2080	0.2173	0.2353	0.2532	0.2937	0.4789
10	0.1682	0.1691	0.1684	0.1695	0.1710	0.1758	0.1837	0.1976	0.2111	0.2404	0.3848
17.78	0.1441	0.1445	0.1448	0.1464	0.1479	0.1510	0.1581	0.1683	0.1791	0.1995	0.3119
31.62	0.1267	0.1266	0.1274	0.1271	0.1293	0.1315	0.1374	0.1463	0.1531	0.1670	0.2562
56.23	0.1124	0.1126	0.1124	0.1133	0.1145	0.1177	0.1222	0.1290	0.1340	0.1435	0.2141
100	0.1011	0.1013	0.1015	0.1020	0.1030	0.1061	0.1100	0.1153	0.1187	0.1247	0.1819
177.8	0.0925	0.0928	0.0929	0.0934	0.0943	0.0971	0.1010	0.1055	0.1075	0.1104	0.1569
316.2	0.0859	0.0856	0.0861	0.0867	0.0878	0.0903	0.0942	0.0974	0.0986	0.0995	0.1391
562.3	0.0804	0.0803	0.0808	0.0815	0.0828	0.0854	0.0884	0.0912	0.0923	0.0914	0.1249
1000	0.0766	0.0765	0.0768	0.0775	0.0787	0.0817	0.0837	0.0868	0.0865	0.0853	0.1138
1778	0.0731	0.0731	0.0736	0.0744	0.0755	0.0783	0.0813	0.0831	0.0833	0.0801	0.1064
3162	0.0706	0.0713	0.0714	0.0721	0.0732	0.0759	0.0780	0.0803	0.0796	0.0765	0.1003
5623	0.0691	0.0690	0.0695	0.0707	0.0718	0.0741	0.0769	0.0785	0.0775	0.0741	0.0960
10000	0.0676	0.0680	0.0685	0.0693	0.0704	0.0732	0.0759	0.0774	0.0768	0.0719	0.0924
17780	0.0667	0.0668	0.0676	0.0683	0.0693	0.0725	0.0745	0.0757	0.0751	0.0702	0.0892
31620	0.0658	0.0663	0.0668	0.0675	0.0687	0.0714	0.0740	0.0754	0.0738	0.0692	0.0871

Table C-4: Imaginary part of the hydrodynamic function of a torsionally vibrating microcantilever found as a function of Reynolds number and aspect ratio (*h*/*b*)

h / b Re	0.001	0.002	0.005	0.01	0.02	0.05	0.1	0.2	0.3	0.5	1
1	1.1229	1.1264	1.1307	1.1401	1.1547	1.1959	1.2659	1.4078	1.5556	1.8647	2.7058
1.778	0.6781	0.6804	0.6830	0.6887	0.6982	0.7232	0.7658	0.8525	0.9435	1.1356	1.6773
3.162	0.4194	0.4208	0.4226	0.4260	0.4319	0.4473	0.4738	0.5281	0.5852	0.7084	1.0664
5.623	0.2664	0.2673	0.2682	0.2704	0.2741	0.2839	0.3009	0.3354	0.3722	0.4527	0.6955
10	0.1738	0.1745	0.1750	0.1765	0.1787	0.1850	0.1960	0.2184	0.2428	0.2966	0.4656
17.78	0.1164	0.1169	0.1173	0.1186	0.1199	0.1237	0.1313	0.1459	0.1628	0.1996	0.3187
31.62	0.0805	0.0806	0.0811	0.0810	0.0826	0.0846	0.0901	0.1005	0.1114	0.1367	0.2217
56.23	0.0567	0.0568	0.0571	0.0573	0.0578	0.0596	0.0627	0.0703	0.0785	0.0966	0.1575
100	0.0405	0.0407	0.0407	0.0410	0.0412	0.0424	0.0444	0.0497	0.0555	0.0690	0.1138
177.8	0.0297	0.0300	0.0298	0.0298	0.0298	0.0305	0.0328	0.0364	0.0403	0.0498	0.0844
316.2	0.0221	0.0219	0.0218	0.0220	0.0221	0.0222	0.0240	0.0261	0.0291	0.0363	0.0610
562.3	0.0163	0.0165	0.0164	0.0162	0.0165	0.0169	0.0173	0.0191	0.0222	0.0277	0.0468
1000	0.0123	0.0124	0.0122	0.0124	0.0121	0.0126	0.0134	0.0145	0.0175	0.0207	0.0352
1778	0.0094	0.0099	0.0093	0.0093	0.0094	0.0092	0.0098	0.0108	0.0122	0.0160	0.0255
3162	0.0075	0.0072	0.0076	0.0070	0.0072	0.0073	0.0083	0.0086	0.0102	0.0119	0.0198
5623	0.0059	0.0059	0.0060	0.0053	0.0052	0.0053	0.0055	0.0062	0.0075	0.0083	0.0147
10000	0.0043	0.0041	0.0041	0.0044	0.0041	0.0040	0.0044	0.0044	0.0055	0.0064	0.0107
17780	0.0033	0.0033	0.0036	0.0032	0.0031	0.0034	0.0036	0.0042	0.0053	0.0058	0.0084
31620	0.0028	0.0025	0.0025	0.0023	0.0024	0.0025	0.0023	0.0026	0.0032	0.0036	0.0069

APPENDIX D MATLAB PROGRAM USED TO CALCULATE FREQUENCY SPECTRUM, CHARATERISTICS, AND DESIGNED DIMENSION FOR TORSIONALLY VIBRATING RECTANULGAR MICROCANTILEVERS IN VISCOUS LIQUIDS

```
function mPhi_fr_df_Q = Freq_Spectrum(str_Method, str_Structure,
str_Fluid, s_L, s_b, s_h, s_df, v_f)
%% str_Method     string variable, Name of Method/Theory for Torsional
Mode
%%                  Ribbon  Ignore Thickness Effect
%%                  Thick0  Consider Thickness Effect on K, J and
Hydrodynamic Function
%%                  Thick1  Consider Thickness Effect on only J and
Hydrodynamic Function
%%                  Thick2  Consider Thickness Effect on only K and
Hydrodynamic Function
%%                  Thick3  Consider Thickness Effect on only K and J
%% str_Structure  string variable, Material Name of the Structure
%% str_Fluid      string variable, Material Name of the Fluid
%% s_L            scaler variable, Length of the microcantilevers
%% s_b            scaler variable, Width of the microcantilevers
%% s_h            scaler variable, Thickness of the microcantilevers
%% s_df           scaler variable, slightly larger than half of 3-dB
bandwidth
%% v_f            vector variable, Excitation Frequencies
%% Called by: Characteristics()
%% Call: getMatProp_Value(), getHDF_Thick()
%% mPhi_fr_df_Q   matrix variable.
%%                  1-4 rows are Normalized Deflectoin, Resonance
Frequency,
%%                               3-dB bandwidth, and Quality Factor,
respectively.
%%                  1-4 columns are for 2nd Transverse, 1st Transverse,
1st Lateral, 1st Torsional modes.
disp(['***  Freq_Spectrum: ' str_Structure ', ' str_Fluid ', '
str_Method '  ***']);
[sE, sG, sRho, sRho_L, sEta, vPercent] = getMatProp_Value(str_Structure,
str_Fluid);
sAspectRatio = s_h / s_b;  % [.], Aspect Ratio (h/b)
if strcmp(str_Method, 'Ribbon') | strcmp(str_Method, 'Thick1')
    sK = s_b*s_h^3/3;      % [m^4], Geometric Function of the cross-
section, h/b=0
else
    vxn = [0 1/10  1/5  1/4 1/3  2/5  1/2  2/3    1]'; % h/b
    vyn = [6 6.41 6.87 7.12 7.6 8.03 8.73 10.2 14.2]'; % k2
    sk2 = interp1(vxn,vyn,sAspectRatio,'linear'); % Get the parameter
by linear interpolation
    sK  = 2*s_b*s_h^3/sk2; % [m^4], Geometric Function of the cross-
section, real h/b
end
if strcmp(str_Method, 'Ribbon') | strcmp(str_Method, 'Thick2')
    sJ = s_b^3*s_h/12;     % [m^4], Polar moment of the area, h/b=0
else
```

```
    sJ  = s_b*s_h*(s_b*s_b + s_h*s_h)/12; % [m^4], Polar moment of the
area, real h/b
end
sBend = pi*sRho_L*s_b*s_b/4;           % [.], Intermediate term for
Transverse and Lateral Modes
sTors = pi*sRho_L*s_b^4/8;             % [.], Intermediate term for
Torsional Mode
vRe = sRho_L*2*pi*v_f*s_b*s_b/4/sEta; % [.], Reynolds number
mfs = zeros(length(v_f),3);            % [dB], Frequency Spectrum

% Prediction of E and G from resonance frequency in air/vacuum
% E = 110 GPa;    G = 45.4 GPa
sf_tran1_air = 154.6;   % [kHz]
sE_tran1 = 48*pi^2*s_L^4*sRho*sf_tran1_air^2/1.8751^4/s_h^2/1E3; %
109.8622 [GPa]
sf_lat1_air  = 636.68;  % [kHz]
sE_lat1 =  48*pi^2*s_L^4*sRho*sf_lat1_air^2/1.8751^4/s_b^2/1E3;  %
114.3922 [GPa]
sf_tran2_air = 954.57;  % [kHz]
sE_tran2 = 48*pi^2*s_L^4*sRho*sf_tran2_air^2/4.6941^4/s_h^2/1E3; %
106.6432 [GPa]
sf_tors1_air = 1218.79; % [kHz]
sG_tors1 = 16*s_L^2*sRho*sJ*sf_tors1_air^2/sK/1E3; % 45.3728 [GPa]
sE_calc = (sE_tran1 + sE_tran2 + sE_lat1)/3;

% Transverse and Lateral Modes
sEI_T = sE*s_b*s_h^3/12;              % [N.m^2], Transverse Bending
Rigidity
sEI_L = sE*s_b^3*s_h/12;              % [N.m^2], Lateral Bending
Rigidity
vBetaL = [1.8751 4.6941 7.8548 10.9955 14.1372]';
syms x;
vPhi1 = ( cos(vBetaL*x/s_L) - cosh(vBetaL*x/s_L) ) .* ( cos(vBetaL) +
cosh(vBetaL) );
vPhi2 = ( sin(vBetaL*x/s_L) - sinh(vBetaL*x/s_L) ) .* ( sin(vBetaL) -
sinh(vBetaL) );
vPhi  = (vPhi1 + vPhi2) ./ ( sin(vBetaL) - sinh(vBetaL) );
vt01 = [0.000213321956162338; 8.52133529324053e-05; 5.09242756021669e-
05; ...
        3.63785184845922e-05; 2.82941459435193e-05;]; % eval(int(vPhi,
x, 0, s_L));
vt02 = [0.000371130872675644; 0.000192813260010481;
0.000200311621486068; ...
        0.000199985838593808; 0.000200000542916072;]; %
eval(int(vPhi.*vPhi, x, 0, s_L));

% Transverse Mode
mHDF_Best = getHDF_Thick('Transverse Rectangular Ribbon Sader', vRe,
sAspectRatio);
if strcmp(str_Fluid, 'Vacuum')
    vg1 = 0; vg2=0;
else
    vg1 = pi * sEta .* vRe .* mHDF_Best(:,1,4);
    vg2 = sBend*mHDF_Best(:,1,3);
end
vt1 = 2*pi*v_f .* vg1;
```

```
vt20 = 4*pi*pi*v_f.*v_f.*(sRho*s_b*s_h + vg2);
for i=1:5
    vt2 = sEI_T*vBetaL(i)^4/s_L^4 - vt20;
    vt_i = sqrt(vt1 .* vt1 + vt2 .* vt2);
    vy_i = vt01(i) / vt02(i) ./ vt_i;
    mfs(:,1) = mfs(:,1) + vy_i;
end

% Lateral Mode
if strcmp(str_Method, 'Ribbon') | strcmp(str_Method, 'Thick3')
    mHDF_Best = getHDF_Thick('Lateral Rectangular Ribbon Stokes', vRe,
sAspectRatio);
else
    mHDF_Best = getHDF_Thick('Lateral Rectangular Thickness Russell',
vRe, sAspectRatio);
end
if strcmp(str_Fluid, 'Vacuum')
    vg1 = 0; vg2=0;
else
    vg1 = pi * sEta .* vRe .* mHDF_Best(:,1,4);
    vg2 = sBend*mHDF_Best(:,1,3);
end
vt1 = 2*pi*v_f .* vg1;
vt20 = 4*pi*pi*v_f.*v_f.*(sRho*s_b*s_h + vg2);
for i=1:5
    vt2 = sEI_L*vBetaL(i)^4/s_L^4 - vt20;
    vt_i = sqrt(vt1 .* vt1 + vt2 .* vt2);
    vy_i = vt01(i) / vt02(i) ./ vt_i;
    mfs(:,2) = mfs(:,2) + vy_i;
end
% Simple formula for Q at resonance [Heinrich 2010]
sQ_Lateral = 0.7124*(sE*sRho^3)^0.25*s_h*sqrt(s_b/sEta/sRho_L)/s_L;

% Torsional mode
if strcmp(str_Method, 'Ribbon') | strcmp(str_Method, 'Thick3')
    mHDF_Best = getHDF_Thick('Torsional Rectangular Ribbon Sader', vRe,
sAspectRatio);
else
    mHDF_Best = getHDF_Thick('Torsional Rectangular Thickness Tao2',
vRe, sAspectRatio);
end
if strcmp(str_Fluid, 'Vacuum')
    vg1 = 0; vg2=0;
else
    vg1 = sTors*2*pi*v_f .* mHDF_Best(:,1,4);
    vg2 = sTors*mHDF_Best(:,1,3);
end
vt1 = 2*pi*v_f .* vg1;
vt20 = 4*pi*pi*v_f.*v_f.*(sRho*sJ + vg2);
for i=1:5
    sLambda_i = (2*i-1)*pi/2/s_L;
    vt2 = sG*sK*sLambda_i*sLambda_i - vt20;
    vt_i = sqrt(vt1 .* vt1 + vt2 .* vt2);
    vy_i = 4*(-1)^(i+1)*sG*sK/sLambda_i/s_L^3 ./ vt_i;
    mfs(:,3) = mfs(:,3) + vy_i;
end
```

```
% Normalization
mfs(:,1) = mfs(:,1)/mfs(1,1);
mfs(:,2) = mfs(:,2)/mfs(1,2);
mfs = 20*log10(abs(mfs)); % [dB]
m_f_Tran_Lat_Tors = [v_f mfs];

% vPhi, [dB], Maximum Normalized Tip Rotation
% vfr,  [Hz], Resonance Frequency
[vPhi, vIndex] = max(mfs);
[sPhi, sIndex] = max(mfs(2*vIndex(1):end,1));
mPhi_fr = [sPhi, vPhi; (sIndex+2*vIndex(1)-2)*(v_f(2)-v_f(1)), (vIndex-
1)*(v_f(2)-v_f(1))];
vIndex = [sIndex+2*vIndex(1)-1 vIndex];
tmfs = abs( [mfs(:,1) mfs] - kron(mPhi_fr(1,:)-3,
ones(length(mfs(:,1)),1)) );
vdf = zeros(1,4);
for i=1:4
    [t1Phi, t1Index] = min(tmfs(vIndex(i)-s_df/(v_f(2)-
v_f(1)):vIndex(i),i));
    [t2Phi, t2Index] = min(tmfs(vIndex(i):vIndex(i)+s_df/(v_f(2)-
v_f(1)),i));
    tInfo = [i t1Index t2Index]; % only for test
    vdf(i) = (t2Index - t1Index) * (v_f(2)-v_f(1)) + s_df;
end
vQ = mPhi_fr(2,:) ./ vdf; % 3-dB Bandwidth Quality Factor
mPhi_fr_df_Q = [mPhi_fr; vdf; vQ];
mPhi_fr(2,:)
save(['postprocess21_FreqSpectrum_' str_Structure '_' str_Fluid '_'
str_Method '.mat'], ...
    'm_f_Tran_Lat_Tors', 'mPhi_fr_df_Q', 'vt01', 'vt02', 'sQ_Lateral');

figure(8);
plot(v_f/1E6, mfs(:,1), 'r-', v_f/1E6, mfs(:,2), 'k-', ...
     v_f/1E6, mfs(:,3), 'b-'); grid on;
xlabel('Excitation Frequency (MHz)'); ylabel('Normalized Tip Rotation
(dB)');
legend('Transverse Modes', 'Lateral Modes', 'Torsional Modes',
'Location', 'Best');
set(gcf, 'PaperPosition', [0.25 2.5 13.33 10.0]);
print('-dtiff', ['PostProcessF21_FreqSpectrum_' str_Structure '_'
str_Fluid '_' str_Method '.tif']);


function Characteristics_Torsional(str_Structure, str_Fluid, v_L, v_b,
v_h, n_Iter, n_i, st_name)
%% v_L      vector variable, Length of the microcantilevers
%% v_b      vector variable, Width of the microcantilevers
%% v_h      vector variable, Thickness of the microcantilevers
%% n_Iter   scalar variable, Maximum Number of Iteration
%% n_i      No. of different Length, Width, or Thickness
%% st_name  Part of the file name of the saved figures
%% Called by: Characteristics()
%% Call: getHDF_Ribbon(), getHDF_Thick(), getHDF_tors_rect_Sader(),
getMatProp_Value()
```

```
% sE     [Pa], Young's Modulus of Microcantilever
% sG     [Pa], Shear Modulus of Microcantilever
% vRho   [kg/m^3], Density of Microcantilever
% vEta   [Ns/m^2]=[kg/s/m], Viscosity of Fluid
% vRho_L [kg/m^3], Density of Fluid
% vPercent [%], percent (w/w) of Aqueous Fluid
[sE, sG, vRho, vRho_L, vEta, vPercent] = getMatProp_Value(str_Structure,
str_Fluid);

vAspectRatio = v_h ./ v_b; % [.], Aspect Ratio (h/b)
vxn = [0 1/10  1/5  1/4 1/3  2/5  1/2  2/3    1]'; % h/b
vyn = [6 6.41 6.87 7.12 7.6 8.03 8.73 10.2 14.2]'; % k2
vk2 = interp1(vxn,vyn,vAspectRatio,'linear'); % Get the parameter by
linear interpolation
vK0 = v_b.*v_h.^3/3;       % [m^4], Geometric Function of the cross-
section, h/b=0
vK  = 2*v_b.*v_h.^3./vk2;  % [m^4], Geometric Function of the cross-
section, real h/b
vJ0 = v_b.^3.*v_h/12;                    % [m^4], Polar moment of the
area, h/b=0
vJ  = v_b.*v_h.*(v_b.*v_b + v_h.*v_h)/12; % [m^4], Polar moment of the
area, real h/b
vT0 = pi*vRho_L.*v_b.^4/8./vRho./vJ0;     % [.], Intermediate term
vT  = pi*vRho_L.*v_b.^4/8./vRho./vJ;      % [.], Intermediate term
vrJV = (v_b.*v_b + 3*v_h.*v_h) ./ v_L/12; % [.], Ratio of J to V of the
coating layer (film)

vfVac1  = sqrt(sG*vK0./vRho./vJ0)./v_L/4/1E6; % [MHz], Resonant
Frequency in Vacuum, h/b=0
vfVac1K = sqrt(sG*vK./vRho./vJ)./v_L/4/1E6;   % [MHz], Resonant
Frequency in Vacuum, real h/b
vfInvF1 = vfVac1K./sqrt(1 + 3*pi*vRho_L./vRho/32./vAspectRatio); %
[MHz], Resonant Frequency in Inviscid Liquid
mfVisF1s = zeros(length(vAspectRatio), n_Iter+1);
mfVisF1s(:,1) = vfVac1K/1000;     mfVisF1c = mfVisF1s;
for i=1:n_Iter
    vRe_Sader = vRho_L*pi.*v_b.^2/2./vEta.*mfVisF1s(:,i)*1E6;
    mHDF_Sader = getHDF_Ribbon('Torsional Rectangular', vRe_Sader); %
[vmag vphase vreal vimg]
    mfVisF1s(:,i+1) = vfVac1 ./ sqrt(1 + vT0 .* mHDF_Sader(:,3));
    vRe_Best = vRho_L*pi.*v_b.^2/2./vEta.*mfVisF1c(:,i)*1E6;
    mHDF_Best1 = getHDF_Thick('Torsional Rectangular Thickness Tao2',
vRe_Best, vAspectRatio); % mmag, mphase, mreal, mimg
    mfVisF1c(:,i+1) = vfVac1K ./ sqrt(1 + vT .*
diag(mHDF_Best1(:,:,3)));
end

vRe_Sader = vRho_L*pi.*v_b.^2/2./vEta.*mfVisF1s(:,end)*1E6;
mHDF_Sader = getHDF_Ribbon('Torsional Rectangular', vRe_Sader); % [vmag
vphase vreal vimg]
vQ_Sader = (1 ./ vT0 + mHDF_Sader(:,3)) ./ mHDF_Sader(:,4);
vSm_Sader = 1E-9*mfVisF1s(:,end)/2./vRho./vJ0./( 1 +
vT0.*mHDF_Sader(:,3) ).*vrJV;
vLODm_bar_Sader = 1.5*mfVisF1s(:,end)./vQ_Sader./vSm_Sader;
vSc_bar_Sader = 1E6*mfVisF1s(:,end)/2./vRho./( 1 +
vT0.*mHDF_Sader(:,3) );
```

```
vLODc_bar_Sader = 1.5E6*mfVisF1s(:,end)./vQ_Sader./vSc_bar_Sader;
vRe_Best = vRho_L*pi.*v_b.^2/2./vEta.*mfVisF1c(:,end)*1E6;
mHDF_Best1 = getHDF_Thick('Torsional Rectangular Thickness Tao2',
vRe_Best, vAspectRatio); % mmag, mphase, mreal, mimg
vQ_Best = (1 ./ vT + diag(mHDF_Best1(:,:,3))) ./
diag(mHDF_Best1(:,:,4));
vSm_Best = 1E-9*mfVisF1c(:,end)/2./vRho./vJ./( 1 +
vT.*mHDF_Best1(:,3) ).*vrJV;
vLODm_bar_Best = 1.5*mfVisF1c(:,end)./vQ_Best./vSm_Best;
vSc_bar_Best = 1E6*mfVisF1c(:,end)/2./vRho./( 1 + vT.*mHDF_Best1(:,3) );
vLODc_bar_Best = 1.5E6*mfVisF1c(:,end)./vQ_Best./vSc_bar_Best;

% h: Thickness, b: Width, L: Length, h/b: Aspect Ratio, Re: Reynolds
Number,
% f: Resonance Frequency, Q: Quality Factor, S: Normalized Sensitivity,
LOD: Limit of Detection
% vac1:  First mode in Vacuum for Ribbon Case  (h/b->0)
% vac1K: First mode in Vacuum for General Case (Finite h/b)
% _c: Chemical,  _C: Chu,  _S: Sader,  _F: Our approach
%
% h[um], b[um], L[um], h/b, h/(bL)[/m],
% f_vac1[MHz], fvac1K[MHz], f_C[MHz], f_S[MHz], f_F[MHz]
% Re_S[1E3], Re_F[1E3], S_m_S[Hz/pg], S_m_F[Hz/pg],
% h/sqrt(L), Q_S, Q_F, sqrt(L)/h, LOD_m_S[ug], LOD_m_F[ug]
% S_cBar_S[Hz/(kg/m3)], S_cBar_F[Hz/(kg/m3)], LODc_S[kg/m3],
LODc_F[kg/m3]
mfr_Re_S_Q_LOD = [v_h*1E6 v_b*1E6 v_L*1E6 vAspectRatio v_h./v_b./v_L ...
    vfVac1 vfVac1K vfInvF1 mfVisF1s(:,end) mfVisF1c(:,end) ...
    vRe_Sader/1E3 vRe_Best/1E3 vSm_Sader vSm_Best ...
    v_h./sqrt(v_L) vQ_Sader vQ_Best sqrt(v_L)./v_h vLODm_bar_Sader
vLODm_bar_Best ...
    vSc_bar_Sader vSc_bar_Best vLODc_bar_Sader vLODc_bar_Best];
mPercent_RhoL_Eta = [vPercent vRho_L vEta];
save(['postprocess22_Fr_Re_S_Q_LOD_' st_name, num2str(n_i) '.mat'],
'mfr_Re_S_Q_LOD', ...
      'vRho', 'mPercent_RhoL_Eta');
disp('      h/b    f_vac[MHz] f_F[MHz] Re_F[1E3]    Q_Best
S_cBar_F[kHz/(kg/m3)] LOD_F[1000kg/m3]');
disp([vAspectRatio vfVac1K mfVisF1c(:,end) vRe_Best/1E3 vQ_Best
vSc_bar_Best/1E3 vLODc_bar_Best/1E3]);

% Plots
scrsz = get(0,'ScreenSize'); figure('Position',scrsz);
set(gcf, 'PaperPosition', [0.25 2.5 13.33 10.0]);
switch st_name(1)
    case 'A' % Fixed Cross-Section Area in Water
        stTitle = [' (A=', num2str(v_h(1)*v_b(1)*1E12), '\mum^2)'];
    case 'L' % Fixed Length in Water
        stTitle = [' (L=', num2str(v_L(1)*1E6), '\mum)'];
    case 'h' % Fixed Thickness in Water
        stTitle = [' (h=', num2str(v_h(1)*1E6), '\mum)'];
    case {'G', 'E'} % Specific Geometry in Aqueous Glycerol/Ethanol
        stTitle = '';
    otherwise
        stTitle = [' !!! Wrong Parameter in
Characteristics_Torsional() !!!'];
```

```
end

%test vx = vEta./vRho_L;  strXLabel = '\eta/\rho_l [m^2/s]';
vx = vPercent;      strXLabel = ['Percent of Aqueous ' str_Fluid];

subplot(2,2,1);
switch st_name(1)
    case {'G', 'E'}
        plot(vx, 1E3*( vfInvF1 - vfInvF1(1) ), 'k', ...
             vx, 1E3*( mfVisF1s(:,end) - mfVisF1s(1,end) ), 'b', ...
             vx, 1E3*( mfVisF1c(:,end) - mfVisF1c(1,end) ), 'r-x');
        xlabel(strXLabel); ylabel('Shift in Resonance Frequency [kHz]');
    otherwise
        plot(vAspectRatio./v_L, vfInvF1, 'k', vAspectRatio./v_L,
mfVisF1s(:,end), 'b', ...
             vAspectRatio./v_L, mfVisF1c(:,end), 'r-x');
        xlabel('h/(bL) [m^{-1}]'); ylabel('Resonant Frequency [MHz]');
end
grid on; title(['Resonant Frequency' stTitle]);
legend('Inviscid Liquid, by Chu', 'Viscous Liquid, by Sader', ...
       'Viscous Liquid, by Fitting Expression', 'Location', 'Best');

subplot(2,2,2);
switch st_name(1)
    case {'G', 'E'}
        plot(vx, vQ_Sader, 'b', vx, vQ_Best, 'r-x');
        xlabel(strXLabel);
    otherwise
        plot(v_h./sqrt(v_L), vQ_Sader, 'b', v_h./sqrt(v_L), vQ_Best,
'r-x');
        xlabel('h/L^{0.5} [m^{0.5}]');
end
grid on; title(['Quality Factor' stTitle]);
ylabel('Quality Factor');
legend('Viscous Liquid, by Sader', 'Viscous Liquid, by Fitting
Expression', 'Location', 'Best');

subplot(2,2,3);
switch st_name(1)
    case {'G', 'E'}
        plot(vx, vSm_Sader, 'b', vx, vSm_Best, 'r-x');
        xlabel(strXLabel);
    otherwise
        plot(sqrt(v_h)./v_b./v_b./v_L./sqrt(v_L), vSm_Sader, 'b', ...
             sqrt(v_h)./v_b./v_b./v_L./sqrt(v_L), vSm_Best, 'r-x');
        xlabel('h^{0.5}/(b^2L^{1.5}) [m^{-3}]');
end
grid on; title(['Mass Sensitivity' stTitle]);
ylabel('Mass Sensitivity [Hz/pg]');
legend('Viscous Liquid, by Sader', 'Viscous Liquid, by Fitting
Expression', 'Location', 'Best');

subplot(2,2,4);
switch st_name(1)
    case {'G', 'E'}
        plot(vx, vLODm_bar_Sader, 'b', vx, vLODm_bar_Best, 'r-x');
```

```
        xlabel(strXLabel);
    otherwise
        plot(v_b.*v_L./sqrt(v_h), vLODm_bar_Sader, 'b',
v_b.*v_L./sqrt(v_h), vLODm_bar_Best, 'r-x');
        xlabel('bL/h^{0.5} [m^{1.5}]');
end
grid on; title(['Normalized Limit of Detection' stTitle]);
ylabel('Normalized Limit of Detection [\mug]');
legend('Viscous Liquid, by Sader', 'Viscous Liquid, by Fitting
Expression', 'Location', 'Best');

print('-dtiff', ['PostProcessF22_Fr_Q_S_LOD_' st_name, num2str(n_i)
'.tif']);


function mGeo_fr_Re_S_Q_LOD = Dimension_Torsional(v_fr, v_Re, v_AR, n_i,
st_name)
%% v_fr     vector varialbe, Resonance Frequency
%% v_Re     vector variable, Reynolds Number
%% v_AR     vector variable, Aspect Ratio (h/b)
%% n_i      No. of different Resonance Frequencies, Reynolds numbers or
Aspect Ratios
%% st_name  Part of the file name of the saved figures
%% Called by: Characteristics()
%% Call: getHDF_Ribbon(), getHDF_Thick(), getHDF_tors_rect_Sader()
%% mGeometry matrix variable, [vh, vb, vL_Sader, vL_Best]
sG = 79.6E9;              % [Pa], Shear Modulus of Silicon
sEta = 1E-3;              % [Ns/m^2]=[kg/s/m], Viscosity of Water
sRho = 2330;              % [kg/m^3], Density of Silicon
sRho_L = 1E3;             % [kg/m^3], Density of Water
vb = sqrt(2*sEta/pi/sRho_L.*v_Re./v_fr); % [m], Width
vh = vb .* v_AR;          % [m], Thickness
vxn = [0 1/10  1/5  1/4 1/3  2/5  1/2  2/3    1]'; % h/b
vyn = [6 6.41 6.87 7.12 7.6 8.03 8.73 10.2 14.2]'; % k2
vk2 = interp1(vxn,vyn,v_AR,'linear'); % Get the parameter by linear
interpolation
vK0 = vb.*vh.^3/3;        % [m^4], Geometric Function of the cross-
section, h/b=0
vK  = 2*vb.*vh.^3./vk2;   % [m^4], Geometric Function of the cross-
section, real h/b
vJ0 = vb.^3.*vh/12;                 % [m^4], Polar moment of the area,
h/b=0
vJ  = vb.*vh.*(vb.*vb + vh.*vh)/12; % [m^4], Polar moment of the area,
real h/b
vT  = pi*sRho_L.*vb.^4/8; % [.], Intermediate term

% Torsional: Our Numerical Results of Hydrodynamic Function
mHDF_Num = getHDF_Thick('Torsional Rectangular Thickness Interpolation',
v_Re, v_AR); % mmag, mphase, mreal, mimg
vg1_tors = 2*pi*v_fr .* vT .* diag(mHDF_Num(:,:,4));  % [kg.m/s],
g1_tors
vg2_tors = vT .* diag(mHDF_Num(:,:,3));               % [kg.m], g2_tors
vXi = vg1_tors/4/pi ./ v_fr ./ (sRho.*vJ + vg2_tors);  % [.], Damping
Ratio
vL_Num = sqrt(sG*vK.*(1-2*vXi.*vXi)./(sRho.*vJ + vg2_tors))/4 ./ v_fr; %
[m], Length
```

```
vQ_Num = 0.5 ./ vXi;                                % [.], Quality
Factor
vS_cbar_Num = v_fr/2 .* vJ ./ (sRho.*vJ + vg2_tors);   % [Hz/(kg/m^3)],
Normalized Sensitivity
vLODc_bar_Num = 1.5*v_fr ./ vQ_Num ./ vS_cbar_Num;     % [kg/m^3],
Normalized Limit of Detection

% Torsional: Our Analytical Expression of Hydrodynamic Function [Cai
2013 Dissertation]
mHDF_Best = getHDF_Thick('Torsional Rectangular Thickness Tao2', v_Re,
v_AR); % mmag, mphase, mreal, mimg
vg1_tors = 2*pi*v_fr .* vT .* diag(mHDF_Best(:,:,4)); % [kg.m/s],
g1_tors
vg2_tors = vT .* diag(mHDF_Best(:,:,3));            % [kg.m], g2_tors
vXi = vg1_tors/4/pi ./ v_fr ./ (sRho.*vJ + vg2_tors);  % [.], Damping
Ratio
vL_Best = sqrt(sG*vK.*(1-2*vXi.*vXi)./(sRho.*vJ + vg2_tors))/4 ./
v_fr; % [m], Length
vQ_Best = 0.5 ./ vXi;                               % [.], Quality
Factor
vS_cbar_Best = v_fr/2 .* vJ ./ (sRho.*vJ + vg2_tors);  % [Hz/(kg/m^3)],
Normalized Sensitivity
vLODc_bar_Best = 1.5*v_fr ./ vQ_Best ./ vS_cbar_Best;  % [kg/m^3],
Normalized Limit of Detection

% Torsional: Sader's Hydrodynamic Function
mHDF_Sader = getHDF_Ribbon('Torsional Rectangular', v_Re); % [vmag
vphase vreal vimg]
vg1_tors = 2*pi*v_fr .* vT .* mHDF_Sader(:,4);         % [kg.m/s],
g1_tors
vg2_tors = vT .* mHDF_Sader(:,3);                      % [kg.m],
g2_tors
vXi = vg1_tors/4/pi ./ v_fr ./ (sRho.*vJ0 + vg2_tors);   % [.], Damping
Ratio
vL_Sader = sqrt(sG*vK0.*(1-2*vXi.*vXi)./(sRho.*vJ0 + vg2_tors))/4 ./
v_fr; % [m], Length
vQ_Sader = 0.5 ./ vXi;                                 % [.], Quality
Factor
vS_cbar_Sader = v_fr/2 .* vJ0 ./ (sRho.*vJ0 + vg2_tors); %
[Hz/(kg/m^3)], Normalized Sensitivity
vLODc_bar_Sader = 1.5*v_fr ./ vQ_Sader ./ vS_cbar_Sader; % [kg/m^3],
Normalized Limit of Detection

% h: Thickness, b: Width, L: Length, h/b: Aspect Ratio, Re: Reynolds
Number,
% fr: Resonance Frequency, Q: Quality Factor, S: Normalized Sensitivity,
LOD: Limit of Detection
% _c: Chemical,  _N: Numerical Data,  _B: Our approach,  _S: Sader
%  %: Relative Error to the relevant results based on numerical data
% fr[MHz], Re, h/b, h[um], b[um],
% L_N[um], L_B[um], L_S[um], %L_B, %L_S,
% Q_N, Q_B, Q_S, %Q_B, %Q_S,
% S_cBar_N[Hz/(kg/m3)], S_cBar_B[Hz/(kg/m3)],
S_cBar_S[Hz/(kg/m3)], %S_B, %S_S
% LOD_N[1000kg/m3], LOD_B[1000kg/m3], LOD_S[1000kg/m3], %LOD_B, %LOD_S
mGeo_fr_Re_S_Q_LOD = [v_fr/1E6 v_Re v_AR vh*1E6 vb*1E6 ...
```

```
    vL_Num*1E6 vL_Best*1E6 vL_Sader*1E6 (vL_Best-vL_Num)./vL_Num*100
(vL_Sader-vL_Num)./vL_Num*100 ...
    vQ_Num vQ_Best vQ_Sader (vQ_Best-vQ_Num)./vQ_Num*100 (vQ_Sader-
vQ_Num)./vQ_Num*100 ...
    vS_cbar_Num vS_cbar_Best vS_cbar_Sader ...
    (vS_cbar_Best-vS_cbar_Num)./vS_cbar_Num*100 (vS_cbar_Sader-
vS_cbar_Num)./vS_cbar_Num*100 ...
    vLODc_bar_Num/1E3 vLODc_bar_Best/1E3 vLODc_bar_Sader/1E3 ...
    (vLODc_bar_Best-vLODc_bar_Num)./vLODc_bar_Num*100 (vLODc_bar_Sader-
vLODc_bar_Num)./vLODc_bar_Num*100];
save(['postprocess23_Geo_Re_S_Q_LOD_' st_name, num2str(n_i) '.mat'],
'mGeo_fr_Re_S_Q_LOD');
disp('    Re[1E3]    h[um]     b[um]    L_B[um]    Q_B
S_cBar_B[kHz/(kg/m3)]  LOD_B[1000kg/m3]');
disp([v_Re/1E3 vh*1E6 vb*1E6 vL_Best*1E6 vQ_Best vS_cbar_Best/1E3
vLODc_bar_Best/1E3]);


function m3_HDF = getHDF_Thick(str_Method, v_Reynolds, v_AspectRatio)
%% Calculate Hydrodynamic Function for Vibrating Microcantilevers in
Fluids
%% str_Method    string variable, Name or Type of Expressions or
Methods
%% v_Reynolds    vector variable, Reynolds Number
%% v_AspectRatio vector variable, Aspect Ratio (h/b)
%% Called by: Freq_Spectrum()
%% Call:      getHDF_Ribbon()
%% m3_HDF        3d matrix variable, Hydrodynamic Function (Magnitude,
Phase, Real part and Imaginary Part)
%%               at differnt Reynolds numbers and different Aspect
Ratios
m3_HDF = zeros(length(v_Reynolds), length(v_AspectRatio), 4); % [mMag,
mPhase, mReal, mImag]
switch str_Method
    case 'Transverse Rectangular Ribbon Sader' % [Sader 1998 JAP]
        mHDF_Ribbon = getHDF_Ribbon('Transverse Rectangular',
v_Reynolds);
        m3_HDF(:,:,3) = kron(mHDF_Ribbon(:,3), ones(1,
length(v_AspectRatio))); % Real Part
        m3_HDF(:,:,4) = kron(mHDF_Ribbon(:,4), ones(1,
length(v_AspectRatio))); % Imaginary Part

    case 'Lateral Rectangular Ribbon Stokes' % [Stokes 1851]
        mt = kron(2*sqrt(2)/pi ./ sqrt(v_Reynolds), ones(1,
length(v_AspectRatio)));
        m3_HDF(:,:,3) = mt;    % Real Part
        m3_HDF(:,:,4) = mt;    % Imaginary Part

    case 'Lateral Rectangular Thickness Russell' % [Cox 2012 JAP]
        mt = kron(2*sqrt(2)/pi ./ sqrt(v_Reynolds), ones(1,
length(v_AspectRatio)));
        % Real Part
        mCR = 1.658 * kron(sqrt(v_Reynolds), v_AspectRatio'.^1.83) + ...
              3.08  * kron(ones(length(v_Reynolds),1),
v_AspectRatio'.^0.85) + 1;
        m3_HDF(:,:,3) = mt .* mCR;
```

```
        % Imaginary Part
        mCI = kron(1./sqrt(v_Reynolds), 2.56 - 1.321*v_AspectRatio')
+ ...
              3.108 * kron(ones(length(v_Reynolds),1),
v_AspectRatio'.^0.85) + 1;
        m3_HDF(:,:,4) = mt .* mCI;

    case 'Torsional Rectangular Ribbon Sader' % [Green+Sader 2002 JAP]
        mHDF_Ribbon = getHDF_Ribbon('Torsional Rectangular',
v_Reynolds);
        m3_HDF(:,:,3) = kron(mHDF_Ribbon(:,3), ones(1,
length(v_AspectRatio))); % Real Part
        m3_HDF(:,:,4) = kron(mHDF_Ribbon(:,4), ones(1,
length(v_AspectRatio))); % Imaginary Part

    case 'Torsional Rectangular Thickness Tao1' % [Cai 2012 IFCS]
        % (a + b*x^(-m)) * (c + y^n),   x=Re=1-31620, y=h/b=0.01-0.2
        % Real Part = (0.049369 + 0.23625 Re^(-0.42804)) * (1.2012 +
(h/b)^0.88591)
        % -6.19% ~ 3.85%
        vHDF_AR = 1.2 + v_AspectRatio' .^ 0.89;
        vHDF_Re = 0.05 + 0.24 .* v_Reynolds .^ (-0.43);
        m3_HDF(:,:,3) = kron(vHDF_AR, vHDF_Re);
        % (b*exp(-m*x*log(10)) + d*exp(-x*log(10)/2)) * (c + y^n),
x=Re=1-31620, y=h/b=0.01-0.2
        % Imag Part = (1.043 Re^(-1.0667) + 0.45389 Re^(-0.5)) *
(0.75346 + (h/b)^1.0374)
        % -22.1% ~ 6.12%
        vHDF_AR = 0.75 + v_AspectRatio';
        vHDF_Re = v_Reynolds .^ (-1) + 0.45 ./ sqrt(v_Reynolds);
        m3_HDF(:,:,4) = kron(vHDF_AR, vHDF_Re);

    case 'Torsional Rectangular Thickness Tao2' % [Cai 2013
Dissertation]
        % (a*x^(-0.5) + b*x^(-0.25) + c) * (1 + d * y + e*y*y),
x=Re=1-31620, y=h/b=0.01-0.2
        % Real Part = (0.2123 Re^(-0.5) + 0.07362 Re^(-0.25) + 0.05693)
* (1 + 1.138(h/b) - 0.8151(h/b)^2)
        % -5.89% ~ 5.79%
        vHDF_AR = 1 + 1.1*v_AspectRatio' -
0.82*v_AspectRatio'.*v_AspectRatio';
        vHDF_Re = 0.21 .* v_Reynolds .^ (-0.5) + 0.075 .* v_Reynolds .^
(-0.25) + 0.057;
        m3_HDF(:,:,3) = kron(vHDF_AR, vHDF_Re);
        % (a*exp(-x*log(10)) + b*exp(-0.75*x*log(10)) + c*exp(-
x*log(10)/2) + d) * (1 + e*y + f*y*y), x=Re=1-31620, y=h/b=0.01-0.2
        % Imag Part = (1.023 Re^(-1.5) - 0.2846 Re^(-1) + 0.3871 Re^(-
0.5) + 0.0001778) * (1 + 1.256(h/b))
        % -11.2% ~ 11.0%
        vHDF_AR = 1 + 1.24*v_AspectRatio';
        vHDF_Re = 1.1*v_Reynolds.^(-1) - 0.29*v_Reynolds.^(-0.75) +
0.39 ./ sqrt(v_Reynolds) + 0.00018;
        m3_HDF(:,:,4) = kron(vHDF_AR, vHDF_Re);

    case 'Torsional Rectangular Thickness Interpolation' % [Cai 2013
Dissertation]
```

```
        % load saved variables
        % vAspectRatio  Vector, Aspect Ratios
        % vReynolds     Vector, Reynolds Numbers
        % mHDF_Sader    Matrix, Hydrodynamic Function by Sader
        %                       (Magnitude, Phase, Real part, Imaginary
Part)
        % mHDF1Mag      Matrix, Magnitude of Hydrodynamic Function
        % mHDF2Phase    Matrix, Phase of Hydrodynamic Function
        % mHDF3Real     Matrix, Real Part of Hydrodynamic Function
        % mHDF4Imag     Matrix, Imaginary Part of Hydrodynamic Function
        % mHDF5Err      Matrix, Error of Hydrodynamic Function
        load postprocess11_mHDF.mat;
        m3_HDF(:,:,3) = interp2(vReynolds, vAspectRatio, mHDF3Real,
v_Reynolds, v_AspectRatio'); % Real Part
        m3_HDF(:,:,4) = interp2(vReynolds, vAspectRatio, mHDF4Imag,
v_Reynolds, v_AspectRatio'); % Imaginary Part

    otherwise
        disp(['!!!???!!! getHDF_Thick: Can Not find Method of '
str_Method]);
end
if abs(v_Reynolds(1)) < 1E-20 % here Re=0 means f=0, that is, static
response (No fluid effect)
    m3_HDF(1,:,3) = zeros(1,length(v_AspectRatio));
    m3_HDF(1,:,4) = zeros(1,length(v_AspectRatio));
end
m3_HDF(:,:,1) = sqrt( m3_HDF(:,:,3).*m3_HDF(:,:,3) +
m3_HDF(:,:,4).*m3_HDF(:,:,4) ); % Magnitude
m3_HDF(:,:,2) = atan( m3_HDF(:,:,4)./m3_HDF(:,:,3) ); % Phase


function [sE sG vRho vRho_L vEta vPercent] =
getMatProp_Value(str_Structure, str_Fluid)
%% Set Properties for the Cantilever and the Fluid
%%   str_Structure  string variable, Material Name of the Structure
%%   str_Fluid      string variable, Material Name of the Fluid
%% Called by: Freq_Spectrum(), Characteristics_Torsional()
%%   [sE, sG, vRho, vRho_L, vEta, vPercent]   vector/matrix variable
%%                  Young's Mudulus, Shear Mudulus, Density of the
Structure
%%                  and Density, Dynamic Viscosity, percent (w/w) of
the Fluid
vPercent = 0;
switch str_Structure
    case 'SiliconE' % Experiments data from Dr. Brand
        sE = 110E9;      % [Pa], Young's Modulus of Silicon
        sG = 45.4E9;     % [Pa], Shear Modulus of Silicon
        vRho = 2330;     % [kg/m^3], Density of Silicon
    case 'SiliconB'
        sE = 169E9;      % [Pa], Young's Modulus of Silicon
        sG = 79.6E9;     % [Pa], Shear Modulus of Silicon
        vRho = 2320;     % [kg/m^3], Density of Silicon
    otherwise % Default Material of Structure: Silicon Standard
        sE = 169E9;      % [Pa], Young's Modulus of Silicon
        sG = 79.6E9;     % [Pa], Shear Modulus of Silicon
        vRho = 2330;     % [kg/m^3], Density of Silicon
```

```
end

% Water Properties for Aqueous Glycerol and Aqueous Ethanol
sEta_Water = 1E-3;   % [Pa.s], Viscosity of water @ 20C (@ T=25C Eta =
0.89E-3)
sRho_Water = 997;    % [kg/m^3], Density of water

switch str_Fluid
    case 'Glycerol' % 37 points
        % Percent (w/w) Aqueous Glycerol
        vPercent = [0 0.5  1  2  3  4  5  6  7  8   9 10 12 14 16 18 20
24 28 32 ...
                    36 40 44 48 52 56 60 64 68 72  76 80 84 88 92 96
100]';
        % Viscosity Ratio to Water
        vrEta = [1     1.009 1.020 1.046 1.072 1.098 1.125 1.155 1.186
1.218 ...
                 1.253 1.288 1.362 1.442 1.530 1.627 1.734 1.984 2.274
2.632 ...
                 3.082 3.646 4.434 5.402 6.653 8.332 10.66 13.63 18.42
27.57 ...
                 40.49 59.78 84.17 147.2 383.7 778.9 1759.6]';
        % Density Ratio to Water
        vrRho_L = [1      0.9994 1.0005 1.0028 1.0051 1.0074 1.0097
1.0120 1.0144 1.0167 ...
                   1.0191 1.0215 1.0262 1.0311 1.0360 1.0409 1.0459
1.0561 1.0664 1.0770 ...
                   1.0876 1.0984 1.1092 1.1200 1.1308 1.1419 1.1530
1.1643 1.1755 1.1866 ...
                   1.1976 1.2085 1.2192 1.2299 1.2404 1.2508 1.2611]';
        vRho = vRho * ones(length(vPercent), 1); % [kg/m^3], Density of
Microcantilever
        vEta   = sEta_Water * vrEta;             % [Pa.s], Viscosity of
Fluid
        vRho_L = sRho_Water * vrRho_L;           % [kg/m^3], Density of
Fluid
    case 'Water'
        vRho_L = 1E3;    % [kg/m^3], Density of Water
        vEta = 1E-3;     % [Pa.s]=[kg/s/m], Viscosity of Water
    case 'AirB' % [Basak+Raman 2006 JAP]
        vRho_L = 1.18;   % [kg/m^3], Density of Air
        vEta = 1.86E-5;  % [Pa.s]=[kg/s/m], Viscosity of Air
    otherwise % Default Material of Fluid: Air
        vRho_L = 1.205;  % [kg/m^3], Density of Air
        vEta = 1.827E-5; % [Pa.s]=[kg/s/m], Viscosity of Air
end
```